Cross section measurements of D^* production in the decay channel $D^{*\pm} \to K^{\mp}\pi^{\pm}\pi^{\pm}\pi^{\mp}\pi^{\pm}$ and search for a charmed pentaquark with the H1 detector at HERA

Diplomarbeit

Humboldt-Universität zu Berlin
Mathematisch-Naturwissenschaftliche Fakultät I
Institut für Physik

eingereicht von

Florian Bechtel
geboren am 16.05.1979 in Speyer

1. Gutachter: Prof. Dr. Hermann Kolanoski
2. Gutachter: Prof. Dr. Nikolaj Pavel
Berlin, August 2005

Abstract

In this work, the production and decay of D^* mesons is investigated, measured in deep-inelastic electron-proton collisions with the H1 detector at the HERA accelerator (DESY, Hamburg). D^* mesons are produced mostly in the fragmentation of charm quarks originating from boson-gluon fusion. Measurements of the D^* production cross section offer an excellent tool to probe the gluon content of the proton and to test perturbative quantum chromodynamics. In previous analyses, only the decay channel $D^{*+} \to D^0\pi_s^+$, $D^0 \to K^-\pi^+$ (and charge conjugates) has been exploited with the H1 experiment. In this work, a reconstruction of D^* mesons in the decay channel $D^{*+} \to D^0\pi_s^+$, $D^0 \to K^-\pi^+\rho^0$, $\rho^0 \to \pi^+\pi^-$ is presented, leading to cross section measurements.

A search for exotic baryons containing charm has been performed with the H1 detector and a resonance has been found in the invariant mass spectrum of oppositely charged D^*p combinations. D^* mesons have been reconstructed in the decay channel $D^{*\pm} \to K^\mp\pi^\pm\pi_s^\pm$. To improve the statistics for this particular search, D^*p combinations are investigated where the D^* decays via $D^{*\pm} \to K^\mp\pi^\pm\pi^\pm\pi^\mp\pi_s^\pm$.

Zusammenfassung

In dieser Arbeit wird die Produktion und der Zerfall von D^*-Mesonen untersucht, gemessen in tief-inelastischen Elektron-Proton-Stößen mit dem H1-Detektor am HERA-Beschleuniger (DESY, Hamburg). D^*-Mesonen werden überwiegend bei der Fragmentation von Charm-Quarks aus Boson-Gluon-Fusion erzeugt. Die Messung des Wirkungsquerschnitts der D^*-Produktion bietet ein hervorragendes Werkzeug zur Bestimmung der Gluondichte des Protons und zum Test der perturbativen Quantenchromodynamik. Bisher wurde beim H1-Experiment ausschließlich der Zerfallskanal $D^{*+} \to D^0\pi_s^+$, $D^0 \to K^-\pi^+$ (und Ladungskonjugierte) genutzt. Diese Arbeit beinhaltet eine Rekonstruktion von D^*-Mesonen im Zerfallskanal $D^{*+} \to D^0\pi_s^+$, $D^0 \to K^-\pi^+\rho^0$, $\rho^0 \to \pi^+\pi^-$ sowie Messungen von Wirkungsquerschnitten.

Beim H1-Experiment wurde eine Suche nach exotischen Baryonen mit Charm durchgeführt. Im invarianten Massenspektrum von entgegengesetzt geladenen D^*p-Kombinationen wurde eine Resonanz gefunden. Dazu wurde der Zerfallskanal $D^{*\pm} \to K^\mp\pi^\pm\pi_s^\pm$ analysiert. Um die Statistik für diese spezielle Suche zu erhöhen, werden D^*p-Kombinationen untersucht, bei denen das D^* im Zerfallskanal $D^{*\pm} \to K^\mp\pi^\pm\pi^\pm\pi^\mp\pi_s^\pm$ rekonstruiert wird.

Contents

Introduction 1

1 Charm production in electron-proton scattering 3
- 1.1 DIS kinematics . . . 3
- 1.2 Proton Structure . . . 5
- 1.3 Charm Production: Boson-Gluon Fusion . . . 6
- 1.4 Hadronization . . . 8
- 1.5 Spectroscopy of exotic baryons containing charm . . . 9
- 1.6 Event generators . . . 11
  - 1.6.1 RAPGAP Monte Carlo . . . 12
  - 1.6.2 DJANGO Monte Carlo . . . 12

2 HERA and H1 13
- 2.1 HERA: Hadron Electron Ring Accelerator in Hamburg . . . 13
- 2.2 H1 detector . . . 14
  - 2.2.1 Tracking . . . 16
  - 2.2.2 Electron identification . . . 22
  - 2.2.3 Trigger . . . 24
  - 2.2.4 Luminosity measurement . . . 27

3 Reconstruction of D^* mesons in the decay $D^* \to K\pi\pi\pi_s$ 29
- 3.1 Reconstruction method . . . 30
- 3.2 Selection cuts . . . 32
  - 3.2.1 Online D^* selection . . . 32
  - 3.2.2 Track quality and particle identification . . . 33
  - 3.2.3 Reconstruction of D^* mesons . . . 34
  - 3.2.4 Signal extraction . . . 50
- 3.3 Analysis of D^* production . . . 52
  - 3.3.1 Determination of D^* meson yields . . . 52
  - 3.3.2 Detector acceptance . . . 55
  - 3.3.3 Differential cross sections . . . 59

3.3.4 Discussion 67

4 Search for exotic baryons containing charm **69**
4.1 Selection criteria 70
4.2 Reconstruction efficiency 76
4.3 Investigation of the D^*p invariant mass spectrum 78
4.4 Limits on θ_c production 90
4.5 Discussion 94

5 Summary **95**

Acknowledgments **101**

Introduction

The subject of Elementary Particle Physics is the understanding of the basic constituents of matter and their interactions. A gauge theory description with a $SU(3)_c$ symmetry for the strong interaction and a spontaneously broken $SU(2)_L \bigotimes U(1)_Y$ symmetry for the electroweak interaction has been successfully formulated and tested. It is known today as *the* Standard Model. Six quarks and six leptons are the fundamental fermions, interacting via the exchange of gauge bosons: The photon and the $W^{\pm}$ and Z^0 bosons are the gauge bosons of the electroweak interaction, gluons are the gauge bosons of the strong interaction. The Higgs boson has been postulated to explain the spontaneous symmetry breaking in the electroweak sector; it has however not been found up to the present. The quantum field theory describing the strong interaction of quarks is called quantum chromodynamics (QCD): Quarks interact strongly via the exchange of gluons.

The **H**adron **E**lectron **R**ing **A**ccelerator at DESY Hamburg was designed to investigate the structure of the proton, in all its facets. In this work, the production of charm quarks in deep-inelastic electron-proton collisions at HERA is investigated. Here, charm quarks are mainly produced in boson-gluon fusion, where a photon emitted by the incoming electron interacts with a gluon from the proton to produce a $c\bar{c}$-pair. The measurement of the hadronic final state in gluon-induced processes, such as open charm production in boson-gluon fusion, allows a determination of the gluon density in the proton.

QCD cross section calculations are performed with the help of perturbation theory with the expansion parameter α_s, the strong coupling constant. The perturbation series will only converge if the expansion parameter is sufficiently small. The QCD coupling α_s decreases with harder scales such that the convergence of the perturbation series improves with harder scales, for example with a large photon virtuality Q^2 or with the mass of a heavy quark. Hence, the hard scale introduced by the heavy charm quark mass provides an excellent testing ground of perturbative QCD.

The identification of the charm quark can be performed via e.g. measure-

ment of $D^{*\pm}$ mesons ($c\bar{d}$ or $\bar{c}d$ quark combinations), due to a clean signature. In standard D^* analyses with data from the H1 detector at HERA, D^* mesons are reconstructed in the decay channel $D^{*+} \to D^0\pi^+$, $D^0 \to K^-\pi^+$. The decay channel $D^{*+} \to D^0\pi^+$, $D^0 \to K^-\pi^+\rho^0$, $\rho^0 \to \pi^+\pi^-$ was previously not exploited. The aim of this work is to implement this decay channel into the H1 analysis framework and to measure differential production cross sections from a data sample taken in the years 1996-2000. The inclusion of this decay channel into the H1 analysis framework corresponds to a significant increase in D^* statistics.

Another interesting aspect of charm physics is charm spectroscopy. In general, hadron spectroscopy investigates the masses, widths, decay channels and quark contents of hadrons. QCD allows various colorless combinations of quarks. However, up to now, only the states with the minimum number of quarks have been observed: Mesons, composed of a quark and an anti-quark, and baryons, composed of three quarks. In the last three years, the search for states with more than three quarks has become a very active research field. Recent observations of a narrow resonance decaying to K^+n or K^0p and being interpreted as a strange pentaquark triggered a search for narrow resonances with the H1 experiment. H1 is the first and, up to now, the only experiment to have observed a narrow anti-charmed baryon state, decaying to $D^{*-}p$ or $D^{*+}\bar{p}$ and being interpreted as a charmed pentaquark (with quark content $uudd\bar{c}/\bar{u}\bar{u}\bar{d}\bar{d}c$). This resonance was observed for D^* mesons decaying into a $K^\mp\pi^\pm\pi^\pm$ final state. To increase the statistics for this particular search, a search for exotic baryons containing charm is performed with D^* candidates reconstructed in the decay channel $D^{*\pm} \to K^\mp\pi^\pm\pi^\pm\pi^\mp\pi^\pm$.

This thesis is organized as follows: Chapter 1 describes the theoretical framework for heavy flavor production in deep-inelastic electron proton scattering at HERA. The HERA accelerator and the H1 detector are described in chapter 2. The reconstruction of D^* mesons in the decay channel $D^{*+} \to D^0\pi_s^+$, $D^0 \to K^-\pi^+\rho^0$, $\rho^0 \to \pi^+\pi^-$ is presented in chapter 3 together with cross section measurements. The reconstructed D^* candidates are combined with proton candidates and a search for exotic baryons containing charm is presented in chapter 4. Chapter 5 summarizes this work and discusses the results.

Chapter 1

Charm production in electron-proton scattering

In this chapter, the physics involved in the production of charm quarks in deep-inelastic electron-proton (ep) scattering is described. Section 1.1 introduces the variables used to characterize deep-inelastic-scattering (DIS) events. Section 1.2 reviews the proton structure function formalism. The main production mechanism for charm quarks is outlined in section 1.3. Section 1.4 describes phenomenological models for the transition of quarks to observable hadrons. Recent observations of exotic baryon states with strangeness triggered a search for exotic baryons in the charm sector. Section 1.5 describes this search using data from the H1 experiment. Section 1.6 presents the implementation of quantum chromodynamics (QCD) in event generators to determine the detector acceptance and the production cross section.

1.1 DIS kinematics

Leading order deep-inelastic ep scattering is described by the exchange of a gauge boson between the electron and a quark from the proton. Processes can be classified by the charge of the exchanged gauge boson:

- A $W^{\pm}$ boson is exchanged in *charged current (CC)* reactions. These reactions are of the kind $ep \to \nu X$, the outgoing lepton is a neutrino.
- If the exchanged boson is neutral, the reaction is of the *neutral current (NC)* type; the exchanged gauge boson is a virtual photon γ or Z^0 boson. The reaction is of the kind $ep \to e'X$.

The hadronic final state X includes the fragments of the struck quark and the *proton remnant*, defined as the part of the proton which does not take part in the hard[1] interaction.

The leading order Feynman diagram of ep scattering is shown in figure 1.1, where $\mathbf{q}$, $\mathbf{k}$, $\mathbf{k}'$ and $\mathbf{P}$ are the four-momenta of the exchanged boson, incoming and outgoing lepton and incoming proton, respectively. The entire scattering process can be formulated with the electromagnetic ($L_{\mu\nu}$) and hadronic ($W^{\mu\nu}$) tensor.

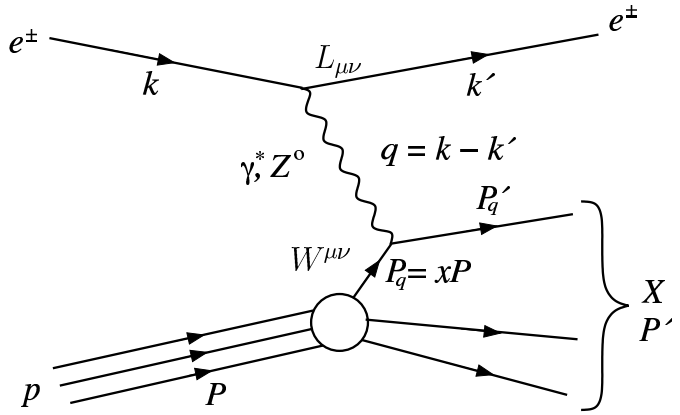

Figure 1.1: Leading order Feynman diagram for neutral current deep-inelastic scattering. The description of the kinematic variables is given in the text.

The kinematics of the process is described by three variables, Q^2, x and y, which are Lorentz-invariant. The negative four-momentum of the photon squared Q^2 (also called photon virtuality) is defined by

$$Q^2 = -\mathbf{q}^2 = (\mathbf{k} - \mathbf{k}')^2 \quad , \tag{1.1}$$

while x is the *Bjorken scaling variable* defined as:

$$x = \frac{Q^2}{2\mathbf{P} \cdot \mathbf{q}} \quad . \tag{1.2}$$

In the *infinite momentum frame* (i.e. in an inertial frame where $m_{\text{proton}} \ll E_{\text{proton}}$), the Bjorken scaling variable x equals the fraction of the proton momentum carried by the struck parton. The normalized energy loss of the

[1]The scattering process is characterized by the mass scales or momentum transfers involved. *Hard* scales correspond to large masses or momentum transfers, *soft* scales correspond to small masses or momentum transfers.

scattered lepton in the proton rest frame is the *inelasticity* y, which is defined as

$$y = \frac{\mathbf{P}\cdot\mathbf{q}}{\mathbf{P}\cdot\mathbf{k}} \quad . \tag{1.3}$$

The connection between center-of-mass energy $\sqrt{s}$, the photon virtuality Q^2, the inelasticity y and the Bjorken scaling variable x follows from

$$\begin{aligned} s &= (\mathbf{k}+\mathbf{P})^2 \\ &= \underbrace{k^2}_{=m_e^2} + \underbrace{P^2}_{=m_p^2} + 2\mathbf{k}\cdot\mathbf{P} \\ &= m_e^2 + m_p^2 + Q^2 \underbrace{\frac{2\mathbf{P}\cdot\mathbf{q}}{Q^2}}_{=1/x} \underbrace{\frac{\mathbf{P}\cdot\mathbf{k}}{\mathbf{P}\cdot\mathbf{q}}}_{=1/y} \quad . \end{aligned}$$

For constant beam energies, only two of the three kinematic variables Q^2, y and x are independent. The above relation reads for negligible electron and proton masses:

$$Q^2 = xys \quad . \tag{1.4}$$

Two kinematic regimes are distinguished by the photon virtuality Q^2: The *photoproduction* regime is defined by a small Q^2 ($Q^2 \to 0$), the exchanged photon is almost real. The *deep-inelastic scattering* regime is characterized by a non-vanishing Q^2 ($Q^2 > 1$ GeV^2), the exchanged photon is space-like.

The invariant mass of the hadronic final state W is defined by

$$W^2 = (\mathbf{q}+\mathbf{P})^2 = -Q^2 + m_p^2 + \frac{Q^2}{x} \quad . \tag{1.5}$$

1.2 Proton Structure

The neutral current differential cross section for unpolarized deep-inelastic ep scattering can be written in terms of *structure functions*, namely as a combination of $F_1(x,Q^2)$ and $F_2(x,Q^2)$ or $F_2(x,Q^2)$ and $F_L(x,Q^2)$:

$$\frac{d^2\sigma_{NC}}{dx\,dQ^2} = \frac{4\pi\alpha^2}{xQ^4}\left(xy^2F_1(x,Q^2) + (1-y)\,F_2(x,Q^2)\right) \tag{1.6}$$

$$= \frac{4\pi\alpha}{xQ^4}\left(\left(1-y+\frac{y^2}{2}\right)F_2(x,Q^2) - \frac{y^2}{2}F_L(x,Q^2)\right) \quad , \tag{1.7}$$

where α is the QED coupling constant. Equations 1.6 and 1.7 neglect contributions from Z^0 exchange which are small for $Q^2 < 1000$ GeV^2. The longitudinal structure function $F_L(x,Q^2)$ is defined by

$$F_L(x,Q^2) = F_2(x,Q^2) - 2xF_1(x,Q^2) \quad . \tag{1.8}$$

The non-Abelian structure of QCD leads to a running QCD coupling constant $\alpha_s = \alpha_s(Q^2)$ which is large at soft scales and small at hard scales (*confinement* for small Q^2 and *asymptotic freedom* at high Q^2). Perturbative calculations are only valid for hard processes, and cross sections are calculated with the help of the QCD factorization theorem (see e.g. [1]): The cross section is a convolution of the matrix element of the hard subprocess with universal parton density functions (PDF). The parton density functions include all soft processes inside the proton and have to be measured.

The simplest model to describe the substructure of the interacting proton is the *quark-parton model*. The quark-parton model is the zeroth-order QCD description of the proton structure. In this model, the proton is assumed to consist of point-like and quasi-free fermions, called *partons*, described by probability distribution functions $q_i(x)$ for the probability to find the parton of flavor i at a proton momentum fraction within $[x, x + dx]$. The partons are identical to the valence quarks. Deep-inelastic electron-proton scattering is assumed to be elastic scattering of electrons off the point-like partons. Within the quark-parton-model and assuming photon exchange, the structure functions are independent of Q^2 (*scaling behavior*):

$$F_2(x, Q^2) = F_2(x) = \sum_{i=1}^{n_f} e_1^2 x q_i(x) \quad , \tag{1.9}$$

$$F_L(x, Q^2) = F_L(x) = 0 \quad , \tag{1.10}$$

where e_i is the quark's charge. In higher-order QCD, the proton consists of valence quarks, gluons, sea quarks and sea anti-quarks: *Scaling violations* occur, i.e. F_2 is a function of Q^2.

1.3 Charm Production: Boson-Gluon Fusion

Perturbative QCD breaks down at soft scales, where the QCD coupling constant α_s is large. The large charm quark mass of 1.15 to 1.35 GeV [2] introduces a hard scale which allows the application of perturbative QCD. The dominant production mechanism for charm in deep-inelastic electron-proton scattering at $Q^2 \approx 4m_c^2$ is *direct boson-gluon fusion*, where a $c\bar{c}$ pair is created by the interaction of the exchanged photon with a gluon in the proton. The leading order Feynman graph is shown in figure 1.2. For $Q^2 \gg m_c^2$, charm quarks can be treated as massless particles.

Another mechanism for charm production is *resolved* boson-gluon fusion, shown in figure 1.3, where a gluon from the proton interacts with a charm

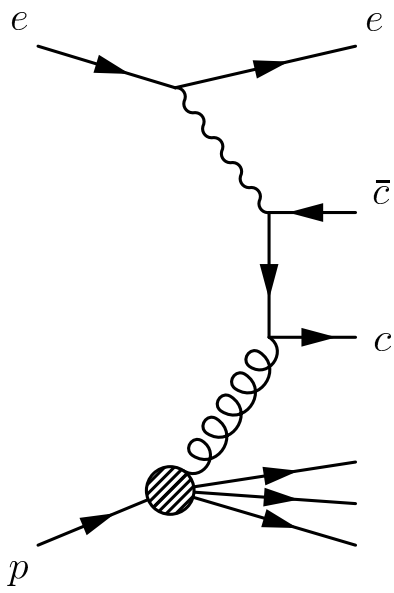

Figure 1.2: Leading order direct boson-gluon fusion

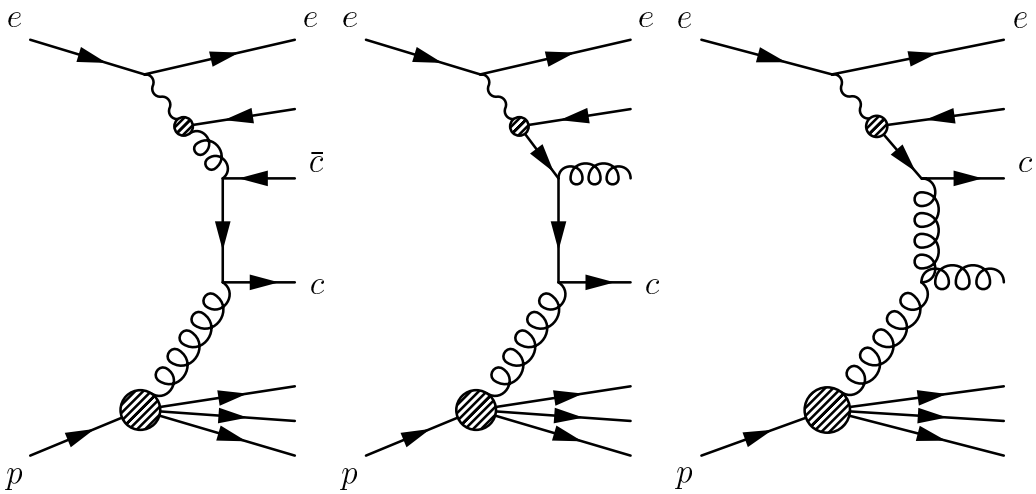

Figure 1.3: Charm production in resolved photon processes: gluon-gluon fusion (left) and charm excitation (middle and right) [3].

quark or a gluon from the photon. Its contribution to charm production is of the order of 5% [4].

Charm production in *ep* scattering is described by the charm contribution F_2^c to the proton structure function F_2:

$$F_2(x,Q^2) = \sum_{i=u,d,s} e_i^2 x \left(q_i(x,Q^2) + \bar{q}_i(x,Q^2)\right) + F_2^c(x,Q^2) \quad , \tag{1.11}$$

where i denotes the flavor of the involved quark.

The ratio F_2^c/F_2 increases from 10% at $Q^2 = 1.5$ GeV^2 and $x \approx 10^{-4}$ to 25% at $Q^2 \approx 25$ GeV^2 and $x \leq 5 \cdot 10^{-4}$ [5]. (The beauty contribution to the proton structure, F_2^b, is of the order of $1-2\%$ [6,7].)

1.4 Hadronization

Quarks and gluons cannot be observed as free particles. They transform into colorless hadrons forming hadronic jets. This transition is called *fragmentation* or *hadronization* and cannot be described perturbatively but only with phenomenological models. Examples of theses models are the cluster model, the Lund string model or the Peterson model.

The *cluster model* [8,9] merges partons to color neutral clusters, which fragment either into two hadrons or into the lightest hadron with the corresponding flavor.

The *Lund string model* [10,11,12] implements the strong force among the partons by connecting the color charges through one-dimensional strings which mediate the color flow. Quark-antiquark pair production corresponds to the breaking of a string and can be described as a tunneling phenomenon. The strings are developed until the quarks are on mass-shell.

The *Peterson model* [13] describes the transition of a heavy quark Q to a bound hadron H. Within this model, the fragmentation process is completely determined by the momenta of heavy quark and hadron; the process is independent of the proton remnant. A light $q\bar{q}$ pair is produced in vacuum fluctuations and a bound meson state $Q\bar{q}$ is formed. The Peterson fragmentation function $dN(z)/dz$ (see also figure 1.4) approximates the $Q \to Q\bar{q}$ transition probability by the inverse of the squared energy difference between initial and final state:

$$\frac{dN}{dz} = \frac{1}{z\left(1 - \frac{1}{z} - \frac{\epsilon_Q}{1-z}\right)^2} \quad , \tag{1.12}$$

where z is the momentum fraction transferred from the heavy quark Q to the produced hadron H.

The Peterson fragmentation parameter ϵ_Q describes the hardness of the fragmentation process and is defined by

$$\epsilon_Q = \frac{m_q}{m_Q} \quad .$$

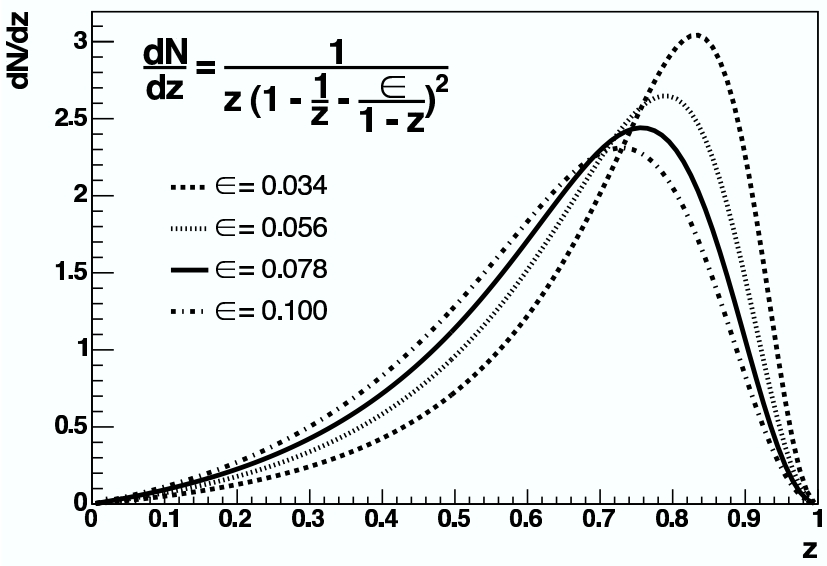

Figure 1.4: The Peterson fragmentation function dN/dz shown for different parameters ϵ between 0.034 and 0.1.

Due to uncertainties in quark mass assignment, the fragmentation parameter is determined experimentally. In the following, a value of $\epsilon_c(D^{*\pm}) = 0.078 \pm 0.008$ [14] is used.

1.5 Spectroscopy of exotic baryons containing charm

As mentioned before, quarks are confined into colorless hadrons. This demand allows, however, for an arbitrary number of $q\bar{q}$ pairs and gluons inside a hadron. In the last 50 years of hadron spectroscopy, however, only the minimum realizations of the quark model have been observed: All known hadrons are either quark-antiquark combinations (mesons) or three-quark combinations (baryons). In the last three years, the search for pentaquarks has become a very active branch of hadron spectroscopy. The minimum quark content of a pentaquark are four quarks and one anti-quark. If the

anti-quark flavor is different from that of the other four quarks, no three-quark combination can have the same quantum numbers. Such a state is called an *exotic pentaquark*.

Experimental observations of a narrow resonance with a mass in the region of 1540 MeV, decaying to K^+n or K^0p, have been reported by several experiments [15,16,17,18,19,20,21,22,23]. With a baryon number and strangeness of +1, the minimal composition of such a state in the constituent quark model is $uudd\bar{s}$. The resonance has been interpreted as a pentaquark, the θ^+. Its mass has been predicted in [24]. Two related states with strangeness −2 have also been observed [25]. The possibility of pentaquarks containing charm has been discussed and their expected properties have been predicted [26,27].

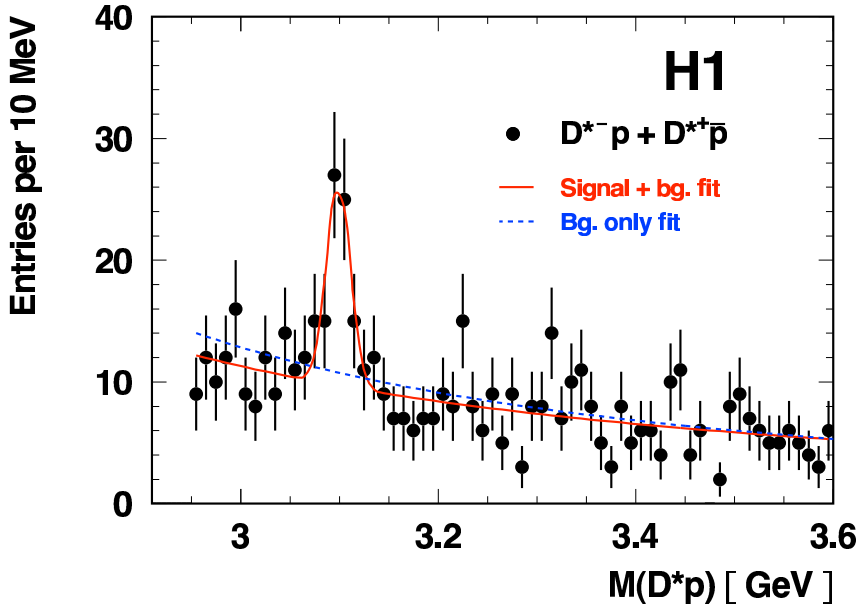

Figure 1.5: Invariant mass of the D^*p system; the D^* mesons have been reconstructed in the decay channel $D^* \to D^0\pi_s \to K\pi\pi_s$

A narrow state in $D^{*-}p$ and $D^{*+}\bar{p}$ invariant mass combinations has been observed with the H1 experiment [28]. In figure 1.5, the D^*p invariant mass spectrum from oppositely charged D^*p combinations in deep-inelastic scattering is shown, compared to two different fits. The resonance has a mass of 3099 ± 3 (stat.) ± 5 (syst.) MeV and a measured Gaussian width of 12 ± 3 (stat.) MeV which is compatible with the experimental resolution. A background fit yields 51.7 ± 2.7 (stat.) background events in the same interval, while 95 events are observed in a $\pm 2\sigma$ interval around the resonance. The

observed number of events corresponds to a 5.4σ statistical fluctuation.

If the state decays strongly to $D^{*-}p$ or $D^{*+}\bar{p}$, it must have baryon number ± 1 and charm ∓ 1. Its minimal constituent quark composition follows to be $uudd\bar{c}$ or $\bar{u}\bar{u}\bar{d}\bar{d}c$. Hence, the observed state is a candidate for a charmed pentaquark. One task of this work is to investigate the D^*p invariant mass spectrum by adding a D^* decay channel which is not yet exploited with the H1 experiment.

1.6 Event generators

Monte Carlo generators are necessary to simulate the cross sections of particular physical process in order to compare theory to experiment. In this work, they are used to investigate the kinematics of signal and background. An event generator produces a large number of events which are statistically distributed according to the cross section predictions of the implemented model. Events are generated in several steps:

- The incoming scatterers are characterized. In the HERA case, the proton is described by *parton distribution functions* which specify the parton energies.
- A parton shower from the proton is intiated (*initial state shower*).
- An incoming particle from the proton shower interacts with the photon in a hard scattering process according to the deep-inelastic scattering cross section.
- The outgoing particles generate parton showers (*final state showers*).
- The proton remnant can still carry color charge and interact with the final state.
- Phenomenological models describe the parton fragmentation to observable hadrons. These hadrons can be unstable and decay further.
- The incoming or scattered lepton can radiate a photon (*initial* or *final state radiation*).

The generated hadronic final state is fed into a detector simulation to determine the detector response, such as e.g. hits in the drift chambers, showers in the calorimeters or trigger signals. The data sets thus generated can be compared to the data sets produced by the detector. In the following, two event generators, RAPGAP and DJANGO, are described.

1.6.1 RAPGAP Monte Carlo

The *RAPGAP* [29] event generator was designed to generate deep-inelastic and diffractive events. This work uses version 3.1. For heavy quark simulation, RAPGAP includes the complete boson-gluon fusion matrix element to order $\alpha^2\alpha_s$, as well as the heavy quark masses and electroweak contributions. Initial and final state showers are ordered according to the radiated parton's virtuality. Light quark fragmentation is described by the Lund string model, heavy quark fragmentation is described by the Peterson model.

RAPGAP does initially not generate pentaquarks. To simulate a charmed pentaquark with RAPGAP, mass and decay modes of D_1^0, D_1^{*0} and D_2^{*0} mesons are modified in the steering mechanism: Masses are set to 3100 MeV, and the decay products $D^{*-}p$ or $D^{*+}\bar{p}$ are forced. No spin is assigned to the particle, i.e. the resonance is assumed to decay isotropically.

1.6.2 DJANGO Monte Carlo

DJANGO [30] is an interface to the Monte Carlo programs HERACLES [31] and LEPTO [32]. Deep-inelastic *ep* scattering can be treated by structure function parametrizations or on the basis of parton distribution functions. QED and QCD radiative effects are included and fragmentation is described by the Lund string model.

Chapter 2

HERA and H1

HERA, the "**H**adron-**E**lektron-**R**ing-**A**nlage" at DESY (Hamburg), came into operation in 1992, and is scheduled to run until 2007. In section 2.1, the HERA accelerator is introduced, while the H1 detector is described in section 2.2. The description is focussed on the detector parts that are relevant for this work.

2.1 HERA: Hadron Electron Ring Accelerator in Hamburg

A schematic view of the DESY site with the HERA accelerator is shown in figure 2.1. HERA is the world's first and only electron-proton collider, probing the proton structure with either electrons or positrons.

Located 30 m below surface level, the circumference of HERA is 6.3 km. Since 1998, electrons and protons are accelerated to energies of 27.5 GeV and 920 GeV, respectively (the proton beam energy was 820 GeV, before 1998). A maximum of 210 bunches, with a time spacing of 96 ns (corresponding to a collision frequency of 10.4 MHz) can be stored in the ring accelerator. HERA reaches a luminosity of $1.5 \cdot 10^{31}$ cm^{-2}s^{-1}. The electron beam is transversely polarized and can be longitudinally polarized in the interaction region.

Three experiments are currently located along the HERA ring accelerator:

HERMES scatters the longitudinally polarized electron beam off polarized gas targets to investigate the spin structure of the nucleon at electron-nucleon center-of-mass energies of 7 GeV.

H1 and ZEUS are multi-purpose detectors to study *ep* collisions at electron-nucleon center-of-mass energies of 318 GeV.

The H1 detector will be described in more detail in the following section.

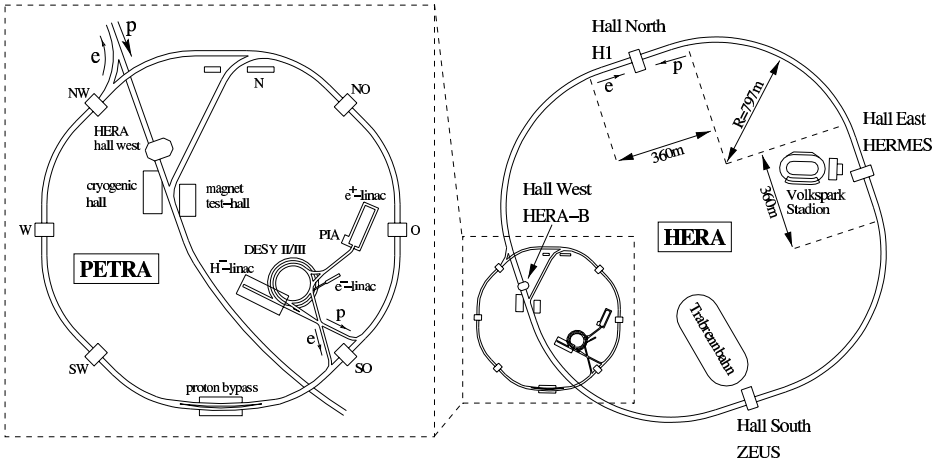

Figure 2.1: The HERA accelerator at DESY in the west of Hamburg

2.2 H1 detector

The H1 detector [33, 34] covers a 4π solid angle range around the nominal interaction point. The detector layout is shown in figure 2.2, together with the H1 coordinate system and the flight direction of protons and electrons.

The right-handed H1 coordinate system has its origin in the interaction point (nominal vertex), the positive z-axis points into the proton's flight direction, the positive x-axis points towards the center of the HERA ring and the positive y-axis points upwards. The *forward* (*backward*) region is defined by small (large) polar angles θ. The H1 detector is cylindrically symmetric around the beam pipe, but asymmetric in the forward-backward direction, because the center-of-mass system is boosted in the proton's flight direction.

The H1 detector consists of different subdetectors, arranged in an onion-like style around the nominal vertex. The main detector parts are listed in the following (going in radial direction from the inner to the outer parts):

- silicon trackers in the central and backward detector part;
- tracking detectors in the central and backward part of the detector;
- a liquid argon calorimeter (LAr) with hadronic and electromagnetic parts in the forward and central part complemented by the plug calorimeter close to the beampipe in the forward direction;

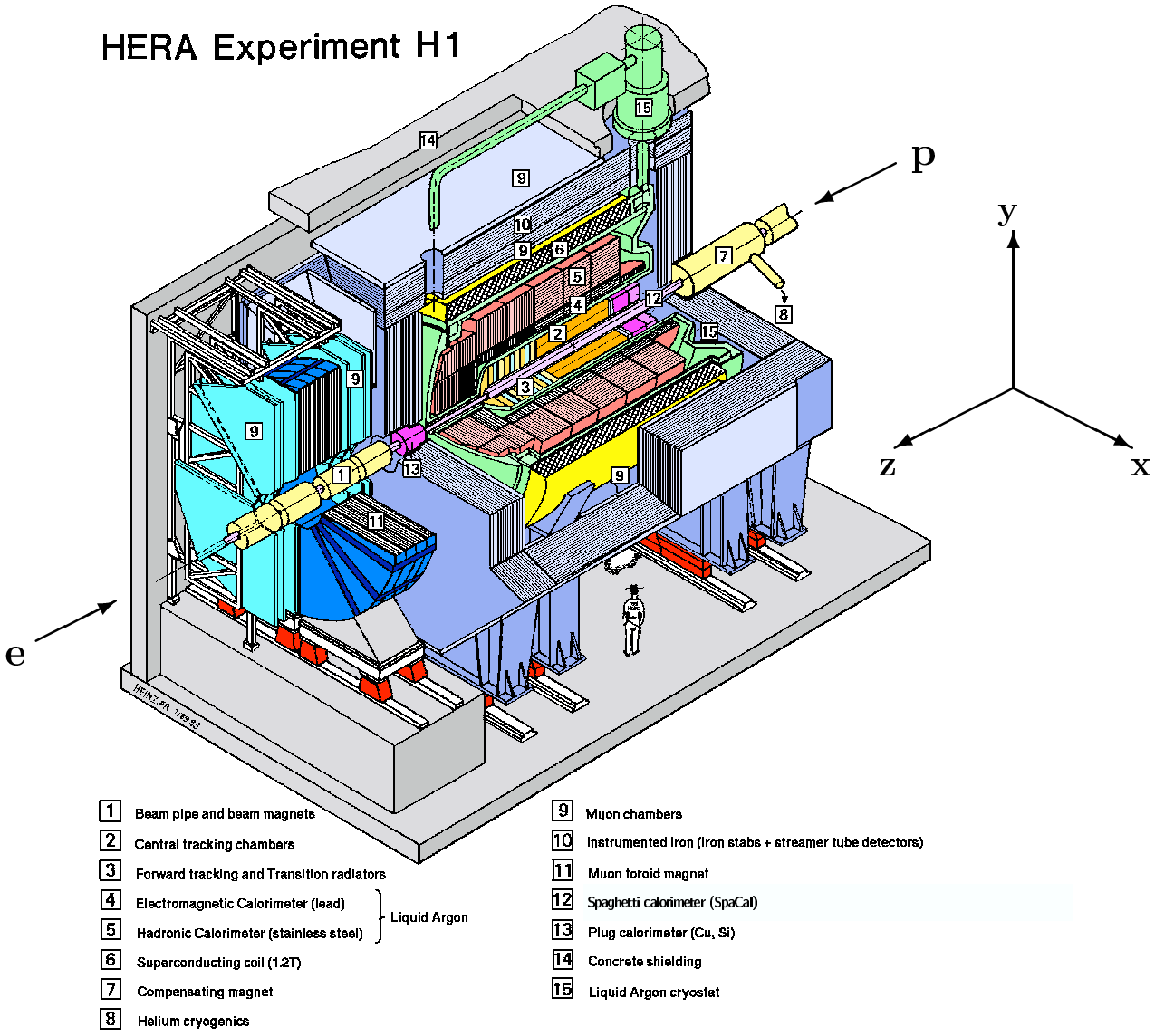

Figure 2.2: The H1 detector, coordinate system and the flight directions of protons and electrons.

- a backward spaghetti calorimeter (SpaCal) behind a backward drift chamber (BDC);
- a superconducting magnetic coil producing a constant magnetic field of 1.15 T;
- an iron yoke to return the magnetic flux instrumented with muon chambers (their purpose is to measure muons and to detect energy from hadronic showers which has not been absorbed by the calorimeters);
- the forward muon system with a toroidal magnet outside of the iron yoke;
- further detectors in the backward tunnel region to detect photons and electrons at very low Q^2 and to measure luminosity.

The H1 tracking system will be described in more detail in section 2.2.1. In section 2.2.2, the electron identification is discussed, while the trigger system is described in section 2.2.3. An overview of the luminosity measurement is given in section 2.2.4.

2.2.1 Tracking

The purpose of the tracking system (see e.g. [33,34]) is to trigger and reconstruct events and to measure momenta of charged particles. The tracking system is divided into three parts to achieve a high track reconstruction efficiency over a maximum angular range: forward, central and backward part. The scattered electron's track is measured in the backward drift chamber (BDC) for a Q^2 below 100 GeV^2.

Tracking detectors

The layout of the H1 tracking system is shown in side view in figure 2.3 and in radial view in figure 2.4. The inner part of the central tracking system consists of the central inner proportional chamber (CIP) and the central inner z-chamber (CIZ). This part is surrounded by the first central jet chamber (CJC1). The outermost part of the central tracking system is built up from the central outer proportional chamber (COP), the central outer z-chamber (COZ) and the second central jet chamber (CJC2). The central tracking system is 2 m long. It covers a polar angular range between 15° and 165° and a radial range of 150 mm $< r <$ 850 mm.

The *z-chambers CIZ and COZ* are thin drift chambers formed by 15 (CIZ) and 24 (COZ) rings of 12(15) cm length in z-direction with four layers

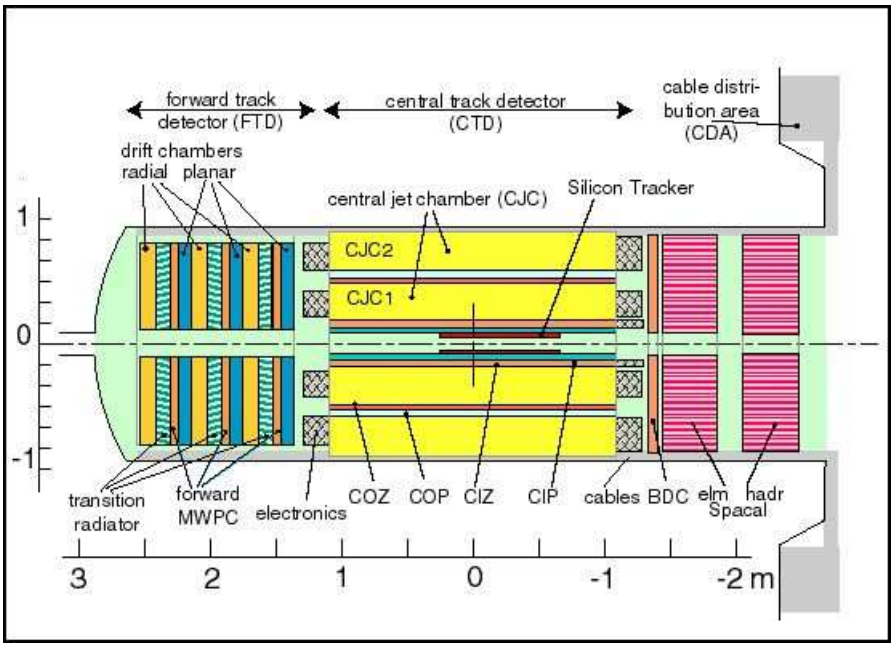

Figure 2.3: Side view of the H1 central tracking system.

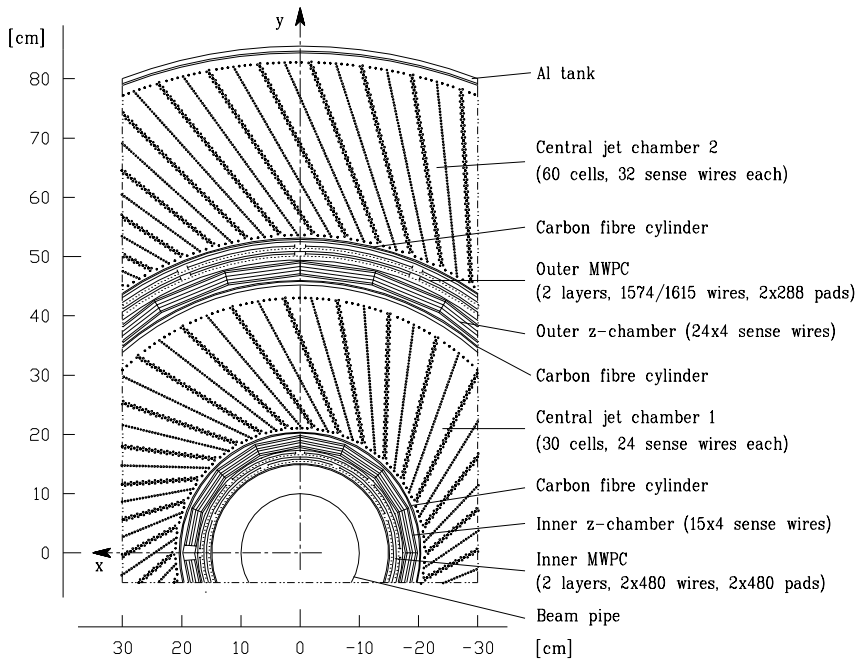

Figure 2.4: Radial view of the H1 central tracking system.

of sense wires in each ring. The signal wires are aligned orthogonal to the beam pipe, so the drift direction is parallel to the z-axis. The internal z-resolution of the z-chambers is about 250 μm at 1 cm drift distance. The $r\phi$-coordinate is measured with an accuracy of $1-2\%$ of 2π.

The *multiwire proportional chambers CIP and COP* are located at the inner radius of the CJC1 and between CJC1 and CJC2, respectively. The central inner proportional chamber (CIP) covers a polar angular range of $9° < \theta < 171°$ and consists of 60 sectors of 36.5 mm length in z-direction and of 8 sectors in ϕ. The angular coverage of the central outer proportional chamber (CIP) is $25° < \theta < 155°$. It is composed of 18 sectors in z-direction of 12.1 cm length and of 16 sectors in ϕ. CIP and COP are used to trigger events with charged particle tracks from the interaction region.

Track reconstruction in the central detector region is performed by the *central jet chambers CJC1 and CJC2* filled with a mixture of argon-ethan gas. The CJC1 (CJC2) consists of 30 (60) "wedge-shaped" drift cells with 24 (32) sense wires strung parallel to the beam axis covering a radial range of 203 mm to 451 mm (CJC1) and 530 mm to 844 mm (CJC2), respectively. The cells are inclined with respect to the radial direction by an angle of 30° to ensure that high momentum tracks from the nominal interaction point going in the radial direction hit more than one drift cell. In the presence of the magnetic field, the ionization electrons drift approximately perpendicular to these tracks, providing an optimal $r\phi$-resolution of about 170 μm at 1 cm drift distance. A z-resolution of 22 mm is achieved by comparing the signal amplitudes readout at both wire ends ("charge division technique", see e.g. [35]). Momenta of charged tracks are measured from the curvature in the magnetic field. The resulting momentum resolution is $\sigma_{p_T}/p_T \approx 0.0005\, p_T/\text{GeV}$. Particles can be identified by their ionization energy loss in the CJC.

Particle identification by ionization energy loss in the jet chambers

The average energy loss per path length of a charged particle in a medium is approximated by the Bethe-Bloch equation:

$$-\frac{dE}{dx} = Cz^2\frac{Z}{A}\frac{1}{\beta^2}\left[\frac{1}{2}\ln\left(\frac{2m_e c^2\beta^2\gamma^2 T_{max}}{I^2}\right) - \beta^2 - \frac{\delta}{2}\right] \tag{2.1}$$

where m, E and p represent the particle's mass, energy and momentum, respectively, $\beta = p/E$ is the particle's velocity in units of c, $\gamma = 1/\sqrt{1-\beta^2} = E/m$, $C = 4\pi N_A r_e^2 m_e c^2$ with N_A being Avogadro's number, r_e the classical electron radius, m_e the electron mass and c the velocity of light; z stands for the charge of the ionizing particle, Z, A and I are atomic number, atomic mass and mean excitation energy of the medium, respectively. T_{max} is the

maximal kinetic energy transfer in a collision of the ionizing particle with a free electron, while δ is a density correction term.

For small β, dE/dx decreases as $1/\beta^2$. The ionization loss is minimal for $3 < \beta\gamma < 4$. For relativistic particles, the ionization loss increases proportional to $\ln\gamma$ until the rise is balanced by density corrections: A plateau of approximately constant energy loss is reached. In figure 2.5, the ionization loss per path length measured in the CJC is shown, normalized to the ionization loss of a minimum ionizing particle.

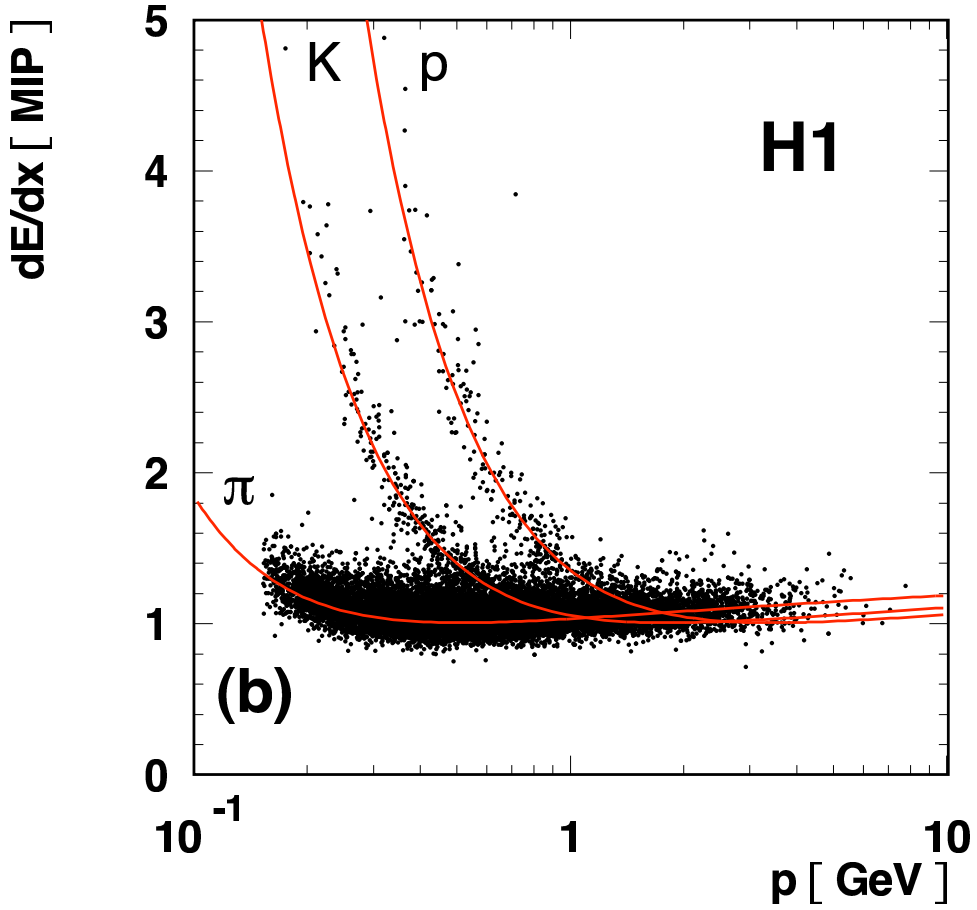

Figure 2.5: Ionisation energy loss per path length normalized to the energy loss of a minimum ionizing particle. The kaon, pion and proton bands are fitted with Bethe-Bloch-like functions according to the most probable CJC response [36].

The specific ionization energy loss of charged particles is derived from the mean of the inverse square-root of the charge collected by all CJC sense wires with a signal above threshold. The resolution is

$$\frac{\sigma(dE/dx)}{dE/dx} \simeq 8\% \tag{2.2}$$

on average for minimum ionizing particles [36].

The information on the ionization energy loss can be transformed into a likelihood for a particular track to be a pion, proton or kaon (this analysis takes only these three hadrons into account). The most probable values for ionization loss are derived from phenomenological parametrizations [36] based on equation 2.1. The normalized pion likelihood is the ratio of the pion likelihood to the sum of pion, kaon and proton likelihoods. Normalized likelihoods for kaons and protons are determined accordingly.

The separation ability S of two particles A and B is defined as

$$S = \frac{dE/dx(A) - dE/dx(B)}{\sigma(dE/dx)} \quad . \tag{2.3}$$

It is shown in figure 2.6 for proton-kaon pairs (upper left panel), pion-proton pairs (upper right panel) and and pion-kaon pairs (lower panel) versus particle momentum (figure taken from [36]). The figure suggests a possible pion-proton separation of $S = 1 - 2$ for particle momenta above 2.5 GeV.

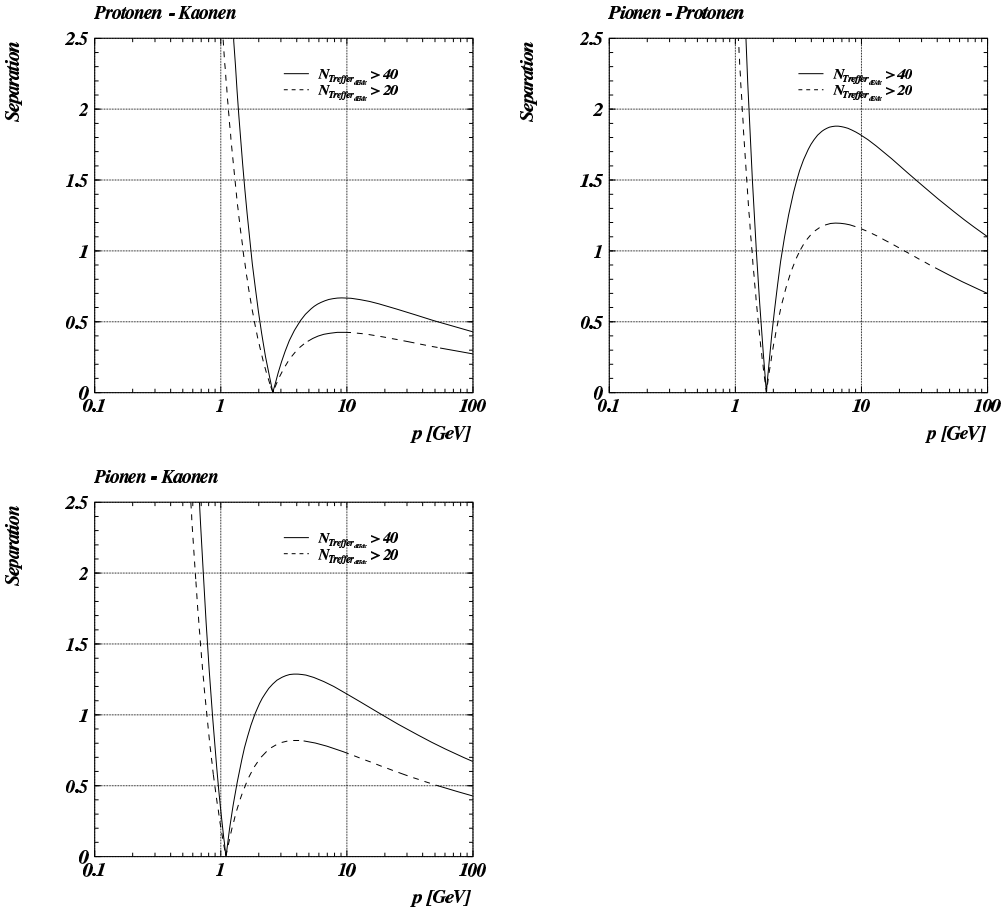

Figure 2.6: Two-particle separation ability S (defined in the text) for proton-kaon pairs (upper left panel), pion-proton pairs (upper right panel) and and pion-kaon pairs (lower panel) versus particle momentum assuming 20 (dashed line) or 40 (solid line) hits (figure from [36]).

Lee-West track reconstruction

Track reconstruction requires a fine resolution of the track's helix parameters. Different track and vertex types are shown in figure 2.7.

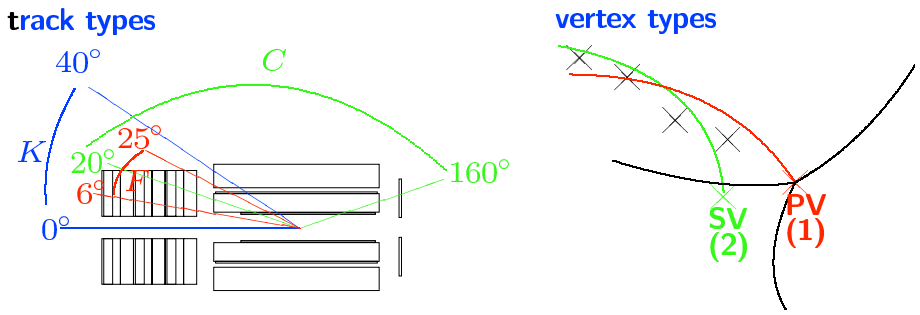

Figure 2.7: Different track (left panel) and vertex (right panel) hypotheses for a single track. The crosses in the right panel symbolize measured space points, being fitted to either the primary vertex (PV) or a secondary vertex (SV).

A track can be a *central track* C (measured only in the central trackers CJC, CST, z-chambers), a *forward track* F (measured only with the FTD) or a *combined track* K (measured in CJC and FTD). The track can be fitted to different vertices (primary vertex PV, secondary vertex SV), where a track fitted to the primary vertex is also called a *central fitted track*. Since the decay lengths of D mesons are not resolved in this analysis, only central fitted tracks are used for this analysis.

The selection cuts for central fitted tracks are listed in table 2.1, where p_T is the transverse momentum of the track, θ the polar angle, d_0 the distance of closest approach to the primary vertex in the $r\phi$ plane, R_{start} the radius of the first CJC hit, R_{length} the radial track length in the CJC and $N_{CJC\,hits}$ the number of hits in the CJC.

2.2.2 Electron identification

The H1 calorimeter system complements the tracking system such that the total energy of all produced particles can be measured. The liquid argon calorimeter performs the basic measurement of hadronic energy and of electromagnetic energy at high Q^2. Hadronic showers leaking out of the liquid argon calorimeter are measured in the tail catcher. The extreme forward direction ($0.6° < \theta < 3°$) is covered by the plug calorimeter. At low Q^2, the electron energy is measured in the spaghetti calorimeter (SpaCal) which

$p_T > 0.12$ GeV
$20° < \theta < 160°$
$\lvert d_0 \rvert \leq 2$ cm
$R_{start} \leq 50$ cm
$R_{length} \geq 10$ cm for $\theta \leq 150°$
$R_{length} \geq 5$ cm for $\theta > 150°$
$N_{CJC\,hits} \geq 0$

Table 2.1: Selection cuts for central fitted tracks

is located in the backward region (as indicated in figure 2.8). It is a lead-scintillating fiber calorimeter and was installed in 1995. The polar range covered by the SpaCal is between 153° and 174°. The spatial resolution is $\sigma_{spatial} = 4.4\text{ mm}/\sqrt{E/\text{GeV}} \bigoplus 1.0\text{ mm}$, while the energy resolution is $\sigma_{energy}/E = 0.07/\sqrt{E/\text{GeV}} \bigoplus 0.01$, where the symbol $\bigoplus$ stands for the squared sum.

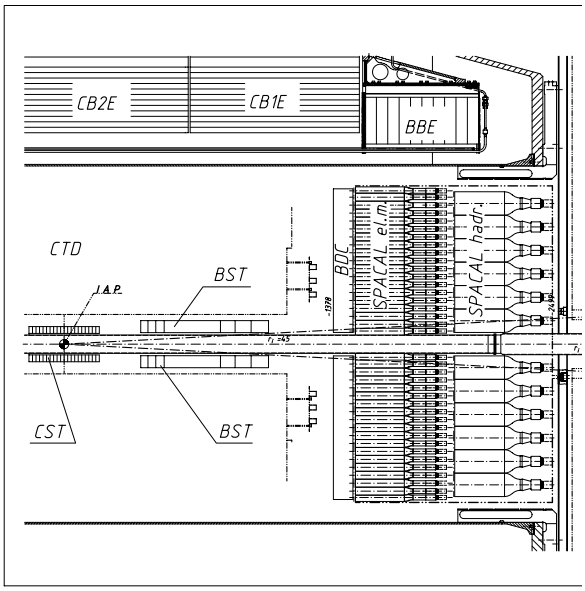

Figure 2.8: Side view of the backward spaghetti calorimeter

A search for electrons is performed in liquid argon and spaghetti calorimeter. The scattered electron is identified from all electron candidates by selecting the candidate which is isolated and has the largest transverse momentum. Further selection cuts are imposed to improve the electron identification and

to suppress background: The reconstructed vertex has to lie within 35 cm of the nominal vertex position to remove the contribution of proton satellite bunches. This selection is made because the vertices stemming from forward and backward satellite bunches are shifted by ±70 cm on average compared to the main bunch. The trigger efficiency decreases for small electron energies, therefore a minimum energy of the scattered electron of 8 GeV is required. The photoproduction background can be suppressed by cutting on the difference between total energy and longitudinal momentum, $E - p_z$, of all central detector particles. Photoproduction background is mostly due to photons from π^0 decays, which are misidentified as scattered electrons. A cut of $E - p_z > 35$ GeV guarantees a detection of all kinematically relevant particles[1]. The selection cuts on the electron identification are summarized in table 2.2.

z-position of primary vertex	$\lvert z_{Vertex}\rvert < 35.0$ cm
energy of the scattered electron	$E_{elec} > 8$ GeV
$E - p_z$ of all central detector particles	$E - p_z > 35$ GeV
photon virtuality	$1\ \text{GeV}^2 < Q^2 < 100\ \text{GeV}^2$
inelasticity	$0.05 < y < 0.7$

Table 2.2: Selection cuts to improve identification of the scattered lepton

2.2.3 Trigger

The *ep* bunch crossing rate at HERA is 10.4 MHz. The purpose of the multi-level H1 trigger system is to filter out physically interesting events, such that the outgoing rate of events from the fourth trigger level does not exceed 10 Hz. The first and second level systems (L1 and L2) are synchronous to the HERA clock. For each bunch crossing, the trigger level L1 decides after 2.3 μs about acceptance or rejection without causing dead time of the detector. General event properties are determined from a subset of the data, encoded in Boolean logics (*trigger elements*). Within 20 μs after the L1 decision to further process the event (*L1-Keep* signal), the L2 trigger decision is made based on a combination of two independent hardware systems. This time is sufficient to transmit the trigger information and to determine the L2 trigger response.

[1] A value of $E - p_z$ significantly below $2 \cdot E_{\text{e beam}}$, where $E_{\text{e beam}}$ is the energy of the $e^{\pm}$ beam, hints to undetected particles in the backward region.

L1 trigger

At every given moment, the detector data from 24 bunch crossings is contained in front-end-pipelines (multi-event buffers). The information is fed into the individual subsystem triggers, where the data are encoded into 256 trigger elements and transmitted to the *central trigger logic*. The pipelined L1 trigger runs deadtime-free at 10.4 MHz synchronous to the HERA clock. Within 2.3 μs after each bunch crossing, a trigger decision is made on this level. The detector information can be related to a specific bunch crossing by the so-called t_0-bit trigger element. Hence, the incoming trigger elements can be synchronized with the central trigger logic to ensure that the trigger decision is only based on information from the same bunch crossing.

The subdetectors set the trigger elements which are used by the central trigger logic for the decision on a further event processing. Furthermore, synchronized timing signals are distributed, which control the subsystem readout such that the pipelined data can be correctly assigned to the corresponding bunch crossing.

The decision on the further event processing (L1-Keep signal) is based on 128 logical combinations (*subtriggers*) of the 256 trigger elements. (This work uses subtrigger 61, which is explained in more detail below.) Each subtrigger condition has to contain one t_0-bit for the correct bunch crossing assignment. The pipelines are stopped and the detector deadtime starts. Data acquisition proceeds in several steps, partly parallel. The L1-Keep signal starts second trigger level (L2) processing. Read-out starts after confirmation by L2 (L2-Keep signal). As soon as the buffer read-out has finished, the pipelines are cleared and reopened.

A subtrigger is *prescaled* by a factor d if it accepts too many events. Out of all events selected by this particular subtrigger, only every d-th event will then be accepted. Subtrigger s61 is used in this analysis. This trigger is described in the next paragraph.

L1 subtrigger 61

Subtrigger 61 (s61) (see e.g. [37]) is used to trigger deep-inelastic scattering events. It is built up from several conditions described in the following:

SpaCal trigger: The *inclusive electron trigger* (IET) sums the energies deposited in the SpaCal to a trigger tower in a *trigger window* of 4×4 neighboring cells. The 320 trigger towers are half overlapping in size in x- and y-direction which avoids trigger inefficiencies as a function of the impact point. The deposited energy is compared to three energy thresholds. Trigger elements are formed in an inner ($R < 16$ cm) and

outer ($R > 16$ cm) region. The subtrigger s61 requires a measured electron in the SpaCal inner or outer region with energy above 6 GeV.

DCRΦ trigger: The DCRΦ trigger uses tracks in the central jet chambers. Out of the 56 wire layers, 10 are used for the trigger: seven in CJC1 and three in CJC2. The wire layer signals are compared to predefined track masks in the $r\phi$-plane to enable a gross decision on the track's charge and momentum range. Positively and negatively charged tracks are separated according to low ($450 \leq p_T \leq 800$ MeV) or high ($p_T \geq 800$ MeV) transverse momentum. At least one fired track mask with $p_T \geq 800$ MeV is required from subtrigger s61.

***z*-vertex trigger:** The z-vertex trigger provides a rough estimate of the ep interaction vertex's z-coordinate by using information of CIP, COP and the first layer of the forward proportional chamber FPC. Straight rays are fitted in 16 ϕ-sectors through the hits in the three proportional chambers. Their intersection points with the z-axis are filled into the 16 bin *z-vertex histogram*. Rays intersecting the region close to the nominal vertex lead to a peak close to $z = 0$ in the z-vertex histogram. Wrong hit combinations yield a random distribution. The trigger condition of s61 is a histogram bin with significantly more entries than the average of the others (see figure 2.9 for illustration).

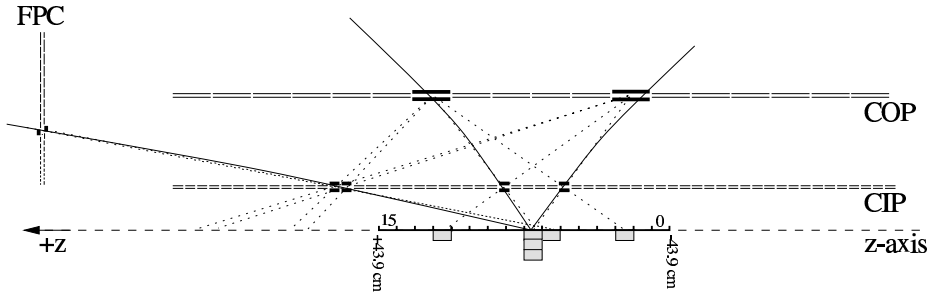

Figure 2.9: z-vertex histogram from extrapolated rays fitted to hits in the proportional chambers. Wrong hit combinations are marked by dotted lines.

L2 trigger

The second trigger level is formed by two separate systems: the *neural network trigger* (L2NN) and the *topological trigger* (L2TT). The L2 trigger

evaluates more complex decisions and suppresses L1 triggers with high rates, thereby reducing the event rate down to 50 Hz. The second level trigger decision is delivered after 20 μs. Data taking restarts immediately if the L2 trigger decision is negative.

L4 trigger

The purpose of the L4 trigger is to filter out obvious background (like e. g. a z-vertex outside the detector acceptance) and to perform as well a complete reconstruction as a classification of the event. Furthermore, the L4 trigger scales down low-Q^2 events, writes out data streams and provides monitoring histograms.

If an event is accepted by the second trigger level, the entire detector information is submitted to the event buffer of the L4 trigger. The L4 trigger consists of a system of microprocessors which decides about the storing of an event to tape. A complete event reconstruction is performed on trigger level 4 and selection cuts on selected decay channels are imposed. After the event builder has finished reading-out the subdetector information, L1 starts to filter the data again. An open charm finder (HQSEL for Heavy Quark SELection) was implemented at Level 4 in 1997. In section 3.2.1, specific selection cuts are listed for the decay channel $D^{*+} \to D^0\pi_s^+$, $D^0 \to K^-\pi^+\rho^0$, $\rho^0 \to \pi^+\pi^-$ (and charge conjugates).

2.2.4 Luminosity measurement

The luminosity is determined from the Bethe-Heitler process $ep \to ep\gamma$ which can be calculated within QED. The Bethe-Heitler cross section in the acceptance range of the luminosity system of the H1 experiment is 70 nb.

The H1 luminosity system [38, 39] consists of two detectors to measure the scattered electron (*electron tagger*) and the radiated photon (*photon detector*), respectively. A scattered electron in the beam pipe is preferred by the Bethe-Heitler kinematics. Hence, the electron tagger is located close to the beam pipe and far from the interaction point ($z = -33$ m). The photon detector is located at $z = -103$ m.

Chapter 3

Reconstruction of D^* mesons in the decay channel $D^* \to K\pi\pi\pi_s$

This chapter describes the reconstruction of D^* mesons in the decay channel $D^{*+} \to D^0\pi_s^+$, $D^0 \to K^-\pi^+\rho^0$, $\rho^0 \to \pi^+\pi^-$ or $D^{*-} \to \bar{D}^0\pi_s^-$, $\bar{D}^0 \to K^+\pi^-\rho^0$, $\rho^0 \to \pi^+\pi^-$. In previous analyses, this decay channel[1] was not exploited with the H1 experiment. After a description of the reconstruction method in section 3.1, all selection cuts are given and motivated in section 3.2. In section 3.3, the analysis of D^* production is described. Differential cross sections for D^* production are determined and compared with measurements in the standard D^* decay channel $D^{*+} \to D^0\pi_s^+$, $D^0 \to K^-\pi^+$ and with Monte Carlo simulations. The data set used to determine the cross sections was recorded in the years 1996 until 2000, corresponding to an integrated luminosity of 75 pb^{-1}.

A measurement of the gluon density in the proton is made possible by the analysis of gluon-induced processes, such as boson-gluon fusion. Hence, a measurement of charmed hadrons provides a method to unfold the proton's gluon content [40]. A high-statistics sample of D^* mesons is therefore desirable to improve the statistical precision on the gluon density. In this analysis, the reconstructed D^* mesons are used to search for charmed pentaquarks in D^*p combinations measured with the H1 detector.

[1] In the following, charge conjugates are always implicitly included.

3.1 Reconstruction method

Measurements of D^* mesons with the H1 experiment employ the standard decay channel for D^* reconstruction,

$$D^{*+} \to D^0\pi_s^+ \quad , \tag{3.1}$$

where D^* mesons decay with a branching ratio of $(67.7 \pm 0.5)\%$ to a D^0 meson and a pion (π_s). Due to the small difference of 145.5 MeV between the nominal masses of D^* and D^0, being just above threshold for π production, the π_s is low-energetic in the D^* center-of-mass system (the notation π_s stands for *slow pion*). Its momentum in the D^* rest frame is below 6 MeV. Analyses of the decay $D^{*+} \to D^0\pi_s^+$ employ this small mass difference, by considering the difference of the reconstructed invariant masses of D^* and D^0, $\Delta M(D^*)$:

$$\Delta M(D^*) = m_{rec}(D^*) - m_{rec}(D^0) \tag{3.2}$$

This way, not all the final-state-particle momenta, but only the slow pion's momentum resolution determines the mass difference resolution.

Previous measurements of D^* mesons with the H1 detector considered the so called "golden decay channel"

$$D^{*+} \to D^0\pi_s^+ \to K^-\pi^+\pi_s^+ \tag{3.3}$$

The non charm-induced background is described by π_s candidates combined with "wrongly charged D mesons", where the like-charged K and π candidates are combined to form a doubly charged D^0 candidate. A comparison of mass difference spectra of D^* candidates and wrong-charge D combinations reconstructed in the "golden decay channel" (3.3) is shown in figure 3.1. The background is well described by wrong-charge D combinations. These are thus used to study background properties and to optimize the selection cuts.

In the years 1999 and 2000, about 2700 D^* mesons decaying via $D^* \to K\pi\pi_s$ have been measured with the H1 detector [3]. To increase the D^* statistics, it has been proposed to reconstruct D^0 mesons in the decay channel

$$D^0 \to K^-\pi^+\pi^+\pi^- \quad . \tag{3.4}$$

This decay channel proceeds dominantly via a ρ^0 resonance:

$$D^0 \to K^-\pi^+\rho^0 \to K^-\pi^+\pi^+\pi^- \quad . \tag{3.5}$$

The branching ratios for the decay channels listed in formulas 3.4 and 3.5 are given in table 3.1. All final state particles are charged and can be measured in the central jet chamber (CJC) of H1.

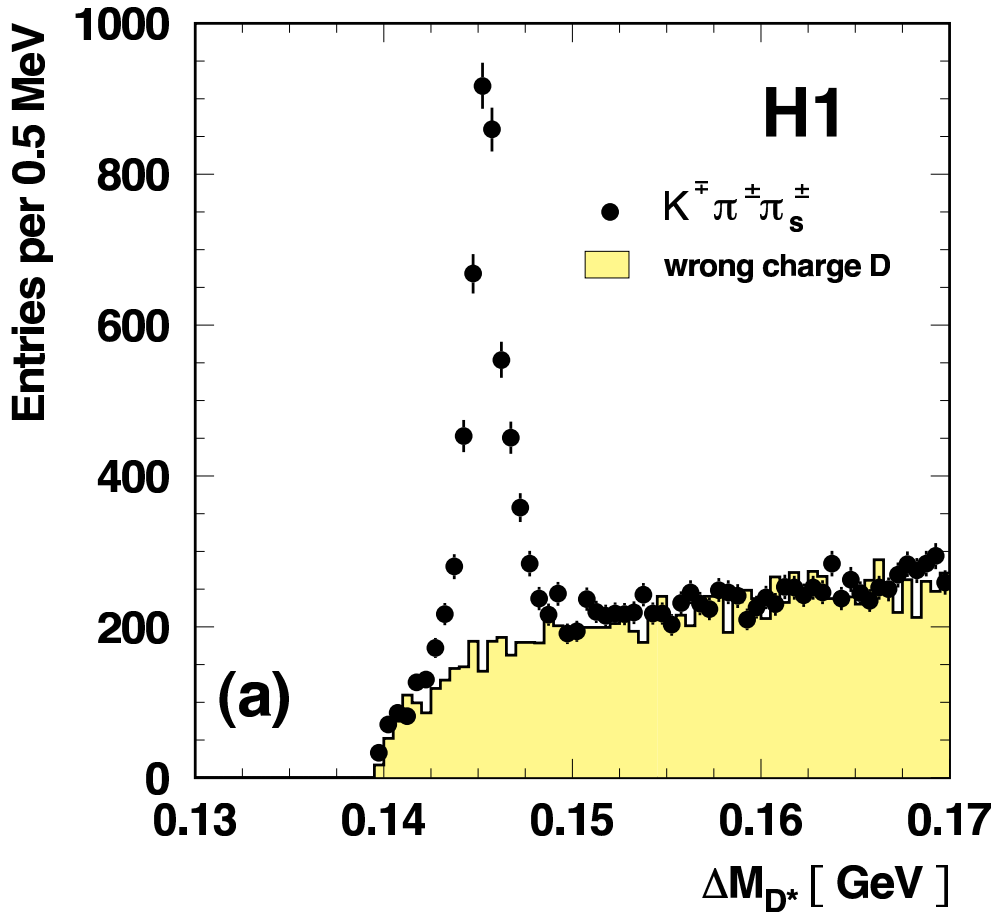

Figure 3.1: D^* mass difference spectrum for the golden decay channel $D^{*\pm} \to D^0(\bar{D}^0)\pi_s^{\pm}$, $D^0(\bar{D}^0) \to K^{\mp}\pi^{\pm}$ (figure from [28]).

	Mass	Branching ratio
D^{*+}	(2010.0 ± 0.5) MeV	$\mathcal{B}(D^0\pi^+) = (67.7 \pm 0.5)\%$
D^0	(1864.6 ± 0.5) MeV	$\mathcal{B}(K^-\pi^+) = (3.80 \pm 0.09)\%$ $\mathcal{B}(K^-\pi^+\pi^+\pi^-) = (7.46 \pm 0.31)\%$ $\mathcal{B}(K^-\pi^+(\rho^0 \to \pi^+\pi^-)) = (6.2 \pm 0.4)\%$

Table 3.1: Branching ratios for the investigated decay modes and masses of D^0 and D^* mesons [2]. Note that the decay $D^0 \to K\pi\rho \to K\pi\pi\pi$ is the dominant decay mode of the decay $D^0 \to K\pi\pi\pi$.

The branching ratio of the decay channel $D^0 \to K\pi\pi\pi$ is about two times the branching ratio of the decay channel $D^0 \to K\pi$. This fact suggests to add the decay channel $D^* \to D^0\pi_s \to\to K\pi\pi\pi\pi_s$ to the H1 analysis framework.

However, the larger number of decay particles leads to a larger combinatorial background in the decay channel $D^* \to K\pi\pi\pi\pi_s$. Requiring an opposite-charge two-pion combination to form a ρ^0 meson introduces an additional constraint, suppressing combinatorial background. This makes D^0 reconstruction in the decay channel $D^0 \to K\pi\rho$ preferable to that in the uncorrelated $K\pi\pi\pi$ decay. The decay $D^{*+} \to D^0\pi_s^+ \to K^-\pi^+\pi^+\pi^-\pi_s^+$ is investigated with and without requiring an intermediate ρ^0 meson.

3.2 Selection cuts

In this section, selection cuts to reconstruct charged D^* mesons in the decay chain $D^{*+} \to D^0\pi_s^+$, $D^0 \to K^-\pi^+\rho^0$, $\rho^0 \to \pi^+\pi^-$ are described. Selection cuts imposed by the open charm finder on trigger level 4 are listed in subsection 3.2.1. Requirements on the track quality and particle identification are described in subsection 3.2.2. Kinematic selections on the D^* daughters are described in subsection 3.2.3. The signal extraction method is presented in subsection 3.2.4 .

This analysis is limited to the DIS kinematic regime, defined by the requirements on the scattered electron:

$$1 \text{ GeV}^2 < Q^2 < 100 \text{ GeV}^2 \text{ and } 0.05 < y < 0.7 \quad .$$

The upper limit on Q^2 is due to the geometric acceptance of the H1 backward calorimeter (SpaCal). Photoproduction events are excluded by selecting $Q^2 > 1$ GeV^2. The y limits exclude regions with high photoproduction background, large radiative corrections and poor y resolution.

3.2.1 Online D^* selection

As mentioned in section 2.2.3, an *open charm finder* (HQSEL for Heavy Quark SELection) was implemented on trigger level 4 in 1997. The imposed selection cuts on the investigated decay channel $D^* \to D^0\pi_s \to K\pi\rho\pi_s \to K\pi\pi\pi\pi_s$ are listed in table 3.2. As the main part of the 1996-2000 data has been recorded with these selections on trigger level, these cuts are also applied for the data taken in 1996.

The reconstructed mass and transverse momentum of the ρ candidate are denoted by $m(\rho)$ and $p_T(\rho)$, respectively, while the reconstructed mass of the D^0 candidate is $m(D^0)$. The D^* mass difference variable as defined

$590\ \text{MeV} < m(\rho) < 950\ \text{MeV}$
$p_T(\rho) > 300\ \text{MeV}$
$1764\ \text{MeV} < m(D^0) < 1964\ \text{MeV}$
$\Delta M(D^*) < 170\ \text{MeV}$
$p_T(D^*) > 2.5\ \text{GeV}$
$z_D(D^*) > 0.1$

Table 3.2: Online selection cuts for the decay chain $D^{*+} \to D^0\pi_s^+$, $D^0 \to K^-\pi^+\rho^0$, $\rho^0 \to \pi^+\pi^-$.

in equation 3.2 is denoted by $\Delta M(D^*)$. The D^*'s transverse momentum is denoted by $p_T(D^*)$, while $z_D(D^*)$ represents the D^*'s production elasticity, defined by

$$z_D = \frac{(E - p_z)_{D^*}}{2 \cdot y \cdot E_{\text{e beam}}} \quad , \tag{3.6}$$

where E and p_z are the energy and longitudinal momentum of the D^* meson and $E_{\text{e beam}}$ is the electron beam energy. The production elasticity is also discussed in section 3.2.3.

3.2.2 Track quality and particle identification

The minimal track conditions on the D^0 daughter tracks are given in table 3.3. The decay lengths of D^* and D^0 are not resolved in this D^* analysis. Tracks therefore have to be fitted to the primary vertex.

track is of type *central fitted*
$R_{length} \geq 25$ cm
$R_{start} \leq 25$ cm
track fit: $\chi^2/\text{ndf} < 10$

Table 3.3: Track selection cuts for D^0 daughters. The variables have been defined in section 2.2.1

The combinatorial background is reduced further by selection cuts on the particle identification. The likelihood that a particle is a pion, kaon or proton is obtained from comparing the measured ionization loss to the most probable value for each particle type at the reconstructed momentum (see section 2.2.1). The normalized pion likelihood is defined as the ratio of the pion likelihood to the sum of pion, kaon and proton likelihoods. Normalized likelihoods for kaons and protons are determined accordingly. The values

are corrected for the different fluxes (pions are more frequent than kaons, kaons are more frequent than protons). The selection cuts on the normalized likelihoods for pions and kaons are given in table 3.4.

$L_K, L_{\pi_s} > 5\%$
$L_\pi, L_{\pi_1}, L_{\pi_2} > 1\%$ for $p < 800$ MeV

Table 3.4: Selection cuts on the normalized likelihoods from ionization loss; π_1 and π_2 are the ρ-daughters

As can be seen in figure 2.5, the dE/dx-bands overlap for large momenta and a separation of pions, kaons and protons based on ionization loss is not possible anymore. The normalized likelihoods for simulated kaon and pion candidates are shown in figure 3.2. It can be seen that the pion identification is reliable for momenta below 800 MeV and is less certain for higher-momentum tracks. Hence, a selection cut on the normalized pion likelihood is only applied for pion momenta below 800 MeV. Due to the low energy of the slow pion only few tracks have a momentum above 800 MeV and a likelihood cut is applied for all momenta. A selection cut $L_K > 5\%$ rejects background from misidentified tracks.

The resolution of the dE/dx-measurement $\sigma\left(\frac{dE}{dx}\right)$ is inversely proportional to the number of hits used for the dE/dx-measurement $N_{\text{CJC hits}}$, i.e. $\sigma\left(\frac{dE}{dx}\right) \propto 1/\sqrt{N_{\text{CJC hits}}}$ [41]. To guarantee a sufficient resolution, $N_{\text{CJC hits}}$ has to be larger than 10 for K, π, π_1 and π_2 (π_1 and π_2 are the ρ daughters). Due to the low energy of the slow pion, its track is short, and $N_{\text{CJC hits}}$ is often less than 10. Therefore no cut is applied on the number of hits used for dE/dx-measurement of the slow pion.

3.2.3 Reconstruction of D^* mesons

In this subsection, the reconstruction algorithm to reconstruct D^* mesons in the decay chain

$$D^{*+} \to D^0\pi_s^+ \ , \ D^0 \to K^-\pi^+\rho^0 \ , \ \rho^0 \to \pi^+\pi^- \tag{3.7}$$

is presented. After a ρ candidate is selected, it is combined with two other tracks (K and π candidates, respectively) to form a D^0 which, combined with a π_s candidate track builds the D^* candidate. The applied selection cuts are motivated by Monte Carlo simulations: A RAPGAP simulation of the decay (3.7) is used to investigate D^* candidate properties, while wrong-charge D combinations in an inclusive DJANGO simulation of deep-inelastic electron-proton scattering are used to investigate the properties of the background.

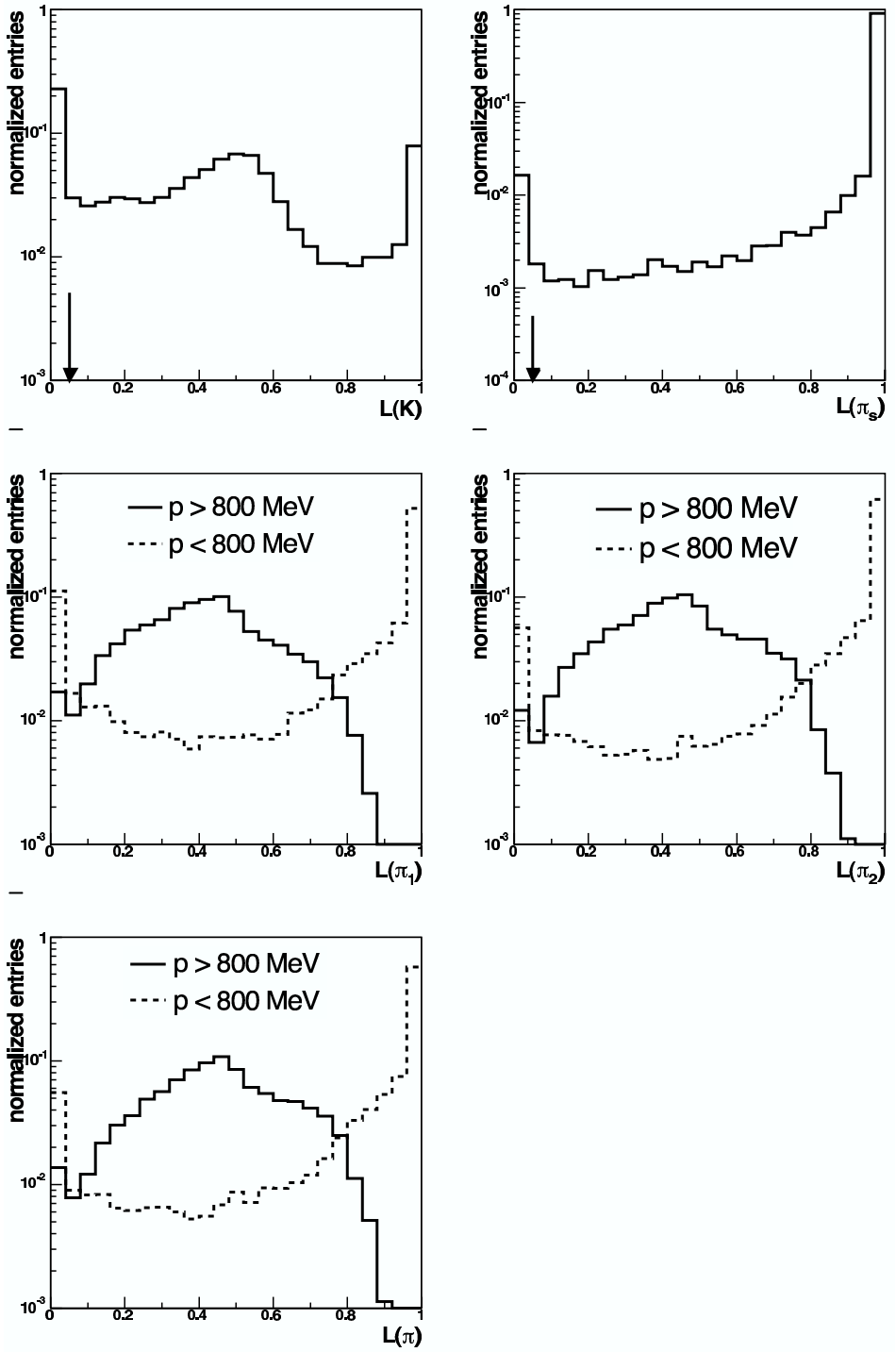

Figure 3.2: Normalized likelihoods from a RAPGAP simulation for kaons (upper left panel), slow pions (upper right panel), ρ-daughters (middle panels) and pions from D^0 candidates (lower panel). The histograms are normalized to the number of entries. The arrows in the upper panels indicate the imposed selection cut on the normalized likelihoods of kaons and slow pions. Normalized likelihoods for pion momenta above and below 800 MeV are shown for π_1, π_2 and π.

After a description of the selection cuts, further selections are proposed to improve the signal-to-background ratio, for example choosing the candidate with the largest fragmentation variable. For comparison, the ρ requirements are dropped and D^* candidates are reconstructed in the decay channel

$$D^{*+} \to D^0\pi_s^+ \ , \ D^0 \to K^-\pi^+\pi^+\pi^- \quad . \tag{3.8}$$

ρ^0 selection

Three charged pion candidate tracks (two positively and one negatively charged or vice versa) can form two possible ρ^0 combinations. The ρ^0 selection chooses one of these combinations and takes the remaining track to be the pion from the D^0.

A loose selection chooses ρ candidates from a mass window of 540 MeV $< m(\rho^0) <$ 1000 GeV and with a transverse momentum above 400 MeV. If this selection is fulfilled by only one combination, the final ρ^0 selection cuts listed in table 3.5 are applied. If, however, both candidates fulfill the crude selection cuts, a tighter selection is imposed. The ρ^0 mass window is narrowed such that the mass difference to the nominal ρ^0 mass has to be less than 170 MeV (600 MeV $< m(\rho^0) <$ 940 MeV). One of the two ρ^0 daughters has to have a transverse momentum larger than 400 MeV, while for the third pion (i.e. the remaining pion not used for the ρ^0):

$$p_T(\pi) > 200 \text{ MeV and } p_T(\pi) > \min(p_T(\pi_1), p_T(\pi_2)) \quad .$$

If this should not decide which tracks to combine to the ρ^0 candidate, the combination with a smaller mass difference to the nominal ρ^0 mass is chosen as the ρ^0 candidate. After a candidate is chosen, the final ρ selection cuts in table 3.5 are applied.

600 MeV $< m(\rho^0) <$ 940 MeV
$p_T(\rho^0) >$ 400 MeV
$p_T(\pi) >$ 200 MeV
$\max(p_T(\pi_1), p_T(\pi_2)) >$ 400 MeV

Table 3.5: Final ρ selection cuts. π_1 and π_2 are the ρ^0 daughters.

Transverse momentum spectra of ρ candidates, ρ daughters and π candidates are shown in figure 3.3. The spectra do not go below 120 MeV due to the Lee-West track selection (see table 2.1). As non-charm background dominates at small transverse momenta, candidates with low transverse momenta

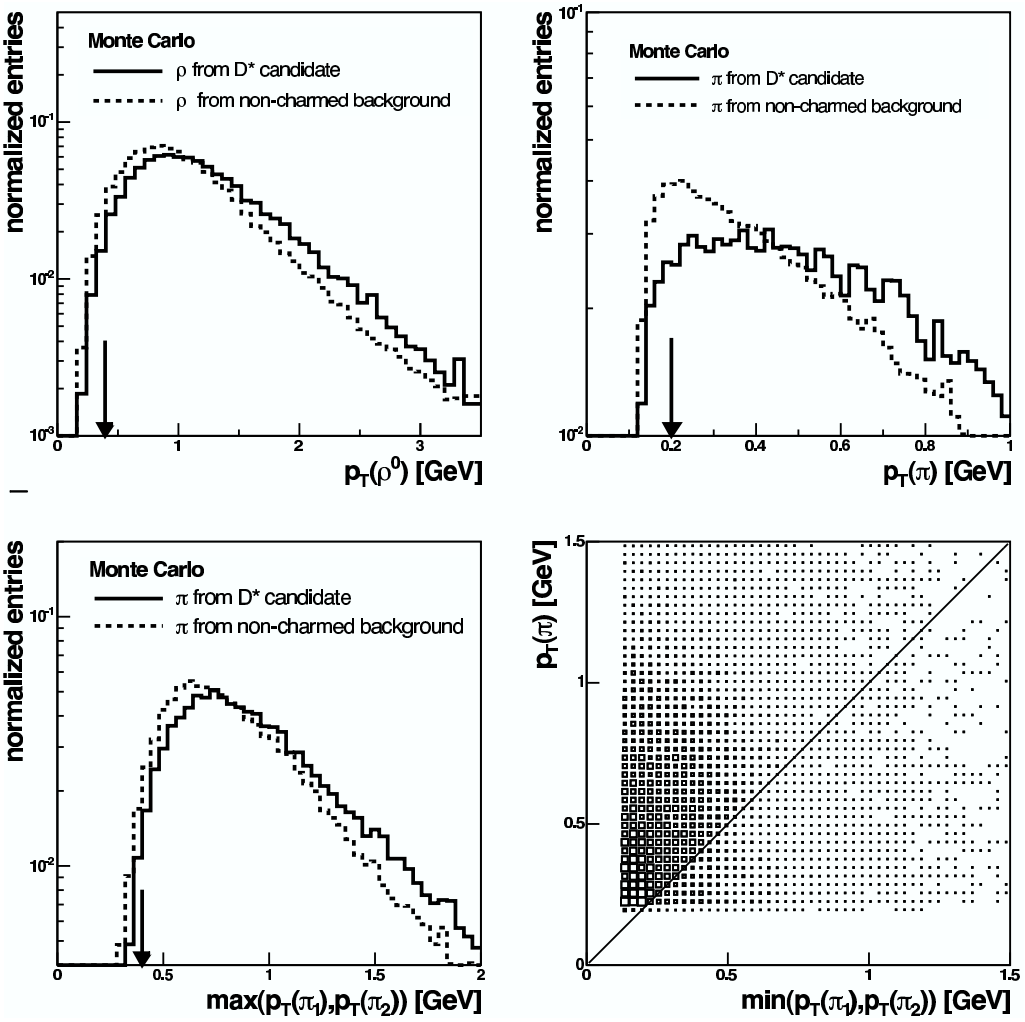

Figure 3.3: Transverse momenta of ρ candidates (upper left panel), ρ daughters (lower left panel) and π candidates (upper right panel) from D^* decays (solid line), compared to transverse momenta of non charm-induced background (dashed line). The histograms are normalized to the number of entries. The pion transverse momentum is shown in the lower right panel versus the minimum transverse momentum of the ρ daughters. The solid line indicates $p_T(\pi) = \min(p_T(\pi_1), p_T(\pi_2))$. D^* candidates are simulated with the RAPGAP Monte Carlo, while non charm-induced background is obtained from a simulation with DJANGO. Arrows indicate imposed selection cuts.

are excluded from this analysis. In the lower right panel of figure 3.3, the transverse momentum of pions from D^0 decay is shown versus the smaller transverse momentum of the ρ daughters. Requiring the pion's transverse momentum to be larger than $\min(p_T(\pi_1), p_T(\pi_2))$ decides between two possible ρ-combinations that both passed the loose ρ-selection, i.e. this selection is only applied as an additional criteria.

D^0 selection

The transverse momentum of the D^0 candidate is required to be larger than 1.5 GeV. A pseudorapidity[2] cut of $|\eta(D^0)| < 2$ selects D^0 mesons from the central region. The D^0 candidate has to have an invariant mass which does not differ by more than 70 MeV from the nominal D^0 mass of 1864 MeV [2]. The sum of the transverse momenta of the final D^0 daughters has to be above 2 GeV, i.e.

$$p_T(\pi_1) + p_T(\pi_2) + p_T(\pi) + p_T(K) > 2 \text{ GeV} \tag{3.9}$$

with π_1 and π_2 being the ρ^0 daughters. The transverse momentum of D^0 candidates is required to be above 1.5 GeV. The sum in (3.9) is shown in the left panel of figure 3.4 for simulated D^0 daughters while the transverse momentum of D^0 candidates is shown in the right panel. The selection cuts exclude the region where non charm-induced background dominates.

The kaon transverse momentum is required to be above 250 MeV. Its spectrum is shown in figure 3.5. The selection cuts imposed on the D^0 and kaon kinematics are summarized in table 3.6.

K	$p_T(K) > 0.25$ GeV
D^0	$\lvert p_T(\pi_1)\rvert + \lvert p_T(\pi_2)\rvert + \lvert p_T(\pi)\rvert + \lvert p_T(K)\rvert > 2.0$ GeV $p_T(D^0) > 1.5$ GeV $-2 < \eta(D^0) < 2$ 1794 MeV $< m(D^0) <$ 1934 MeV

Table 3.6: Selection cuts on D^0 and kaon kinematics: π_1 and π_2 are the ρ^0 daughters. The selection cuts on ρ and π candidates have been listed in table 3.5.

[2]The *pseudorapidity* is defined as $\eta = -\ln\tan\frac{\theta}{2}$ where the polar angle θ is measured relative to the z-axis

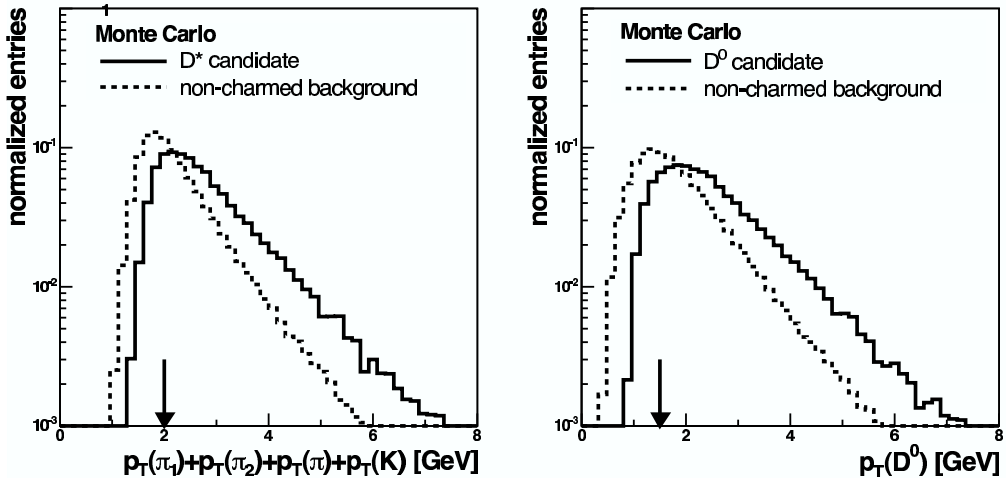

Figure 3.4: Comparison of $\sum p_T(D^0$ daughters) and $p_T(D^0)$ between daughter tracks from D^* candidates (solid line), described by the RAPGAP Monte Carlo, and non charm-induced background (dashed line), described by the DJANGO Monte Carlo. The histograms have been normalized to the number of entries. Selection cuts are indicated by arrows.

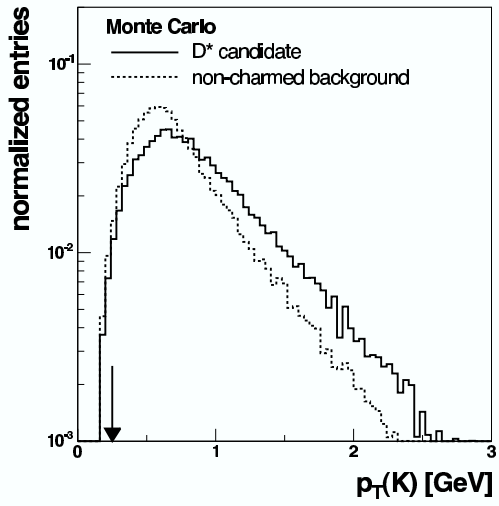

Figure 3.5: Transverse momentum spectrum for kaons from D^* candidates (solid line), described by a simulation with RAPGAP, and non charm-induced background (dashed line), described by a simulation with DJANGO. The histograms have been normalized to the number of entries. The arrow indicates the imposed selection cut.

D^* selection

The D^* daughters are measured in the central detector region. This corresponds to a D^* production in the pseudorapidity region[3] of $-1.5 < \eta(D^*) < 1.0$. Due to the harder charm fragmentation (as will be discussed in the next section), the D^*'s transverse momentum spectrum is harder than for non-charm particles. Hence, the transverse momentum of D^* mesons is restricted to larger values where the combinatorial background is smaller. This is illustrated in figure 3.6, where transverse momenta of simulated D^* candidates are compared to those of non charm-induced background. Only D^* mesons with $p_T(D^*) > 2.5$ GeV are selected for this analysis.

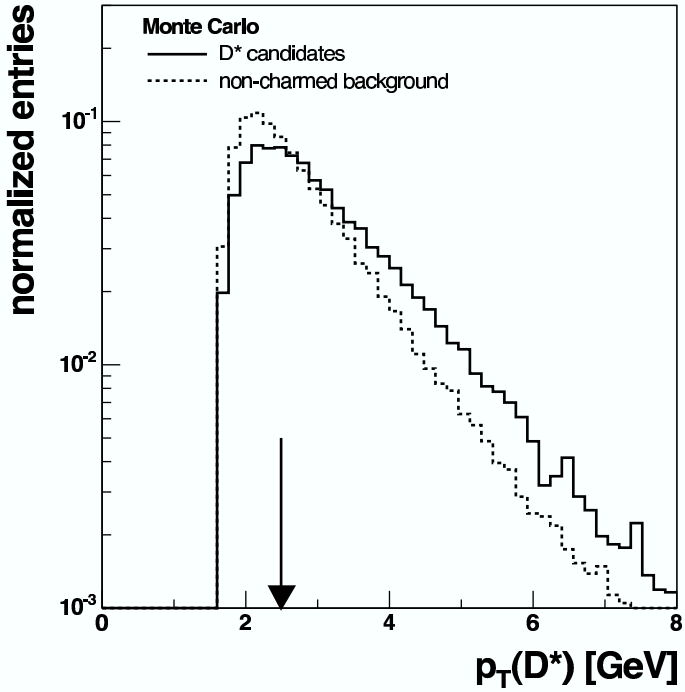

Figure 3.6: Transverse momenta of D^* candidates (solid line), simulated with the RAPGAP Monte Carlo, and non charm-induced background (dashed line), simulated with DJANGO. The histograms have been normalized to the number of entries. Selection cuts on daughter and final state particles are already imposed. The arrow indicates the selection cut $p_T(D^*) > 2.5$ GeV.

[3]The central detector region is defined by the requirement $-1.5 < \eta < 1.5$. D^* candidates in the forward region, corresponding to $1 < \eta(D^*) < 1.5$, are excluded because the non charm-induced background is larger in that region.

On trigger level L4 (see section 2.2.3 and 3.2.1), a selection cut is imposed on the D^* production elasticity z_D. The production elasticity is a convolution of D^* fragmentation and kinematics. Events with $z_D(D^*) > 0.1$ are selected on trigger level. The D^* production elasticity spectrum is shown in figure 3.7. The D^* candidates are observed to have a harder z_D-spectrum than non-charm background due to the harder charm fragmentation into D mesons.

In figure 3.8, invariant mass spectra for D mesons are displayed, after imposing all selection cuts described so far. In this and all further mass difference spectra, the wrong-charge D spectrum is scaled to the number of entries in the range $150 < \Delta M(D^*) < 170$ MeV.

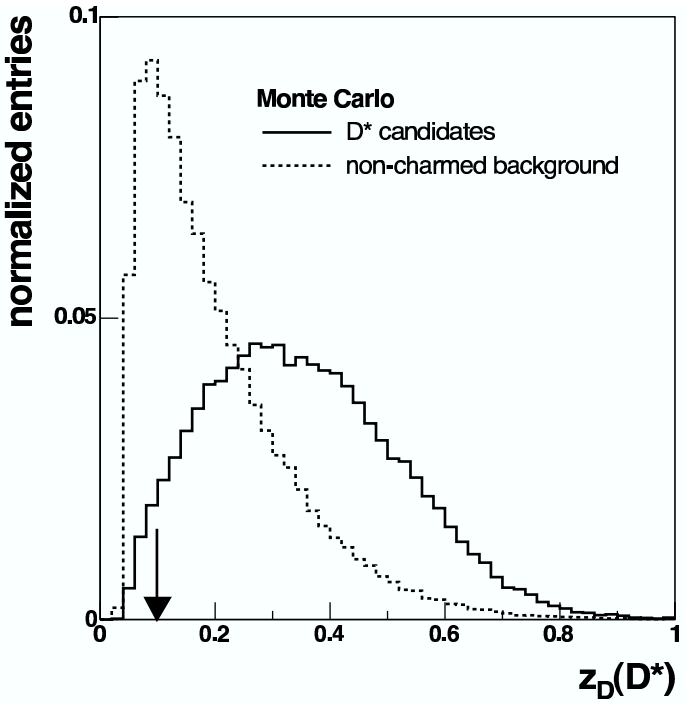

Figure 3.7: z_D-spectra for D^* candidates (solid line) from RAPGAP Monte Carlo and non-charmed background (dashed line) from DJANGO. The histograms have been normalized to the number of entries. The arrow indicates the imposed selection cut.

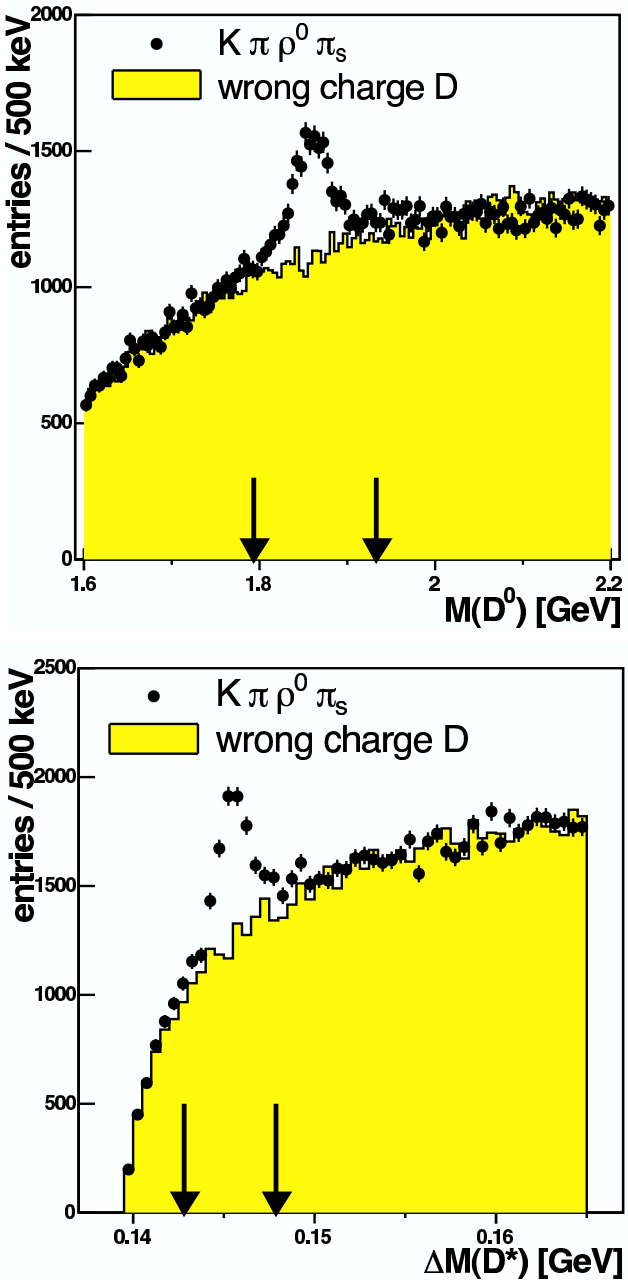

Figure 3.8: D^0 mass spectrum (upper panel) and D^* mass difference spectrum (lower panel) from the data. D^* mesons have been reconstructed in the decay chain (3.7). The D^0 mass spectrum is shown for D^* candidates from the signal region, namely with $142.9 < \Delta M(D^*) < 147.9$ MeV, while the D^* mass difference spectrum is obtained from D^0 candidates with $1794 < M(D^0) < 1934$ MeV (indicated by arrows).

Studies on the charm fragmentation properties

The signal-to-background ratio of the D^* mass difference spectrum is further improved by a cut on the *fragmentation variable* $x_{obs}(D^*)$. Phenomenological models for the fragmentation process have been described in Section 1.4. Charm fragmentation, e.g. into a D^*, is the transformation of a charm quark into a $\bar{d}c$ (or $d\bar{c}$) system. The charm quark defines the D^* kinematics due to its large mass compared to the down quark, i.e. x_{obs} describing the energy fraction of the produced meson with respect to the mother quark is expected to peak close to 1. This is not the case for light mesons, consisting of constituent quarks of comparable masses, therefore a soft fragmentation spectrum is observed. The different fragmentation properties of light quarks and heavy quarks are used to differentiate non charm-induced from charm-induced processes.

The fragmentation variable $x_{obs}(D^*)$ is not unambiguously defined for D^* mesons from boson-gluon fusion. A suitable approximation of the charm quark's energy would be given by the energy of the D^* jet. Another approximation which also includes gluons emitted by the charm quark is the *hemisphere method* [42]: Here, the energy of the charm quark is approximated by the energy of all particles in a suitable hemisphere including the D^* meson. The hemisphere method is used as follows (see also figure 3.9 for illustration):

- All particles in the photon hemisphere are projected into the plane perpendicular to the photon direction.

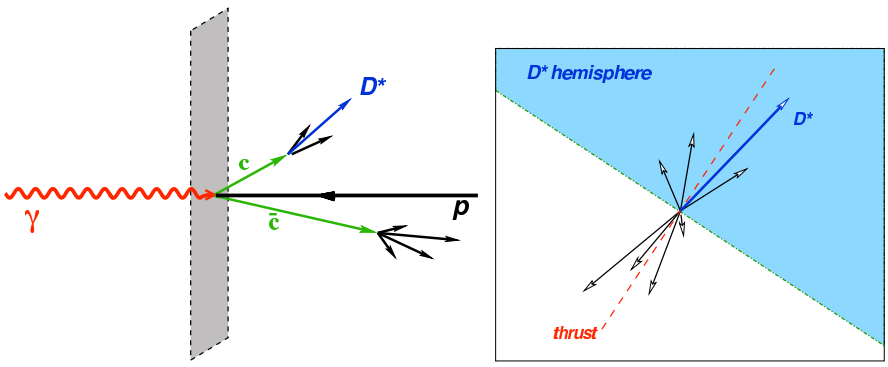

Figure 3.9: Illustration of the hemisphere method: The transverse momenta of charm quark and anti-charm quark in the hadronic center-of-mass are opposite to each other. The event is accordingly divided into two hemispheres.

- In a boson-gluon fusion process, the two charm quarks (i.e. the charm and the anti-charm quark) have opposite transverse momenta in the hadronic center-of-mass frame[4]. The two hemispheres of charm and anti-charm quark are found by determining the *thrust*[5] axis in the plane orthogonal to the photon direction, and by dividing the plane perpendicular to the thrust axis.

- The four-vectors of all particles in the D^* hemisphere are summed. The energy of the obtained hemisphere four-vector approximates the energy of the charm quark (before radiating final state gluons).

- The fragmentation variable $x_{obs}(D^*)$ is calculated from

$$x_{obs}(D^*) = \frac{(E - p_z)_{D^*}}{(E - p_z)_{hemisphere}} \quad . \tag{3.10}$$

In figure 3.10, the fragmentation variable $x_{obs}(D^*)$ is shown for D^* mesons from a RAPGAP simulation and for non-charm background from a DJANGO simulation. It is noticeable that non-charmed background is strongly dominating for a small fragmentation variable x_{obs} as expected and discussed in section 1.4. This observation motivates a cut on the fragmentation variable $x_{obs}(D^*)$ to suppress background.

The $\Delta M(D^*)$ spectrum for a D^* fragmentation variable above and below 0.5 is shown in figure 3.11. The non-charmed background for small $x_{obs}(D^*)$ limits the sensitivity to measure D^* mesons and no signal can be seen for a fragmentation variable $x_{obs}(D^*) < 0.5$, therefore candidates with a fragmentation variable in this range are excluded from this analysis. If not explicitly stated otherwise, this cut is always applied from now on.

[4]The hadronic center-of-mass frame is the center-of-mass frame of photon and proton. Hence, this inertial system is often also called γp frame.

[5]The thrust T is defined as $T = \max_{\vec{n}}(\sum_i |\vec{p}_i \cdot \vec{n}|)/(\sum_i |\vec{p}_i|)$ where the $\vec{p}_i$ are the three-momenta of the tracks and $\vec{n}$ is the direction which maximizes T. The vector $\vec{n}$ is called thrust axis.

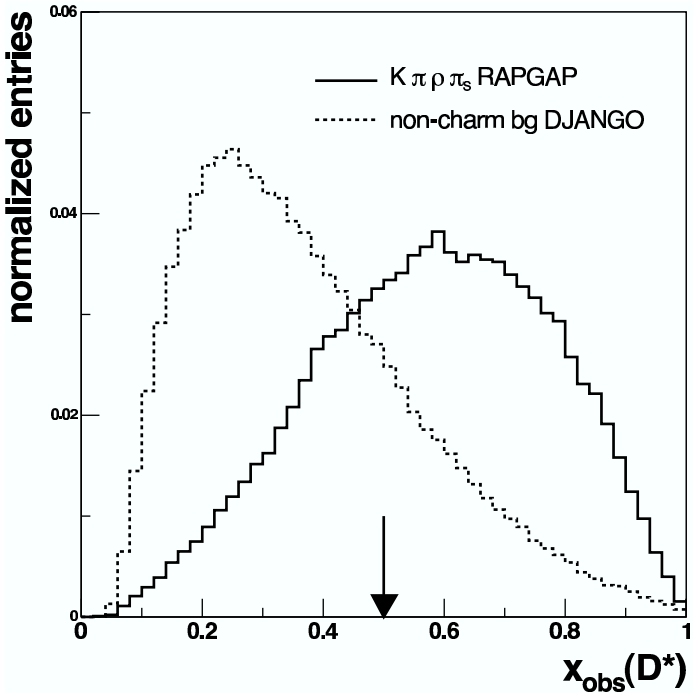

Figure 3.10: Fragmentation spectra for simulated D^* candidates (RAPGAP, solid line) and non-charm background (DJANGO, dashed line). The arrow indicates the imposed selection cut.

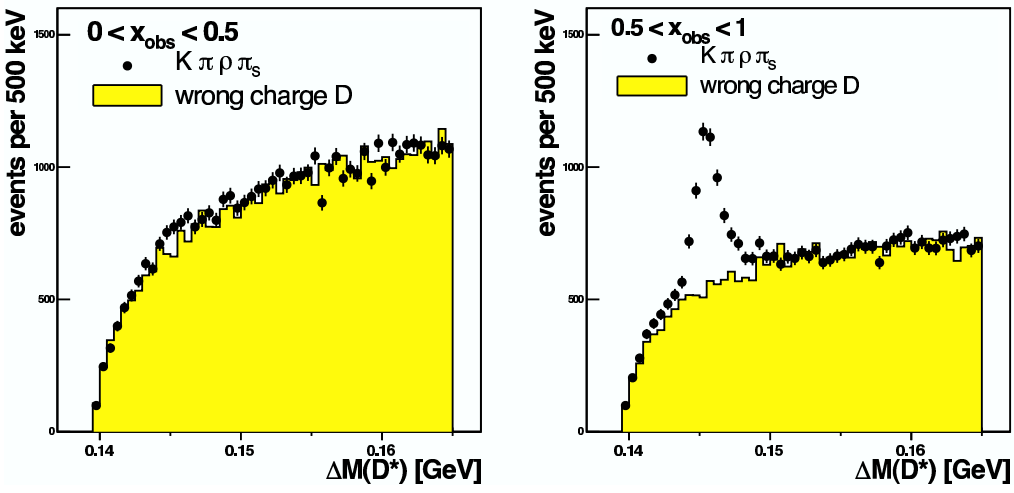

Figure 3.11: $\Delta M(D^*)$ spectra for a D^* fragmentation variable $x_{obs}(D^*)$ below and above 0.5. D^* mesons are reconstructed in the decay channel $D^* \to K\pi\rho\pi_s$.

Further studies and reconstruction of $D^* \to K\pi\pi\pi_s$

It will be interesting to see, whether a ρ signal can be reconstructed back for the corresponding D^* daughters: In figure 3.12, mass spectra for ρ mesons from D^* candidates and from non charm-induced background are shown. All ρ^0 mass window cuts have been relaxed for these studies, while $\Delta M(D^*)$ is required to lie in a ± 2.5 MeV window around the nominal value. The ρ candidate is selected by a smaller difference to the nominal ρ mass. Such a decision leads to an accumulation around the nominal mass also in the combinatorial background as can be seen in figure 3.12. The left panel shows mass spectra for simulated ρ candidates, the right panel shows mass spectra for ρ candidates in the data. A peak is observed at the expected mass with the expected width, in both simulation and data. The data exhibit a steplike structure due to a selection cut on the invariant ρ mass applied on trigger level L4 (see section 3.2.1): The ρ candidate's invariant mass is required to fulfill 590 MeV $< m(\rho) <$ 950 MeV.

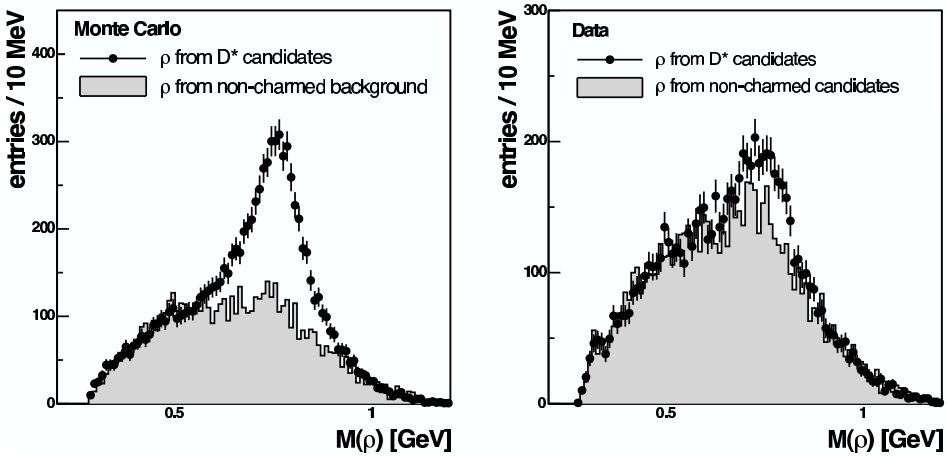

Figure 3.12: Mass spectra for ρ mesons from D^* candidates and non-charmed background. In the left panel, results from a Monte Carlo simulation are shown. D^* candidates are simulated by RAPGAP, while non-charmed background is modeled with DJANGO. Mass spectra from the data are shown in the right panel.

The decay $D^{*+} \to D^0\pi_s^+$, $D^0 \to K^-\pi^+\pi^+\pi^-$ has been reconstructed for comparison: Four tracks are combined to form a D^0 which is then combined with a π_s candidate track to form a D^* candidate. In figure 3.13, the D^* mass difference spectrum of D^* candidates reconstructed in the decay channel $D^* \to K\pi\rho\pi_s$ is compared to that of D^* candidates reconstructed in the decay channel $D^* \to K\pi\pi\pi\pi_s$. All selection cuts applied for the $K\pi\rho$ decay

affecting only one of the pions from the D^0 have been omitted in the reconstruction of the decay $D^* \to K\pi\pi\pi\pi_s$: A $K\pi\rho$ selection like e.g. $p_T(\pi) > 0.2$ GeV is only applied to the pion from the D^0 decay, but not to the ρ daughters. Hence, this particular selection cut on the pion's transverse momentum is omitted in the reconstruction of the decay $D^* \to D^0\pi_s \to K\pi\pi\pi\pi_s$.

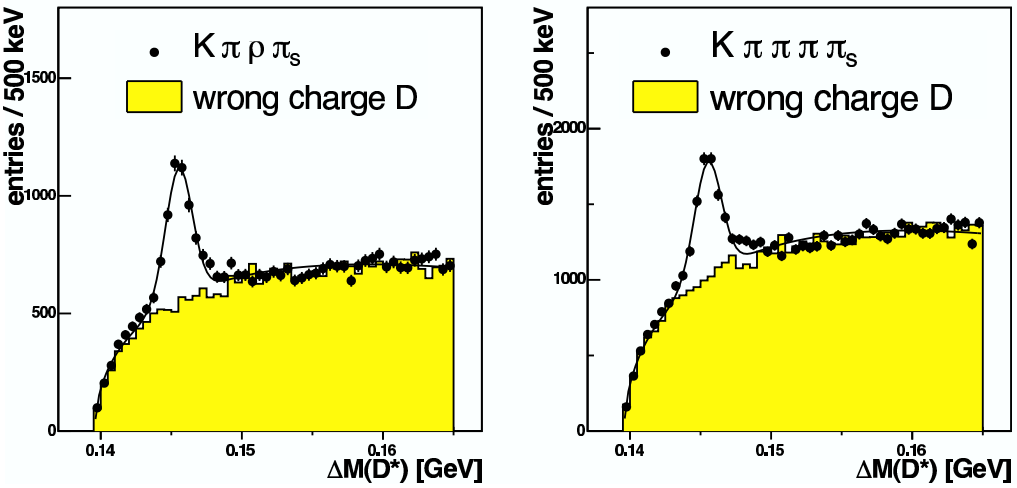

Figure 3.13: D^* mass difference spectra for the decay channels $D^* \to K\pi\rho\pi_s \to K\pi\pi\pi\pi_s$ (left panel) and $D^* \to K\pi\pi\pi\pi_s$ (right panel).

A fit (see section 3.2.4 for details on the signal extraction) to the $\Delta M(D^*)$ distributions yields a signal to background ratio of 0.36 for the decay channel $D^* \to K\pi\rho\pi_s$ and 0.24 for the decay channel $D^* \to K\pi\pi\pi\pi_s$. The total numbers of signal and background events for both decay channels are given in table 3.7. The ratio of signal events reconstructed in the decay channel $K\pi\rho\pi_s$ to those reconstructed in the decay $K\pi\pi\pi\pi_s$ is 73%, while the branching ratios in table 3.1 suggest a ratio of 83%. A correction of these numbers for different acceptances in both decay channels has not been performed, since only the decay channel $D^0 \to K\pi\rho \to K\pi\pi\pi\pi_s$ has been simulated. Nevertheless, the acceptance is expected to be larger for the inclusive $K\pi\pi\pi\pi_s$ decay, since the selection cuts on the ρ-combination are dropped. The ratio of acceptance corrected yields in both decay channels will thus be closer to the branching ratio estimate.

The larger combinatorial background in the decay channel $D^* \to D^0\pi_s$, $D^0 \to K\pi\pi\pi$ might just come from a multiple filling of the same track combination, i.e. five tracks being used with different mass hypotheses for the individual tracks. In particular, taking a slow pion candidate as another pion

	$K\pi\rho\pi_s$	$K\pi\pi\pi\pi_s$
signal events	2638 ± 122	3603 ± 168
background events	7366 ± 778	15087 ± 1186
S/B ratio	0.36	0.24

Table 3.7: Total numbers of D^* candidates from signal and background events for the discussed decay channels.

daughter, and vice versa, will result in the same D^* candidate. The frequency of such a case is studied in figure 3.14. As can be seen in the left panel, the

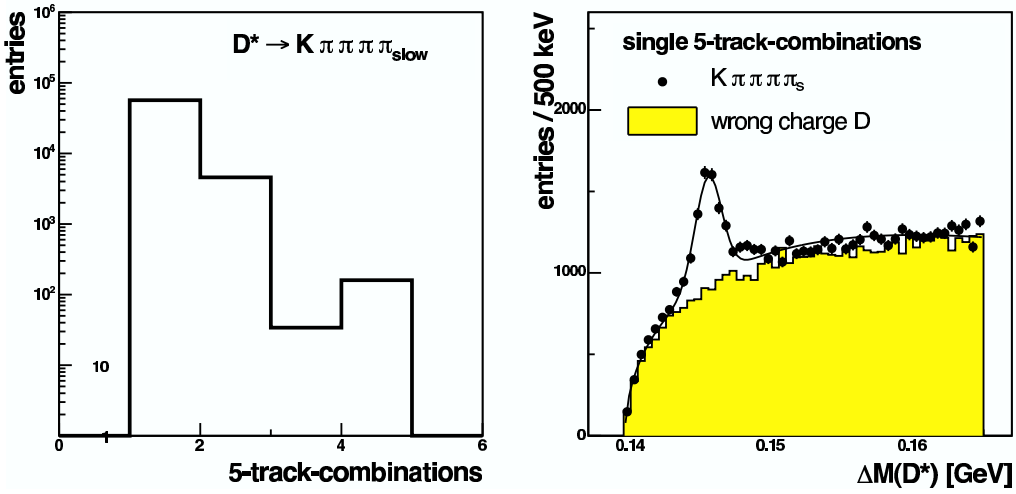

Figure 3.14: Number of five-track-combinations interpreted as different D^* candidates in the decay $D^* \to K\pi\pi\pi\pi_s$ (left panel) and D^* mass difference spectrum from D^* candidates, whose five-track-combination is used only once (right panel).

contribution from multiple filled 5-track-combinations to the $\Delta M(D^*)$ spectrum is about 10%. The right panel shows the D^* mass difference spectrum from D^* candidates whose daughter tracks are filled only once in this particular combination, i.e. the D^* candidate is unique. A fit yields a signal to background ratio of 0.24. Hence, the smaller signal-to-background ratio of the decay channel $D^* \to D^0\pi_s$, $D^0 \to K\pi\pi\pi$ is not caused by a multiple filling of 5-track-combinations.

The better signal-to-background ratio in the $D^0 \to K\pi\rho$ decay channel as well as the observed ρ^0 signal in the D^* mass window motivate the original choice of the decay channel (3.7): The additional mass constraint of the observed intermediate ρ meson provides a better signal-to-background ratio.

Additional studies to improve the D^* signal

The larger number of particles in the $K\pi\pi\pi\pi_s$ final state as compared to the $K\pi\pi_s$ final state (five particles versus three particles) leads to a larger D^* candidate multiplicity in the decay channel $D^* \rightarrow K\pi\pi\pi\pi_s$. To overcome this problem, a candidate can be chosen based on the charm fragmentation behaviour: The candidate with the largest fragmentation variable $x_{obs}(D^*)$ or production elasticity $z_D(D^*)$ is chosen as the best candidate.

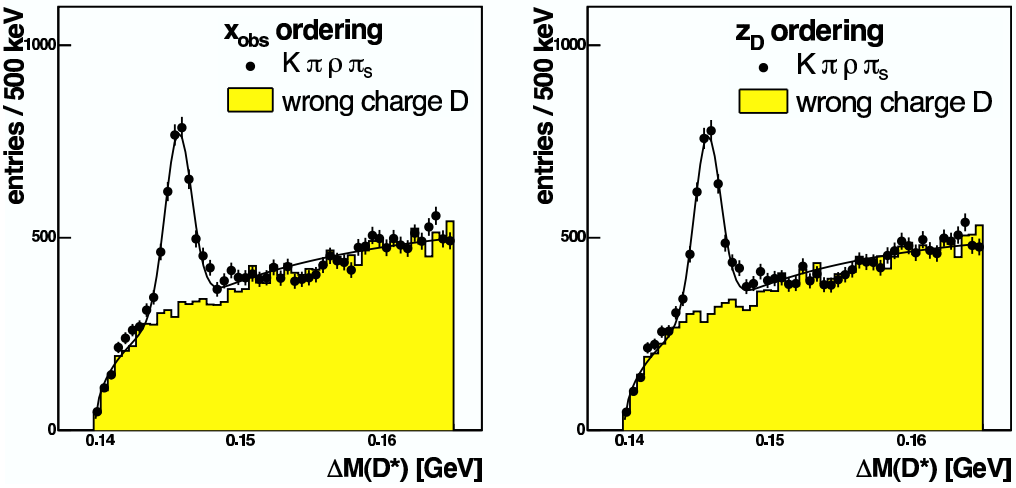

Figure 3.15: Mass difference spectra for D^* candidates selected by the largest fragmentation variable (left panel) or largest production elasticity (right panel)

D^* mass difference spectra for two different candidate selections are shown in figure 3.15: The D^* candidates used for the left panel have the largest fragmentation variable $x_{obs}(D^*)$. The D^* candidates shown in the right panel have the largest production elasticity $z_D(D^*)$. A fit yields a signal to background ratio of 0.64 for the x_{obs} ordering case, and 0.58 for the z_D ordering case. The numbers of signal and background events for both ordering methods are given in table 3.8.

A selection by maximal fragmentation variable is more appropriate because it is directly connected to the charm fragmentation unlike the production elasticity which is a convolution of charm fragmentation and D^* kinematics. Such a selection would provide a greatly improved signal-to-background ratio.

	$x_{obs}(D^*)$ ordering	$z_D(D^*)$ ordering
signal events	2164 ± 95	2144 ± 92
background events	3400 ± 444	3668 ± 513
S/B ratio	0.64	0.58

Table 3.8: Total numbers of D^* candidates from signal and background events for two ordering methods.

3.2.4 Signal extraction

The number of D^* mesons in the signal is extracted from a fit to the D^* mass difference distribution $\Delta M(D^*)$ in the range [141 MeV, 165 MeV]. The fit function $f(x)$

$$f(x) = \underbrace{N_{D^*} \frac{d\Delta M}{\sqrt{2\pi}\sigma_{\Delta M}} \exp\left(-\frac{(x - \langle \Delta M \rangle)^2}{2\sigma^2_{\Delta M}}\right)}_{\text{signal term}} + \underbrace{f_{bg}(x)}_{\text{background term}} \tag{3.11}$$

is used, where $N(D^*)$ is the number of D^* mesons, $\sigma_{\Delta M}, \langle \Delta M \rangle$ are signal width and mean value and f_{bg} is an appropriate background description, respectively. The bin width of the ΔM histogram used for the fit is $d\Delta M$. The free parameters of the fit are N_{D^*}, $\sigma_{\Delta M}$, $\langle \Delta M \rangle$ and the parameters of f_{bg}. In figure 3.16, a fit to the $\Delta M(D^*)$ spectrum is shown with the background description

$$f_{bg}(x) \quad = \quad \alpha(x - m_\pi)^\beta e^{-\gamma(x - m_\pi)} \qquad .$$

The data points are well described by the fit. The resulting parameters are given in table 3.9. In the years 1996-2000, a total number of 2638 ± 122 D^* mesons has been measured in the decay channel $D^{*+} \to D^0\pi_s^+$, $D^0 \to K^-\pi^+\rho^0$, $\rho^0 \to \pi^+\pi^-$. The experimental width is determined to be 0.95 ± 0.05 MeV, while the signal position is correctly fitted to $\langle M \rangle = 145.5$ MeV.

Number of D^* mesons N_{D^*}	2638 ± 122
Mean value $\langle M \rangle$	145.5 MeV
Signal width $\sigma_{\Delta M}$	0.95 ± 0.05 MeV
α	7366 ± 778
β	0.47 ± 0.02
γ	24.5 ± 2.1

Table 3.9: Fitted parameters of the D^* mass difference spectrum.

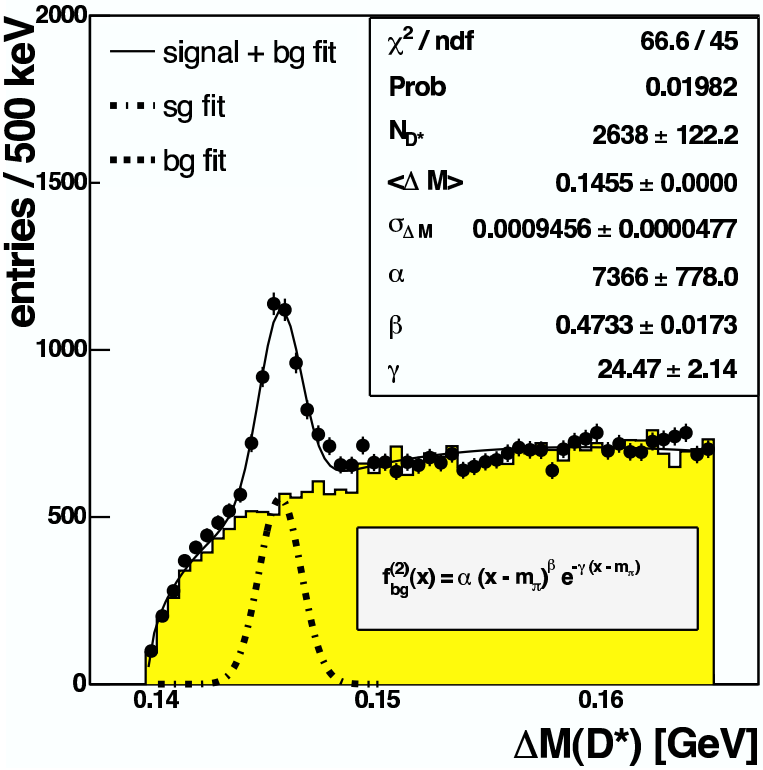

Figure 3.16: Fit to the D^* mass difference spectrum.

3.3 Analysis of D^* production

In this section, results of the analysis of the decay

$$D^{*+} \to D^0\pi_s^+ \ , \ D^0 \to K^-\pi^+\rho^0 \ , \ \rho^0 \to \pi^+\pi^- \tag{3.12}$$

are presented. D^* meson yields in data and simulation are determined in subsection 3.3.1. In subsection 3.3.2, the overall detector acceptance is determined from Monte Carlo simulations with RAPGAP. Differential cross sections are shown in subsection 3.3.3. The results are discussed in subsection 3.3.4.

3.3.1 Determination of D^* meson yields

D^* meson yields from data collected with the H1 detector in the years 1996 until 2000 are shown in figure 3.17 in bins of different kinematic variables. For comparison, yields are shown for the decay channels

$$D^{*+} \to D^0\pi_s^+ \quad , \quad D^0 \to K^-\pi^+\pi^+\pi^- \quad , \tag{3.13}$$
$$D^{*+} \to D^0\pi_s^+ \quad , \quad D^0 \to K^-\pi^+ \quad \text{and} \tag{3.14}$$
$$D^{*+} \to D^0\pi_s^+ \quad , \quad D^0 \to K^-\pi^+\rho^0 \ , \ \rho^0 \to \pi^+\pi^- \quad . \tag{3.15}$$

Without requiring an intermediate ρ^0 candidate (3.13), a larger number of D^* candidates is measured. The number of D^* candidates in the "golden decay channel" (3.14) is compatible with the number of D^* candidates in the $K\pi\rho$ decay channel (3.15). Hence, adding the $K\pi\rho$ channel to standard D^* analyses will double the D^* statistics.

In figure 3.18, yields from D^* mesons reconstructed in the decay channel (3.15) are compared to a Monte Carlo simulation with the RAPGAP program. The data are well described by the simulation.

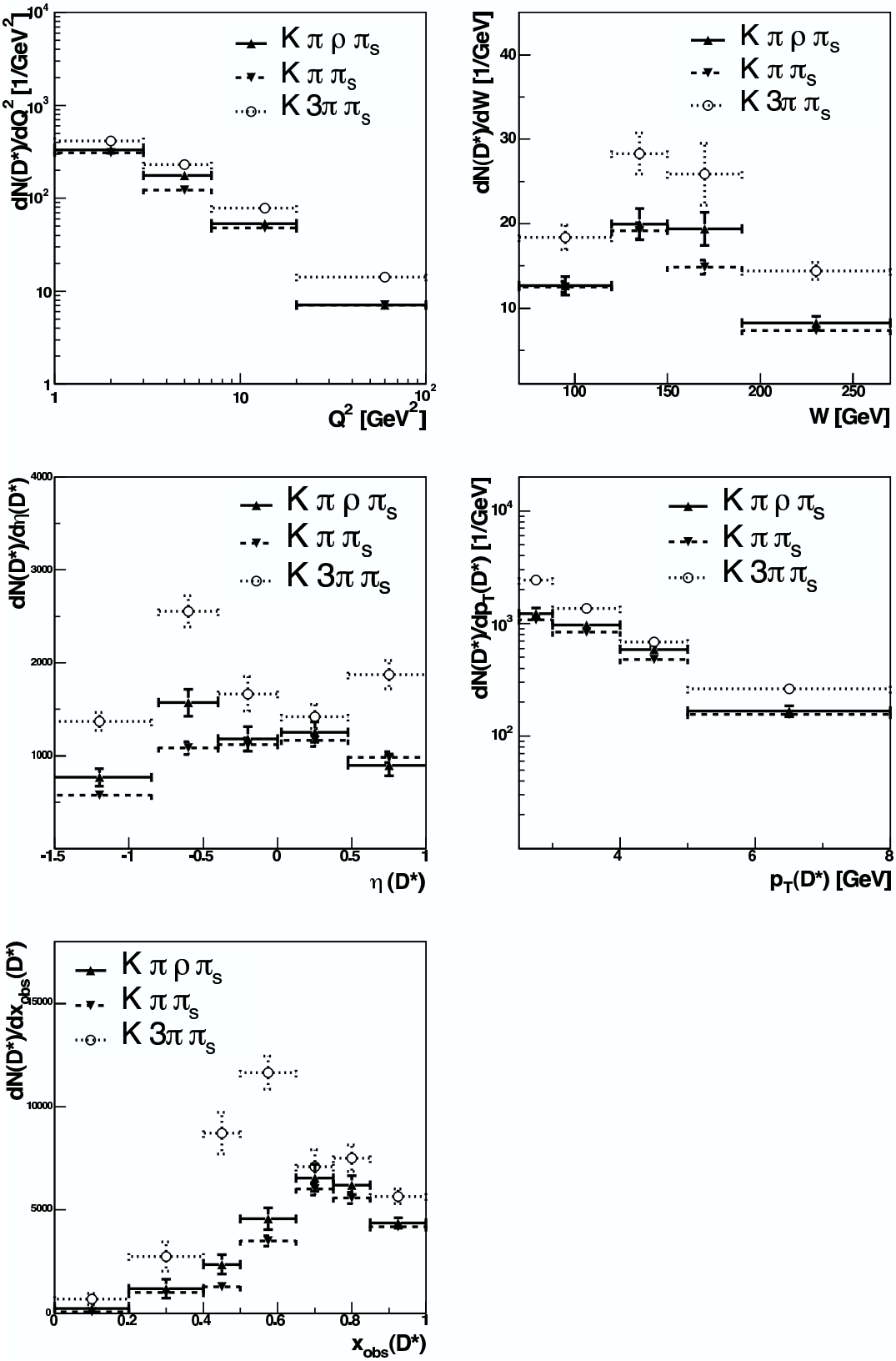

Figure 3.17: D^* meson yields in the data for the final states $K\pi\rho\pi_s$, $K\pi\pi_s$ and $K\pi\pi\pi\pi_s$ $(= K3\pi\pi_s)$.

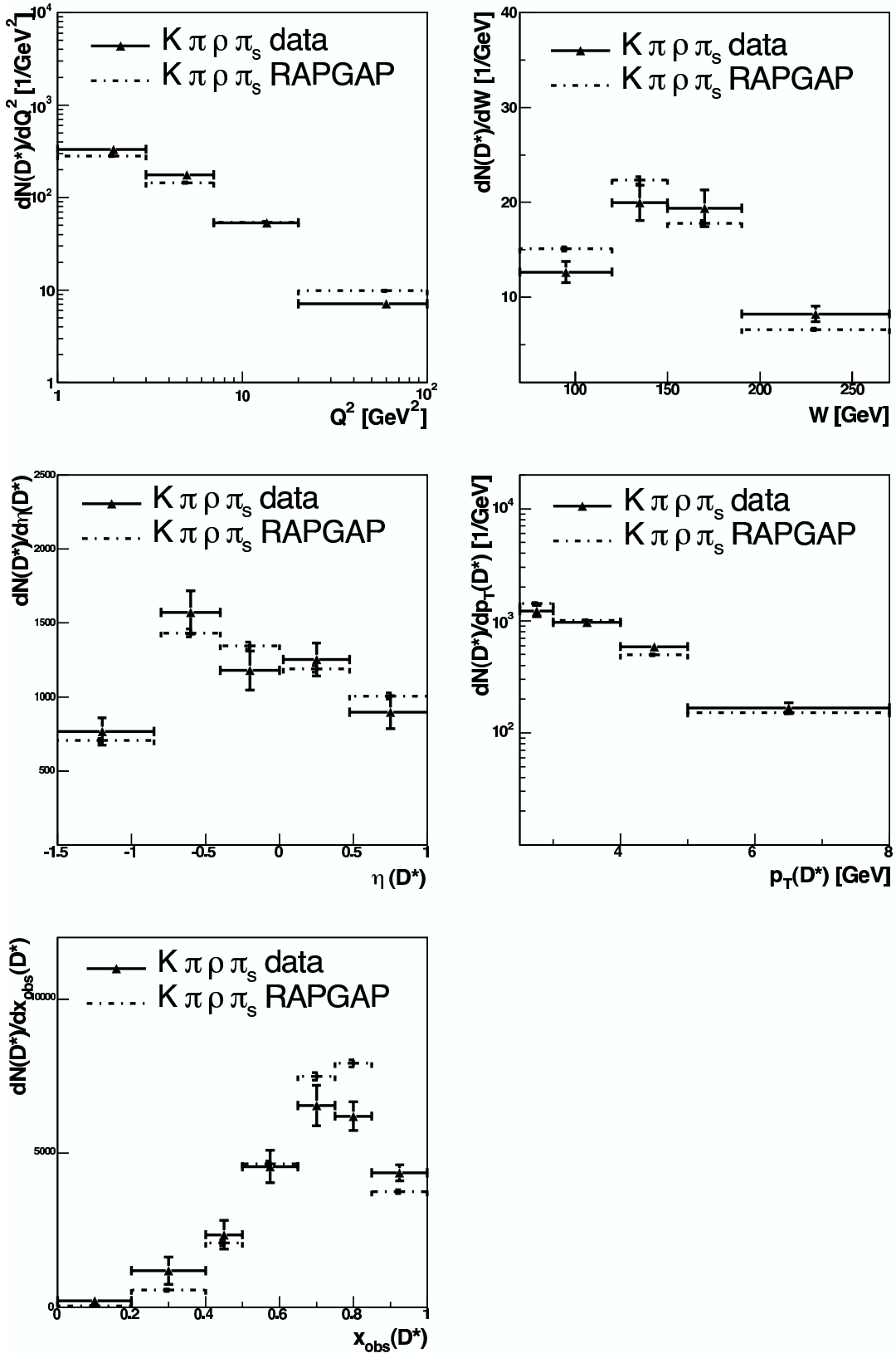

Figure 3.18: Differential yields for D^* mesons reconstructed in the decay channel (3.15), compared to a RAPGAP Monte Carlo simulation. The simulation is normalized according to the number of D^* mesons.

3.3.2 Detector acceptance

The H1 detector has almost full angular coverage. However, in this analysis, its geometric acceptance is limited to the region covered by the subdetectors used. These limitations together with selections on kinematic variables define the *visible range*, namely the conditions on the D^*'s pseudorapidity, transverse momentum and fragmentation variable.

The acceptance is determined from RAPGAP Monte Carlo simulations. The number of reconstructed D^* mesons $N_{rec}(D^*)$ is compared to the number of generated D^* mesons $N_{gen}(D^*)$; the total acceptance $\epsilon = N_{rec}(D^*)/N_{gen}(D^*)$ is a product of the geometric acceptance, trigger efficiency and reconstruction efficiency.

This analysis is limited to the DIS kinematic regime, defined by the requirements $1\ \text{GeV}^2 < Q^2 < 100\ \text{GeV}^2$ and $0.05 < y < 0.7$. The upper limit on Q^2 is due to the geometric acceptance of the backward calorimeter (SpaCal). Photoproduction events are excluded by selecting $Q^2 > 1\ \text{GeV}^2$. The y limits exclude regions with high photoproduction background, large radiative corrections and poor y resolution. The cuts on the generated kinematic variables used for the acceptance determination are summarized in table 3.10.

kinematic variable	selection
D^* pseudorapidity	$-1.5 < \eta(D^*) < 1.0$
D^* transverse momentum	$p_T(D^*) > 2.5$ GeV
photon virtuality	$1\ \text{GeV}^2 < Q^2 < 100\ \text{GeV}^2$
inelasticity	$0.05 < y < 0.7$
D^* fragmentation variable	$x_{obs}(D^*) > 0.5$

Table 3.10: Selection cuts on kinematic variables, used for the acceptance determination.

The overall acceptance is 39% for $D^* \to K\pi\rho\pi_s$ and 51% for $D^* \to K\pi\pi_s$ [43] if the same selection criteria are applied. The acceptance behaviour for DIS event kinematics and D^* kinematics is shown in figure 3.19. Acceptances are shown in bins of photon virtuality Q^2, invariant mass of the hadronic system W, pseudorapidity $\eta(D^*)$, transverse momentum $p_T(D^*)$ and fragmentation variable $x_{obs}(D^*)$.

The shapes of the acceptances in Q^2, W, $\eta(D^*)$ and $p_T(D^*)$ are similar for both decay channels, regardless of whether the D^* is selected by fragmentation variable in the $K\pi\rho$ channel (3.15) or not. This is not the case for the acceptance in $x_{obs}(D^*)$. Obviously, $x_{obs}(D^*)$-ordering leads to a smaller

acceptance at low $x_{obs}(D^*)$, since a higher fragmentation variable for the accepted D^* candidates is required.

An asymmetric forward-backward behavior of D^* meson yields (see left middle panel of figures 3.17 and 3.18) is observed, while no such asymmetry is observed for the acceptance. The simulated D^*'s pseudorapidity on hadron level (i.e. on generator level) is shown in figure 3.20 for different selection cuts on the D^* production elasticity and fragmentation variable. In figure 3.21, the D^* production elasticity is shown versus the D^* pseudorapidity (left panel) and the D^* fragmentation is shown versus the D^* pseudorapidity (right panel). Both figures illustrate that a selection cut on the production elasticity and the fragmentation variable only affects the forward region (i.e. the region of positive η): The D^* yield is reduced due to the combination of selection cuts on fragmentation variable and production elasticity in the forward region. This type of selection suppresses D^* candidates in the forward region because these are less likely to be produced with a hard fragmentation spectrum. It would thus be appropriate to use correlated acceptance corrections. Due to lack of time, such a correction has not been performed.

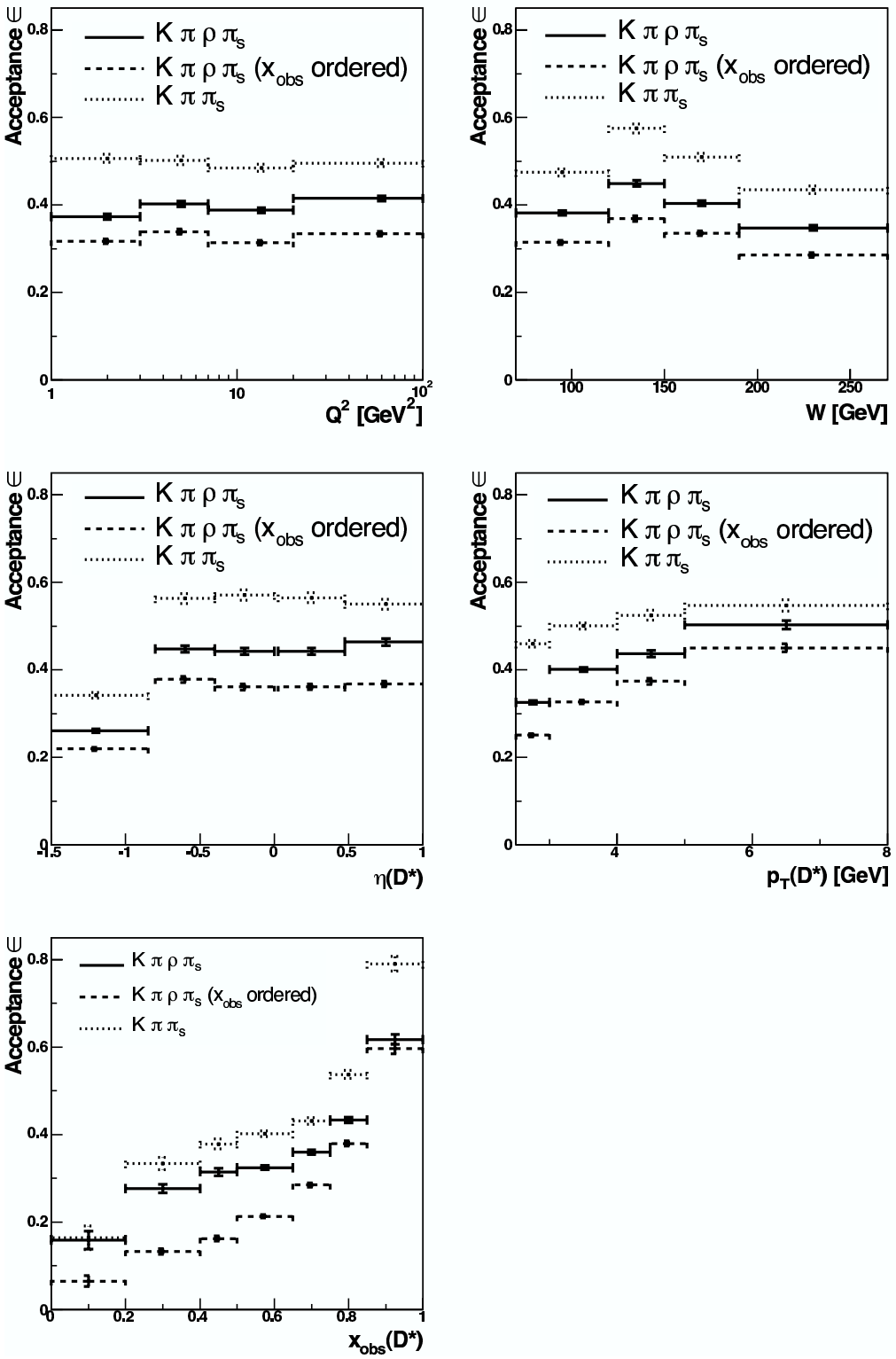

Figure 3.19: Comparison of acceptances for D^* reconstruction in different decay channels. The dotted line shows the behaviour for the $K\pi\pi_s$ final state. The dashed line represents D^* candidates with $x_{obs}(D^*)$-ordering (as described in section 3.2.3). The solid line shows acceptances for all D^* candidates without $x_{obs}(D^*)$-ordering.

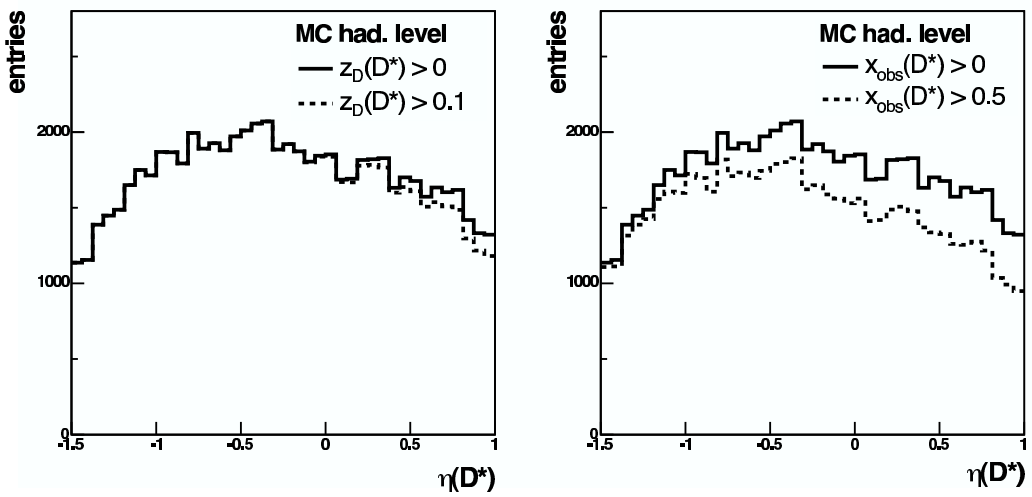

Figure 3.20: D^* pseudorapidity on hadron level for a cut on the production elasticity and on the fragmentation variable. The dashed line in the right panel shows the η behavior for the visible range.

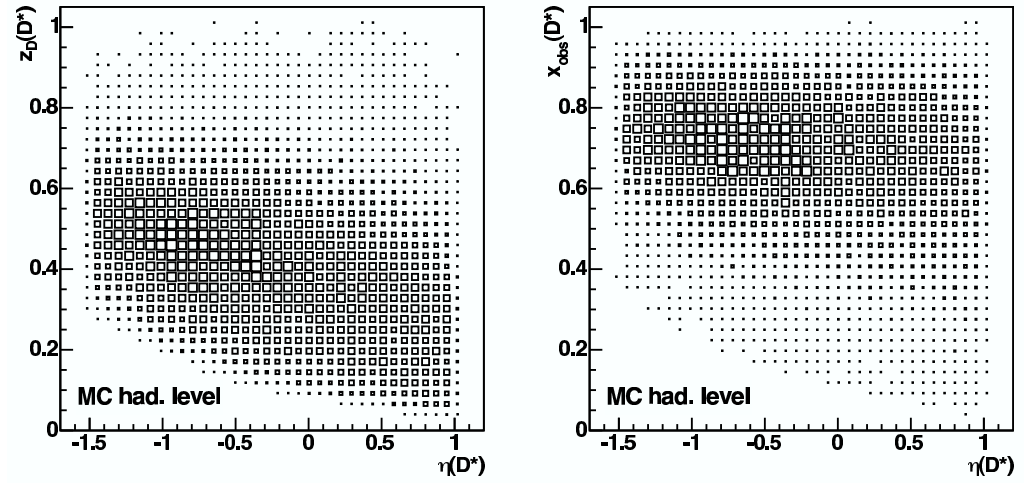

Figure 3.21: D^* production elasticity $z_D(D^*)$ versus pseudorapidity $\eta(D^*)$ and D^* fragmentation variable $x_{obs}(D^*)$ versus $\eta(D^*)$ on hadron level.

3.3.3 Differential cross sections

The D^* production cross section $\sigma(ep \to e' D^{*\pm} X)$ is determined from

$$\sigma(ep \to e' D^{*\pm} X) = \frac{N_{D^*}}{\mathcal{B}(D^{*\pm} \to K^{\mp}\pi^{\pm}\pi^{\pm}\pi^{\mp}\pi_s^{\pm}) \cdot \mathcal{L} \cdot \epsilon \cdot (1 + \delta_{rad})} \tag{3.16}$$

where N_{D^*} is the number of reconstructed D^* mesons, $\mathcal{L}$ the integrated luminosity of the data sample, ϵ the detector acceptance and efficiency and δ_{rad} are radiative corrections. The radiative corrections are small [3] and neglected in the following. The total branching ratio is a product of the branching ratios for each decay step [2]:

$$\begin{aligned}
&\mathcal{B}(D^{*+} \to K^-\pi^+\pi^+\pi^-\pi_s^+) \\
&\quad = \mathcal{B}(D^{*+} \to D^0\pi_s^+) \cdot \mathcal{B}(D^0 \to K^-\pi^+\rho^0) \cdot \mathcal{B}(\rho^0 \to \pi^+\pi^-) \\
&\quad = (67.7 \pm 0.5)\% \cdot (6.2 \pm 0.4)\% \cdot 99.9\% = (4.2 \pm 0.4)\%
\end{aligned}$$

A quantitative determination of the systematic error contributions to the cross section $\sigma(D^{*+} \to K^-\pi^+\rho^0\pi_s^+)$ has not been performed. The contributions to $\sigma(D^{*+} \to K^-\pi^+\pi_s^+)$ have been estimated in [3]. The further quoted numbers are taken from that analysis. Experimental uncertainties are:

- TRIGGER EFFICIENCY: The $K\pi\rho$ and the $K\pi$ channel are both included in the analysis on trigger level 4. The statistical uncertainty of the measured trigger efficiency contributes to the systematic error of the D^* measurement.

- ENERGY MEASUREMENT OF THE SCATTERED ELECTRON: The contribution of a wrong measurement of the energy of the scattered electron to the systematic uncertainty can be estimated from a Monte Carlo simulation. A variation of the energy of the scattered electron yielded a systematic error of $\pm 2\%$ of $\sigma_{total}(D^* \to K\pi\pi_s)$ [3].

- POLAR ANGLE MEASUREMENT OF THE SCATTERED ELECTRON: The polar angle θ'_e of the scattered electron is determined in the Spaghetti Calorimeter (SpaCal) and the Backward Drift Chamber (BDC). The experimental uncertainty is ± 2 mrad. The systematic error of $\sigma_{tot}(D^{*\pm} \to K^{\mp}\pi^{\pm}\pi_s^{\pm})$ from a wrong measurement of θ'_e is $\pm 2.5\%$ [3].

- EFFICIENCY OF TRACK RECONSTRUCTION: A small transverse momentum of the slow pion leads to a poor quality of the π_s track. The contribution to the systematic error of the total and differential cross sections in $D^{*\pm} \to K^{\mp}\pi^{\pm}\pi_s^{\pm}$ has been determined to be 11% and is the dominant contribution to the systematic error [3].

- BRANCHING FRACTION OF THE ANALYSED DECAY CHANNEL: The measurement error of the branching ratio of $D^{*+} \to D^0\pi_s^+$, $D^0 \to K^-\pi^+\rho^0$, $\rho^0 \to \pi^+\pi^-$ is $0.5\% \bigoplus 0.4\% = 0.6\%$. An additional systematical error comes from an effectively too small branching ratio: Two-pion combinations from D^* candidates which decay via the channel $D^* \to K\pi\pi\pi\pi_s$ can fulfill the imposed ρ-selections by coincidence. The D^* mesons are reconstructed as $D^* \to K\pi\rho\pi_s$ candidates and the use of a branching fraction $\mathcal{B}(D^0 \to K^-\pi^+\rho^0)$ of $(6.2 \pm 0.4)\%$ yields too large cross sections. The quantitative contribution of such an effect to the systematic error still has to be determined.

- INTEGRATED LUMINOSITY: The experimental error of the integrated luminosity measured by H1 is $\pm 1.5\%$.

Theoretical uncertainties come from:

- CHARM QUARK MASS m_c: the charm quark mass used in simulations for this work has been set to $m_c = 1.4$ GeV.

- FRAGMENTATION MODEL: Monte Carlo simulations in this analysis have used the Peterson model to describe charm fragmentation. The parameter $\epsilon = 0.078$ has been used for the Peterson fragmentation function [14].

The data set used to determine D^* production cross sections was recorded in the years 1996 until 2000, corresponding to an integrated luminosity of 75 pb^{-1}. The detector acceptance ϵ has been determined in section 3.3.2.

Differential cross sections for D^* production in the decay channels (3.14) and (3.15) are shown in figures 3.22 to 3.27. D^* cross sections in the $K\pi\rho$ decay channel with $x_{obs}(D^*)$-ordering (dash-dotted line) are compared to those without $x_{obs}(D^*)$-ordering (solid line) and to those in the $K\pi$ decay channel (dotted line) in figures 3.22 to 3.24. In figure 3.22, event kinematics in Q^2 and W are shown, while in figure 3.23, the D^* meson's pseudorapidity $\eta(D^*)$ and transverse momentum $p_T(D^*)$ are displayed; the production cross section for the D^*'s fragmentation variable $x_{obs}(D^*)$ is shown in figure 3.24. The cross sections behave similar, regardless of $x_{obs}(D^*)$-ordering. D^* production in the backward region is preferred as can be seen from the asymmetric behaviour of $d\sigma/d\eta$.

In figures 3.25 to 3.27, differential production cross sections for D^* mesons from $K\pi\rho\pi_s$ decays in the data (solid line) are compared to D^* mesons from that channel simulated with the RAPGAP Monte Carlo simulation (dashed line). The data is well described by the simulation.

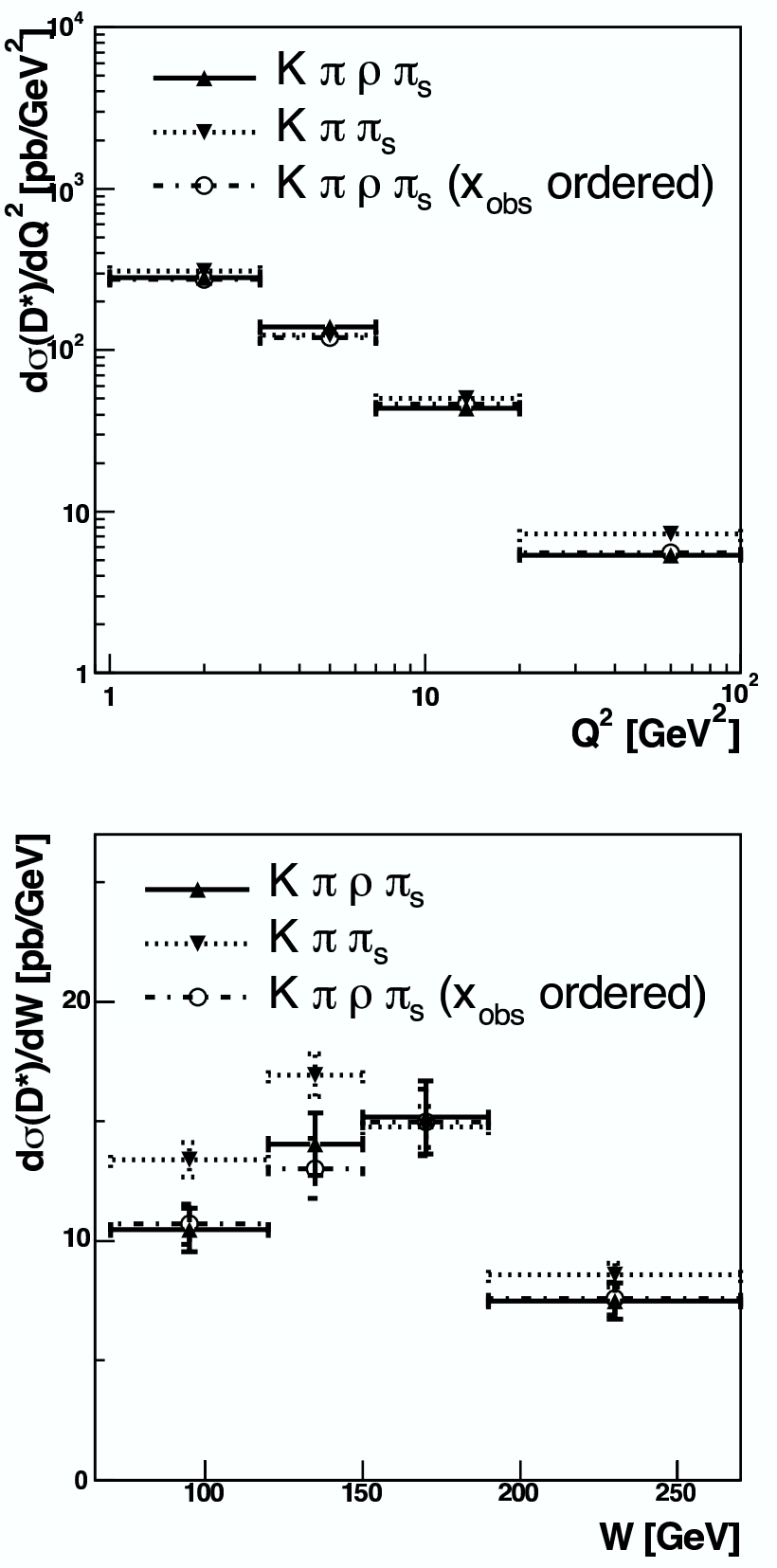

Figure 3.22: Differential cross sections for D^* mesons from $D^* \to K\pi\rho\pi_s$ with and without $x_{obs}(D^*)$-ordering.

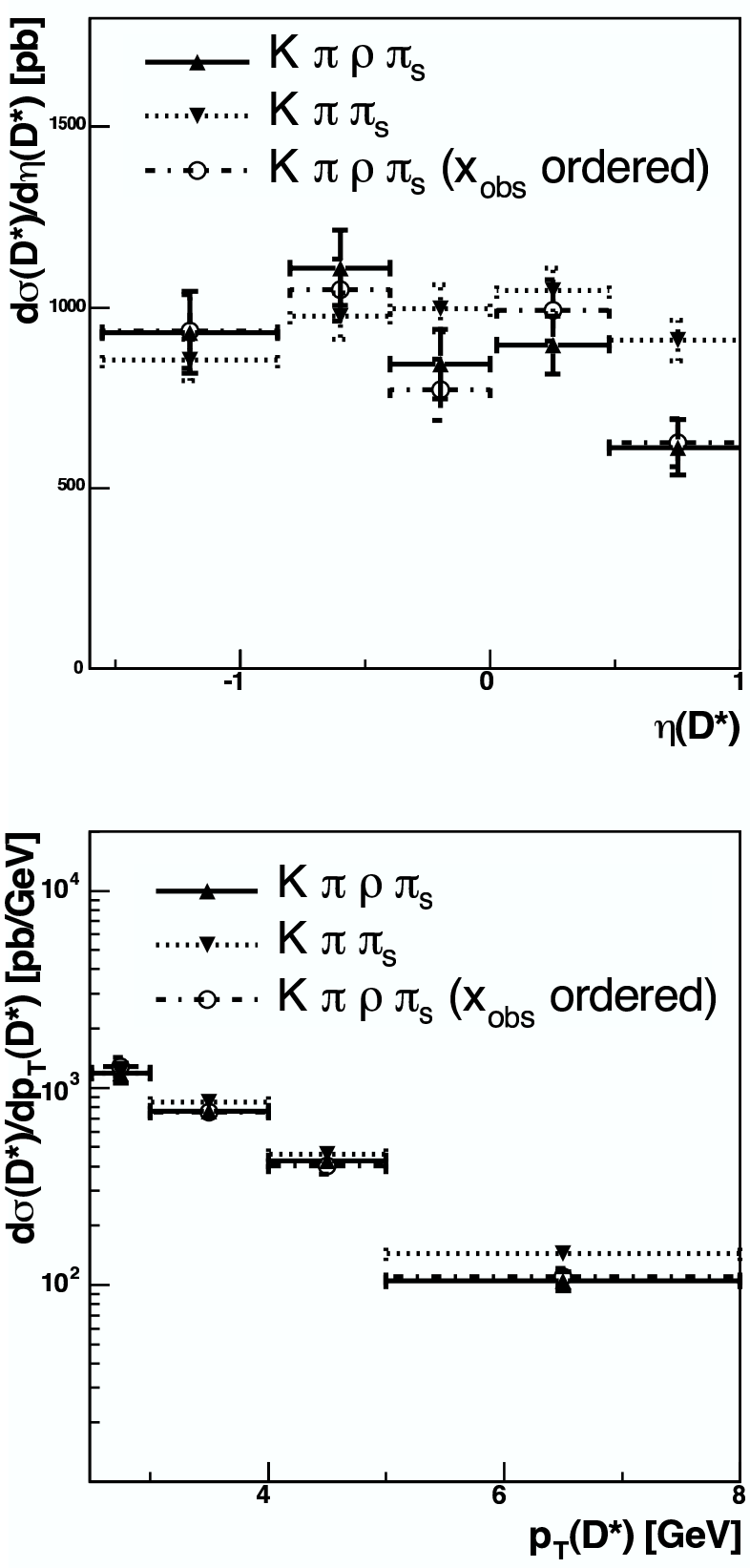

Figure 3.23: Differential cross sections for D^* mesons from $D^* \to K\pi\rho\pi_s$ with and without $x_{obs}(D^*)$-ordering.

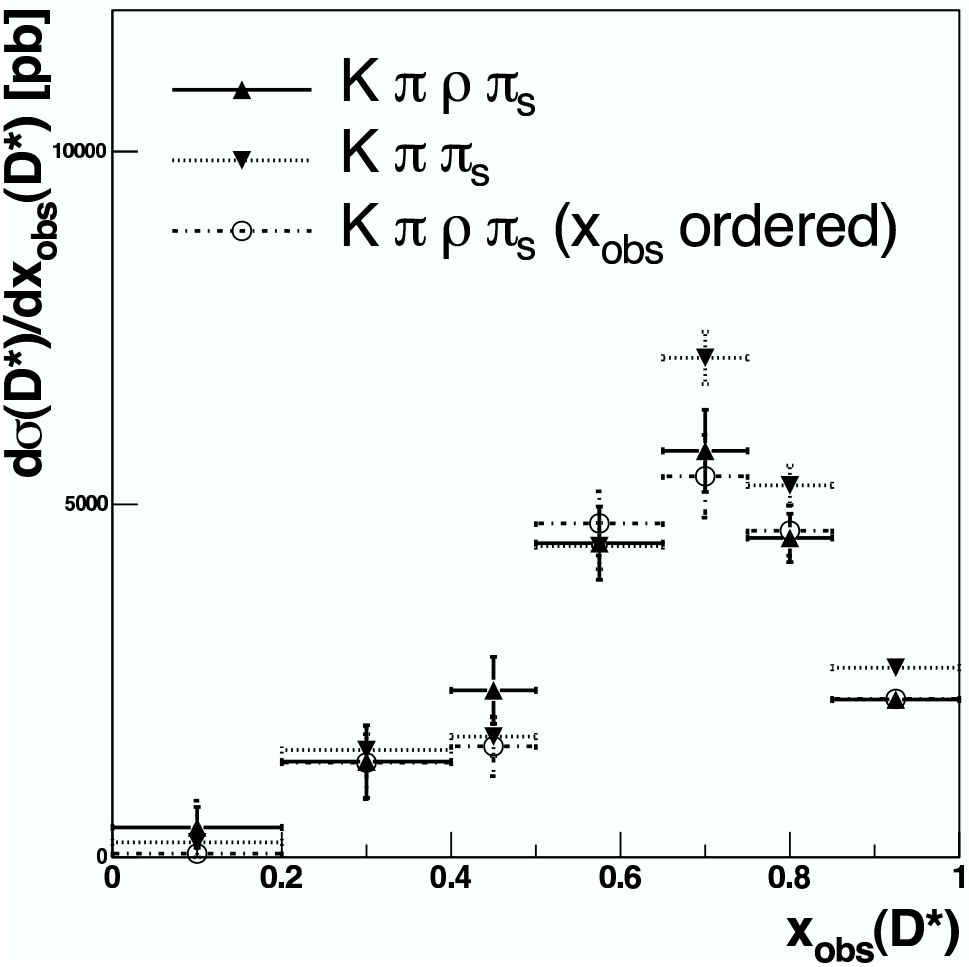

Figure 3.24: Differential cross sections for D^* mesons from $D^* \to K\pi\rho\pi_s$ with and without $x_{obs}(D^*)$-ordering.

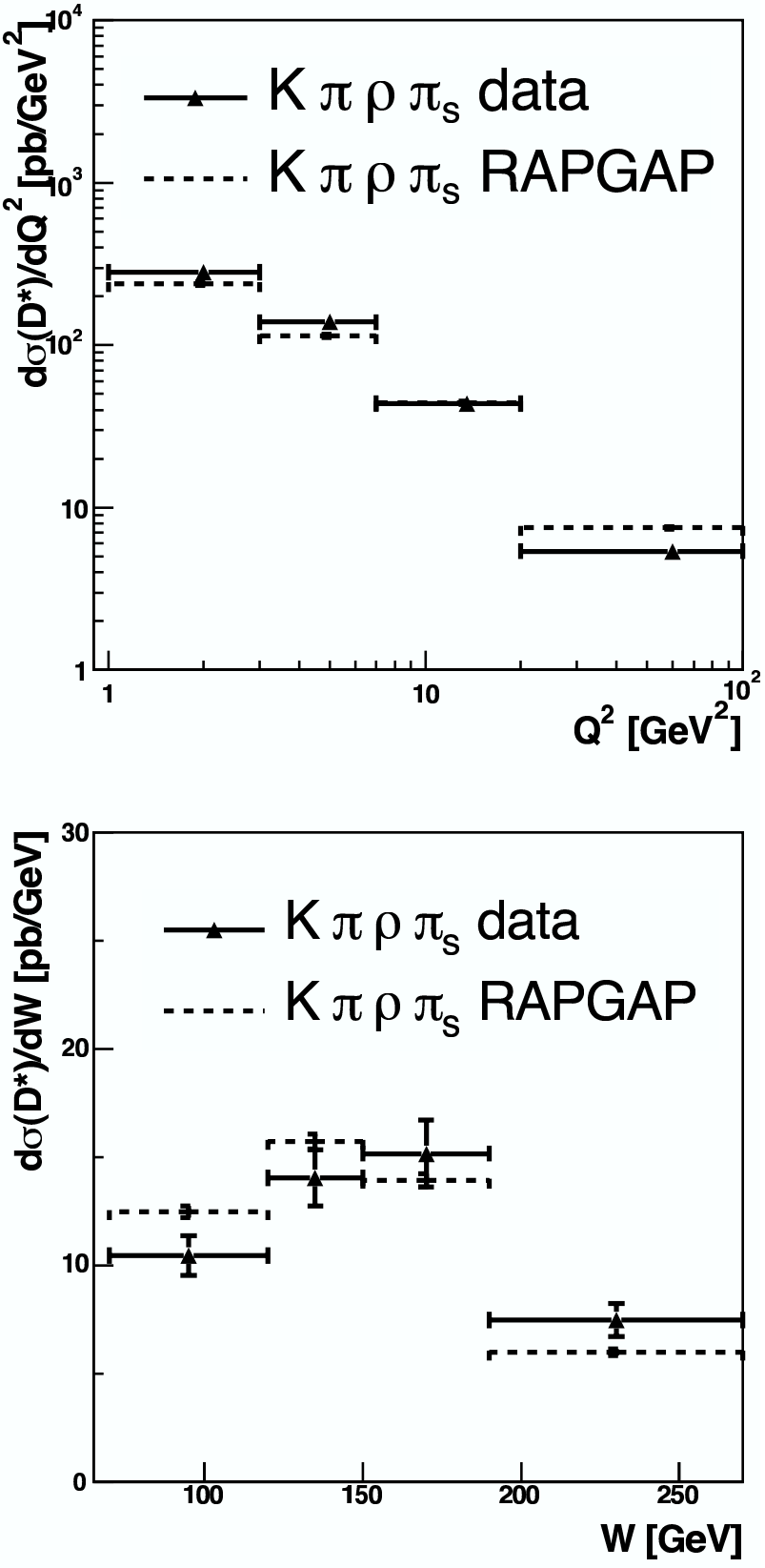

Figure 3.25: Differential cross sections for D^* mesons from $D^* \to K\pi\rho\pi_s$ in data and Monte Carlo simulation.

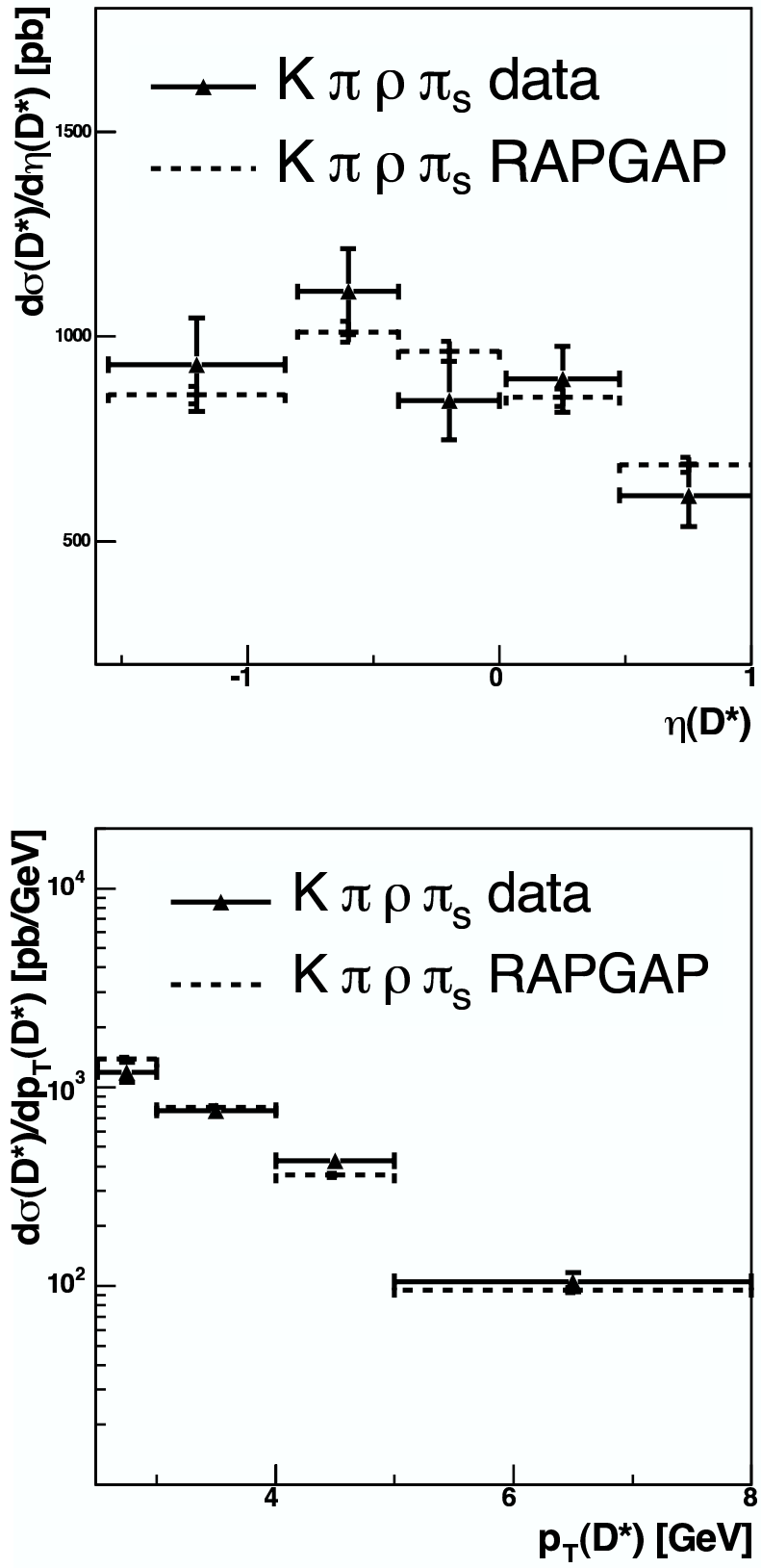

Figure 3.26: Differential cross sections for D^* mesons from $D^* \to K\pi\rho\pi_s$ in data and Monte Carlo simulation.

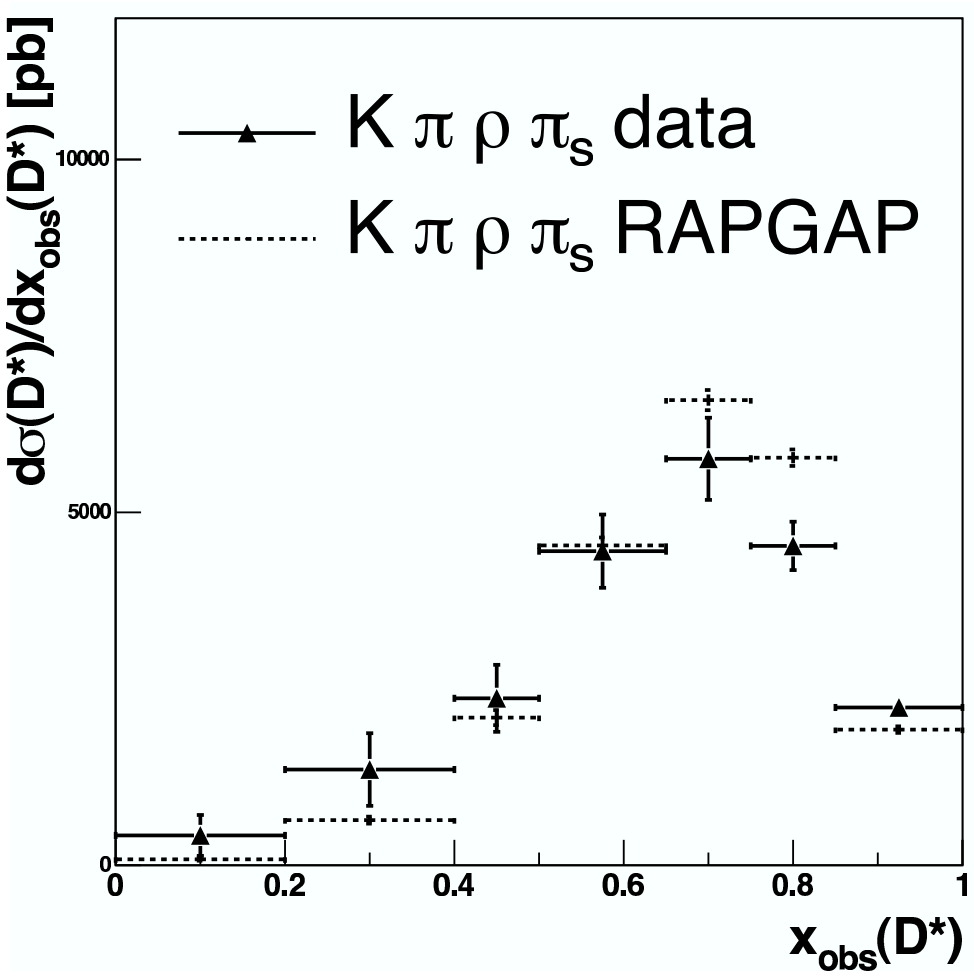

Figure 3.27: Differential cross sections for D^* mesons from $D^* \to K\pi\rho\pi_s$ in data and Monte Carlo simulation.

3.3.4 Discussion

The number of reconstructed D^* mesons in the decay channel $D^* \to K\pi\rho\pi_s$ is comparable to the number of reconstructed D^* mesons in the decay channel $D^* \to K\pi\pi_s$, as can be seen in figure 3.17. Hence, a gain of the same amount of D^* statistics has been achieved. Without the requirement on the intermediate ρ^0 state for the decay $D^* \to K\pi\pi\pi\pi_s$, the D^* statistics is even higher. However, this is only achieved with a significantly worse signal-to-background ratio.

The shapes of the acceptances in Q^2, W, $\eta(D^*)$ and $p_T(D^*)$ are similar for both decay channels, regardless of whether the D^* is selected by fragmentation variable in the $K\pi\rho$ decay channel or not. This is not expected for the acceptance in x_{obs}, as in the ordering case (i.e. for a D^* selection by maximum fragmentation variable $x_{obs}(D^*)$) high-x_{obs} candidates are preferred with respect to low-x_{obs} candidates. This can be seen in a different shape of the acceptance spectrum for the ordering case, compared to the other graphs (see the lower panel of figure 3.19). Without $x_{obs}(D^*)$ ordering, the acceptance shapes for both decay channels agree.

Differential cross sections have been determined for different event and D^* kinematic quantities in the decay channel $D^* \to K\pi\rho\pi_s$ with and without ordering in the charm fragmentation variable $x_{obs}(D^*)$ and in the decay channel $D^* \to K\pi\pi_s$. Results agree for both decay channels and both ordering methods. Differential cross sections from the $K\pi\rho\pi_s$ decay without $x_{obs}(D^*)$ ordering are well described by the simulation. The comparable yields in the decay channels $D^* \to K\pi\rho\pi_s$ and $D^* \to K\pi\pi_s$ hint on a large statistical gain for future D^* analyses when adding the $K\pi\rho$ decay reconstruction to the H1 analysis framework.

Systematic errors have not been studied in this analysis. Specific to the investigated decay channel is a systematic error from the branching ratio $\mathcal{B}(D^0 \to K^-\pi^+\rho^0)$ due to $D^* \to K\pi\pi\pi\pi_s$ candidates wrongly reconstructed in the decay channel $D^* \to K\pi\rho\pi_s$, $\rho \to \pi\pi$. Furthermore, a closer investigation of the correlation of the imposed selection cuts has to be performed: The $x_{obs} > 0.5$-selection suppresses candidates in the forward detector region and the acceptance still has to be corrected.

Chapter 4

Search for exotic baryons containing charm

A narrow state in $D^{*-}p$ and $D^{*+}\bar{p}$ invariant mass combinations (see figure 1.5) has been observed in deep-inelastic electron-proton collisions with the H1 experiment [28]. The resonance has a mass of 3099 MeV and a measured Gaussian width of 12 MeV compatible with the experimental resolution.

The observed state is interpreted as an anti-charmed baryon with a quark content $uudd\bar{c}$ (and its charge conjugate) and is thus a candidate for a charmed pentaquark state θ_c. D^* candidates have been reconstructed in the decay channel $D^{*+} \to D^0\pi_s^+$, $D^0 \to K^-\pi^+$.

The attempt is made to increase the statistics for this particular search by including the previously described D^* decay channel[1]

$$D^{*+} \to D^0\pi_s^+ \ , \ D^0 \to K^-\pi^+\rho^0 \ , \ \rho^0 \to \pi^+\pi^- \tag{4.1}$$

in the search for charmed pentaquarks with the H1 experiment. D^* candidates are combined with proton candidates and the resulting invariant mass spectrum is investigated. The selection criteria on D^* mesons, protons and D^*p combinations are given in section 4.1. The detector acceptance for charmed pentaquark candidates is determined in section 4.2. In section 4.3, the resulting D^*p invariant mass spectra are shown and discussed. Upper limits on the θ_c production cross section are determined in section 4.4. In the final section 4.5, the results of the pentaquark search with D^* mesons reconstructed in the decay channel (4.1) are discussed.

[1] Charge conjugates are implicitly included.

4.1 Selection criteria

The selection criteria on D^* meson, proton and D^*p combination are described in the following.

D^* selection

Unless stated in table 4.1, the D^* selection cuts are those described in the previous chapter. In figure 4.1, the fragmentation properties of D^* candidates from charmed pentaquark candidates are shown, measured in the D^* decay channel $D^* \to K\pi\pi_s$ [44]. The charm quark's energy is divided between proton and D^* meson. Hence, the D^* meson has a softer fragmentation variable if it comes from a charmed pentaquark decay than if it is directly produced in boson-gluon fusion. Therefore, the selection cut on the D^* fragmentation variable $x_{obs}(D^*) > 0.5$ is dropped when searching for a charmed pentaquark.

Selections from last chapter	Selections for pentaquark search
$R_{length}(\pi) \geq 25$ cm	$R_{length}(\pi) \geq 15$ cm
$R_{length}(K) \geq 25$ cm	$R_{length}(K) \geq 15$ cm
$R_{length}(\pi_s) \geq 0$ cm	$R_{length}(\pi_s) \geq 10$ cm
$p_T(K) > 0.25$ GeV	$p_T(K) > 0.15$ GeV
$L_K > 5\%$	$L_K > 5\%$ for $p(K) < 800$ MeV
	$L_K > 1\%$ for $p(K) \geq 800$ MeV
$x_{obs}(D^*) > 0.5$	no requirement on $x_{obs}(D^*)$

Table 4.1: Comparison of selection cuts used in the previous chapter and selection cuts used to search for charmed pentaquark candidates.

Proton identification

The requirements to select the proton candidate are taken from [28]. The proton's distance of closest approach (d_0) to the primary vertex in the $r\phi$-plane has to be less than 2.5 cm. The pion background is suppressed by a requirement on the normalized likelihood from ionization loss.

A large number of hits enables a better proton-pion or proton-kaon separation (see figure 2.6). However, a proton identification based on the normalized likelihood from ionization loss is difficult for large momenta (see figure 2.5). The selection cuts are accordingly loosened for a proton momentum above 2 GeV: The number of hits used for dE/dx-measurement $N_{\text{CJC hits}}(p)$ has to be larger than 11 and the normalized dE/dx-likelihood to be a proton has to be above 10%. For lower proton momenta $N_{\text{CJC hits}}(p)$ has to

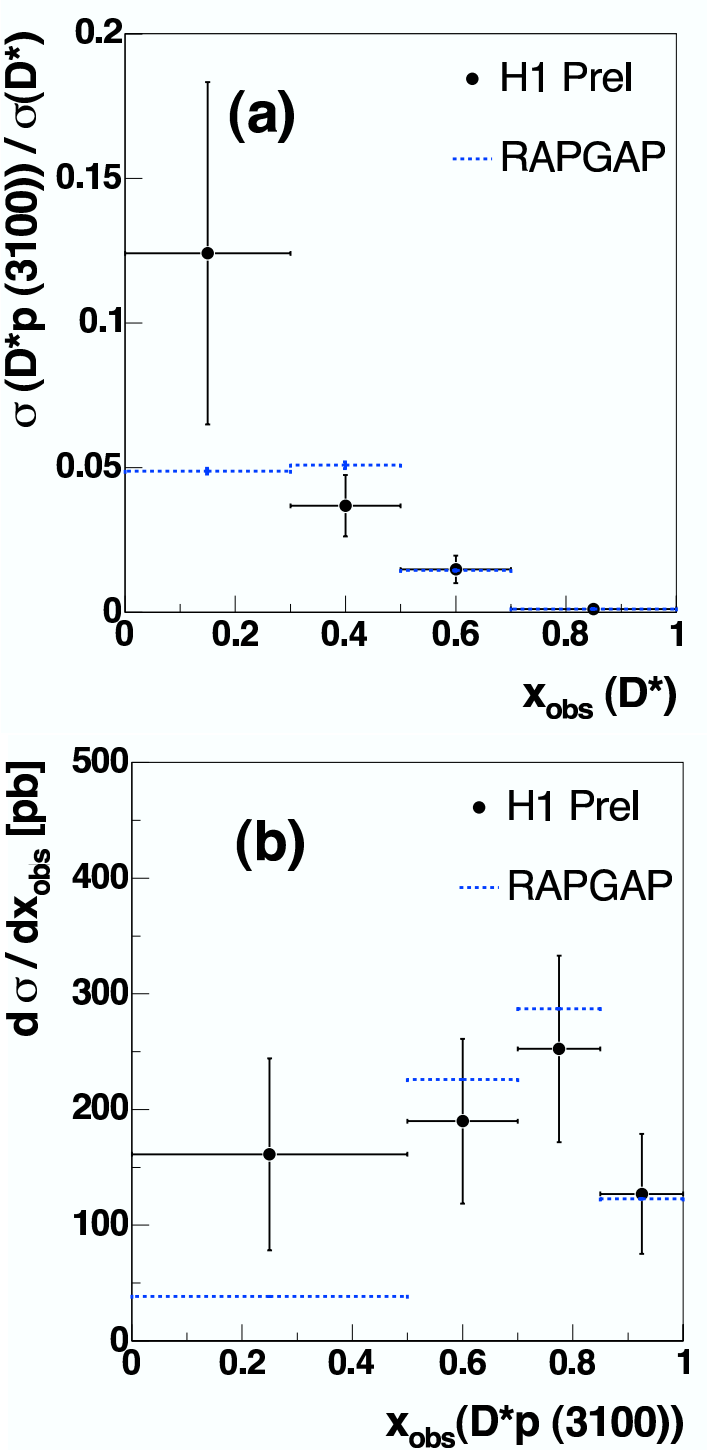

Figure 4.1: Fragmentation characteristics for D^*p candidates in the channel $D^*p \to K\pi\pi_s p$ [44]: (a) Acceptance corrected ratio $\sigma_{vis}(D^*p(3100))/\sigma_{vis}(D^*)$ in bins of the fragmentation variable $x_{obs}(D^*)$ in data and simulation. (b) Differential cross section $d\sigma_{vis}(D^*p(3100))/dx_{obs}(D^*p)$ in data and simulation. Only statistical errors are shown.

be at least 21, while proton candidates with a normalized dE/dx-likelihood below 30% are rejected. The different cuts for different momentum ranges reflect the changing separability of proton, pion and kaon tracks for different momenta (see figure 2.6).

Figure 4.2 suggests a better signal-to-background ratio for increasing proton momenta and no proton dE/dx-requirements [28]. Hence, the invariant mass spectrum of D^*p combinations for $D^* \to K\pi\rho\pi_s$ is also investigated for a selection cut on the proton momentum while dropping the requirements on the proton dE/dx.

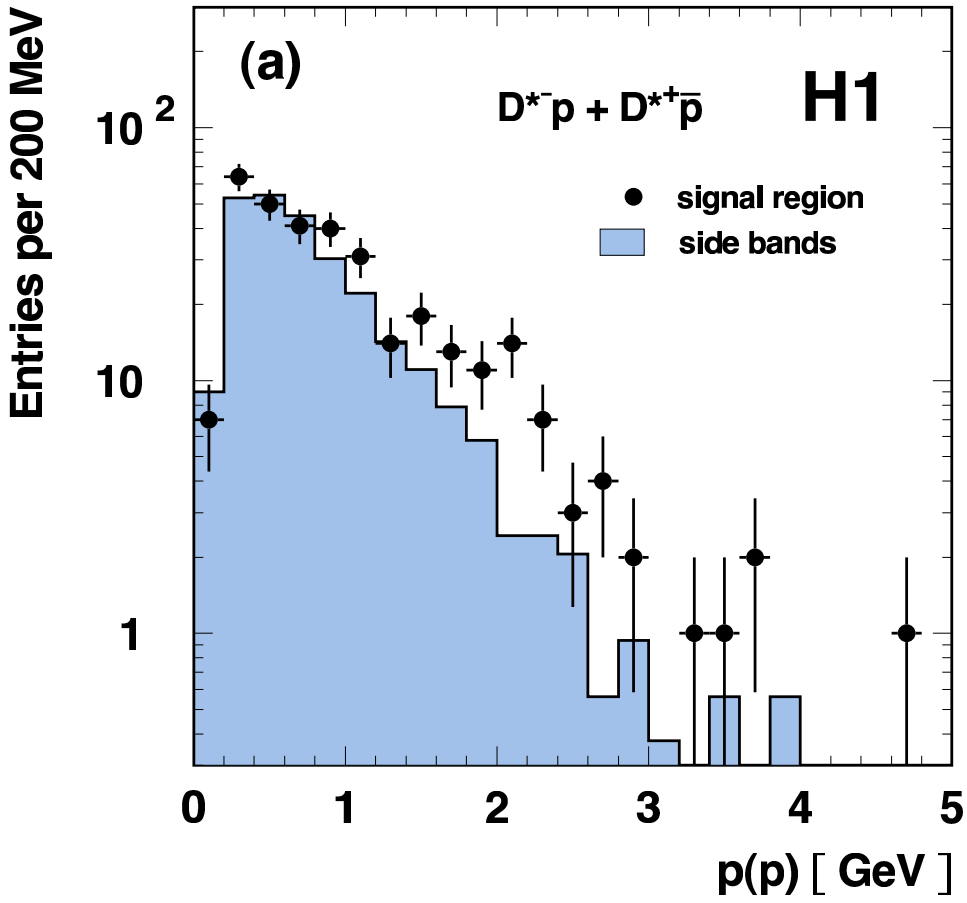

Figure 4.2: Momentum spectra of protons from D^*p combinations in the channel $D^*p \to K\pi\pi_s p$ [28]. No requirement on the proton's ionization loss is imposed. The proton momenta are compared for proton candidates from the signal region ($3085 < M(D^*p) < 3115$ MeV) and from side bands ($2990 < M(D^*p) < 3070$ MeV and $3130 < M(D^*p) < 3210$ MeV).

D^*p selection

The D^*p kinematics have to fulfill the same selection cuts as the D^* meson, namely $p_T(D^*p) > 2.5$ GeV and $-1.5 < \eta(D^*p) < 1$.

The fragmentation variable for the D^*p combination, $x_{obs}(D^*p)$, can be approximated by

$$x_{obs}(D^*p) \approx z_D(D^*p) \cdot \frac{x_{obs}(D^*)}{z_D(D^*)} \quad , \tag{4.2}$$

where $z_D(D^*p)$, $z_D(D^*)$ and $x_{obs}(D^*)$ are production elasticity and fragmentation variable of D^*p combination and D^* candidate, respectively. In figure 4.3, this variable is shown versus the proton momentum $p(p)$, simulated with the RAPGAP Monte Carlo program in the channel $D^*p \to K\pi\rho p$ (this simulation of charmed pentaquarks is described in section 4.2). An additional selection cut on this variable has been investigated [44]:

$$x_{obs}(D^*p) \approx z_D(D^*p) \cdot \frac{x_{obs}(D^*)}{z_D(D^*)} > \min(0.5, 0.5\,p(p)/\text{GeV}) \ . \tag{4.3}$$

This selection cut excludes the region where non-charmed background dominates over the D^* signal. The boundary of the excluded region is also indicated in figure 4.3. All selection cuts are summarized in table 4.2.

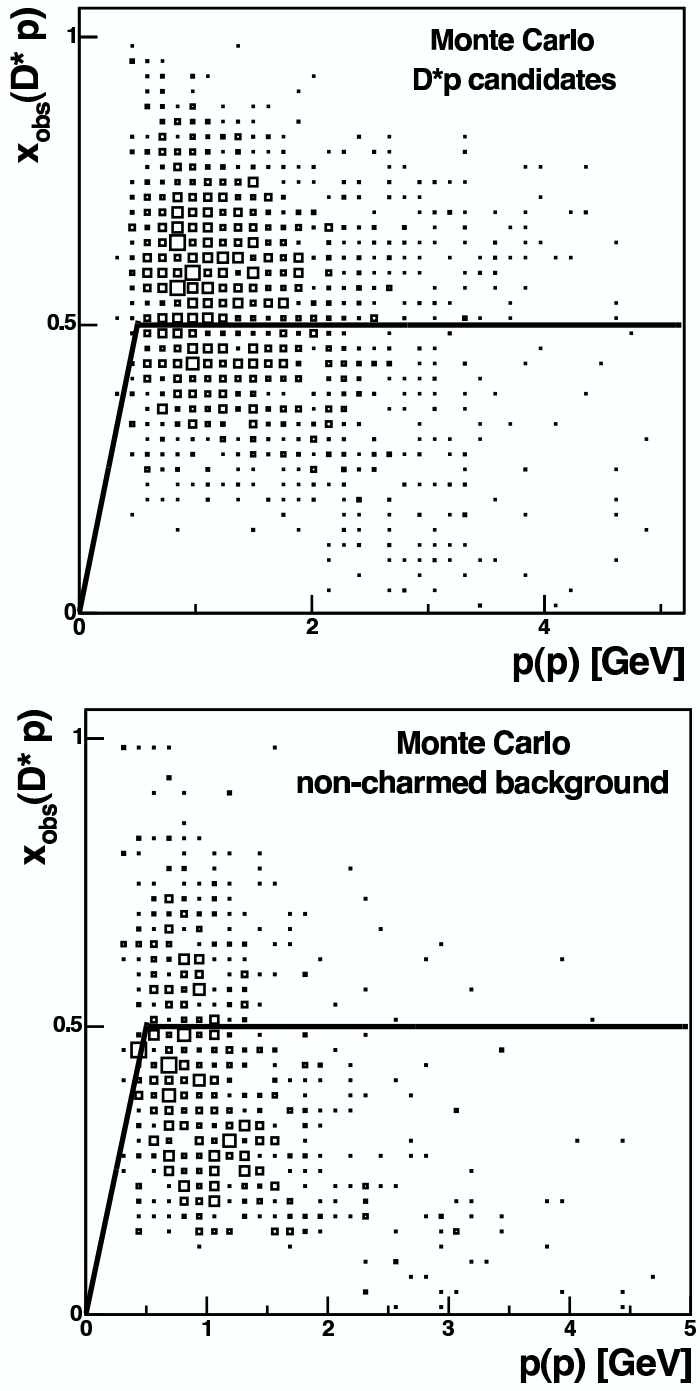

Figure 4.3: Comparison of the proton momentum to $x_{obs}(D^*p) \approx z_D(D^*p) \cdot \frac{x_{obs}(D^*)}{z_D(D^*)}$ for simulated D^*p candidates (upper panel) and non-charmed background (lower panel). The D^*p generation in the channel $D^*p \to K\pi\rho p$ with the RAPGAP Monte Carlo is described in section 4.2. Non-charmed background is described by a DJANGO Monte Carlo simulation. The black line indicates the region where $x_{obs}(D^*p) = \min(0.5, 0.5\,p(p)/\mathrm{GeV})$.

$\theta_c \to D^*p \to K\pi\rho\pi_s p$	
D^0	$p_T(\pi) > 0.2$ GeV $p_T(K) > 0.15$ GeV $\chi^2/\mathrm{ndf}(\pi), \chi^2/\mathrm{ndf}(K) \leq 10$ $R_{length}(\pi), R_{length}(K) \geq 15$ cm $R_{start}(\pi), R_{st0art}(K) \leq 25$ cm $L_K > 5\%$ for $p(K) < 800$ MeV $L_K > 1\%$ for $p(K) \geq 800$ MeV $L_\pi, L_{\pi_1}, L_{\pi_2} > 1\%$ for $p(\pi), p(\pi_1), p(\pi_2) < 800$ MeV $\lvert M(D^0) - M(K\pi\rho)\rvert < 60$ MeV
D^*	$p_T(D^*) > 2.5$ GeV $z_D(D^*) > 0.1$ $R_{length}(\pi_s) \geq 10$ cm $L_{\pi_s} > 5\%$ $\lvert M(D^*) - M(K\pi\rho\pi_s)\rvert < 2.5$ MeV
p	$\lvert d_0\rvert < 2.5$ cm $L_p > 10\%$ for $p(p) > 2$ GeV and $N_{\mathrm{CJC\ hits}}(p) > 11$ $L_p > 30\%$ for $N_{\mathrm{CJC\ hits}}(p) > 20$
D^*p	$p_T(D^*p) > 2.5$ GeV $-1.5 < \eta(D^*p) < 1$

$\theta_c \to D^*p \to K\pi\pi\pi\pi_s p$	
D^0	$p_T(K) > 0.15$ GeV $\chi^2/\mathrm{ndf}(K) \leq 10$ $R_{length}(K) \geq 15$ cm $R_{start}(K) \leq 25$ cm $L_K > 5\%$ for $p(K) < 800$ MeV $L_K > 1\%$ for $p(K) \geq 800$ MeV $L_{\pi_1}, L_{\pi_2}, L_{\pi_3} > 1\%$ for $p(\pi_1), p(\pi_2), p(\pi_3) < 800$ MeV $\lvert M(D^0) - M(K\pi\rho)\rvert < 60$ MeV
D^*	$p_T(D^*) > 2.5$ GeV $z_D(D^*) > 0.1$ $R_{length}(\pi_s) \geq 10$ cm $L_{\pi_s} > 5\%$ $\lvert M(D^*) - M(K\pi\rho\pi_s)\rvert < 2.5$ MeV
p	$\lvert d_0\rvert < 2.5$ cm $L_p > 10\%$ for $p(p) > 2$ GeV and $N_{\mathrm{CJC\ hits}}(p) > 11$ $L_p > 30\%$ for $N_{\mathrm{CJC\ hits}}(p) > 20$
D^*p	$p_T(D^*p) > 2.5$ GeV $-1.5 < \eta(D^*p) < 1$

Table 4.2: Summary of the selection cuts for the pentaquark search.

4.2 Reconstruction efficiency

The reconstruction efficiency is determined from simulating a charmed pentaquark θ_c with RAPGAP. The pentaquark state θ_c is assumed to originate from the fragmentation of charm quarks produced in boson-gluon fusion.

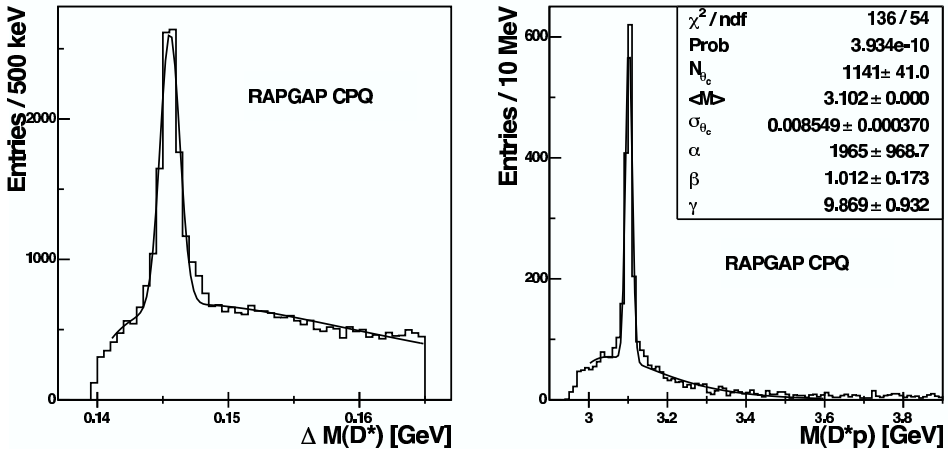

Figure 4.4: Simulated mass spectra for D^* mesons from charmed pentaquark candidates and the corresponding charmed pentaquark candidates.

The RAPGAP charmed pentaquark (CPQ) simulation describes θ_c states by modifying mass and decay modes of D_1^0, D_1^{*0} and D_2^{*0}: Masses are set to 3100 MeV, the artificial θ_c is required to decay into $D^{*-}p$ or $D^{*+}\bar{p}$. No spin is assigned to the particle, i.e. the resonance is assumed to decay isotropically. The resulting D^* mass difference spectrum (left panel) and D^*p mass spectrum for pentaquark candidates reconstructed in the decay channel

$$\theta_c^0 \to D^{*+}\bar{p}\ ,\ D^{*+} \to D^0\pi_s^+\ ,\ D^0 \to K^-\pi^+\rho^0\ ,\ \rho^0 \to \pi^+\pi^- \tag{4.4}$$

is shown in figure 4.4. The θ_c width is determined from a Gaussian fit in the range $3000 < M(D^*p) < 3600$ MeV to be (8.5 ± 0.4) MeV. The functional form of the fit function is given by

$$f(M) = \underbrace{\alpha\,(M - m_{D^*} - m_p)^{\beta} \exp\left(\gamma \cdot (M - m_{D^*} - m_p)\right))}_{\text{background term}} \tag{4.5}$$

$$+ \underbrace{N_{\theta_c} \frac{dM}{\sqrt{2\pi}\sigma_{\theta_c}} \exp\left(-\frac{(M - \langle M\rangle)^2}{2\sigma_{\theta_c}^2}\right)}_{\text{signal term}}\ , \tag{4.6}$$

where N_{θ_c} is the number of θ_c states and σ_{θ_c}, $\langle M \rangle$ are signal width and mean value, respectively. The bin width of the $M(D^*p)$ histogram used for the fit is dM, while α, β and γ are fit parameters for the background description. The free parameters of the total fit are N_{θ_c}, σ_{θ_c}, $\langle M \rangle$ and the background parameters α, β, γ, respectively. As can be seen in the right panel of figure 4.4, this fit does not describe the small excess around the θ_c signal coming from D^* candidates filled with several proton candidates. A quantitative determination of the contribution of these multiple fillings to the $M(D^*p)$ spectrum has not been performed.

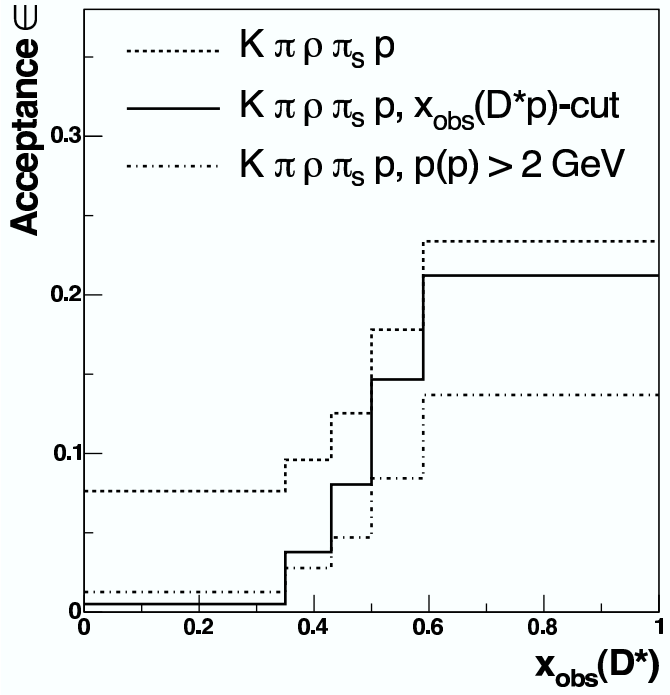

Figure 4.5: Acceptance for charmed pentaquarks θ_c in bins of the D^* fragmentation variable $x_{obs}(D^*)$ for D^*p combinations in the decay channel (4.4). The dashed line shows the D^*p acceptance from selection cuts listed in table 4.2. The solid line shows the θ_c acceptance with an additional cut on the D^*p fragmentation variable $x_{obs}(D^*p) \approx z_D(D^*p) \cdot \frac{x_{obs}(D^*)}{z_D(D^*)}$. Alternatively, selection cuts on the proton likelihood are removed, while the proton momentum is required to be above 2 GeV, shown by the dash-dotted line.

The θ_c acceptance in the decay channel (4.4) is shown in figure 4.5 in bins of the D^* fragmentation variable $x_{obs}(D^*)$ for different selection cuts. The overall acceptance is determined from dividing the number of reconstructed θ_c

candidates by the number of generated charmed pentaquarks. The following selection cuts are investigated:

- Only the selection cuts listed in table 4.2 are applied. All D^* candidates are combined with proton candidates and filled into the histograms with weight 1.
- An additional selection cut is imposed to suppress non-charmed background and contributions from D^* mesons not coming from a charmed pentaquark:

$$x_{obs}(D^*p) \approx z_D(D^*p) \cdot \frac{x_{obs}(D^*)}{z_D(D^*)} > \min(0.5, 0.5\,p(p)/\text{GeV}) \ ,$$

  as described in the previous section.
- The proton momentum is required to be above 2 GeV, while no more requirements on the proton's dE/dx-likelihood L_p and on the number of hits $N_{\text{CJC hits}}$ used for the dE/dx-measurement of the proton are imposed.

The overall θ_c acceptances for these selections are listed in table 4.3.

Selection	θ_c acceptance
$K\pi\rho\pi_s p$	24.5%
$K\pi\rho\pi_s p$, $x_{obs}(D^*p)$-cut	17.8%
$K\pi\rho\pi_s p$, $p(p) > 2$ GeV	10.9%

Table 4.3: Overall acceptances for θ_c candidates in the channel $\theta_c \to D^*p \to K\pi\rho\pi_s p$. Three different selections on the D^*p combination are compared (see text for description).

4.3 Investigation of the D^*p invariant mass spectrum

The invariant mass spectrum of $D^{*-}p$ and $D^{*+}\bar{p}$ combinations is investigated in the decay channels $D^* \to K\pi\pi_s$ (figure 4.7), $D^* \to K\pi\rho\pi_s \to K\pi\pi\pi\pi_s$ (figure 4.9) and $D^* \to K\pi\pi\pi\pi_s$ (figure 4.10). Mass difference spectra $M(D^*p)$ for D^*p candidates are shown, shifted by the nominal D^* mass:

$$M(D^*p) = M((D^*p)_{rec}) - M(D^*_{rec}) + M(D^*_{PDG}) \quad , \qquad (4.7)$$

where $(D^*p)_{rec}$ and D^*_{rec} are the reconstructed D^*p and D^* candidates, respectively.

D^*p candidates reconstructed in the $K\pi$ decay channel are shown for comparison. An exotic baryon containing charm is searched for in the decay channels $D^* \to K\pi\rho\pi_s \to K\pi\pi\pi\pi_s$ and $D^* \to K\pi\pi\pi\pi_s$. Three different selections, as described in the previous section, are imposed on the D^*p combinations. The D^* mass difference spectra are also shown for reference (figures 4.6 and 4.8); all candidates from these spectra with a reconstructed mass in the range $[145.4 - 2.5\ \text{MeV}, 145.4 + 2.5\ \text{MeV}]$ are combined with proton candidates.

Investigation of the D^*p resonance in the channel $D^*p \to K\pi\pi_s p$

To investigate the effect of the described additional cuts on the D^*p fragmentation variable $x_{obs}(D^*p)$ and on the proton momentum $p(p)$, the enhancement in the invariant mass of D^*p combinations in the channel $D^*p \to K\pi\pi_s p$ is reproduced. The thus obtained mass difference spectrum for D^* candidates is shown in figure 4.6. Invariant mass spectra of D^*p combinations

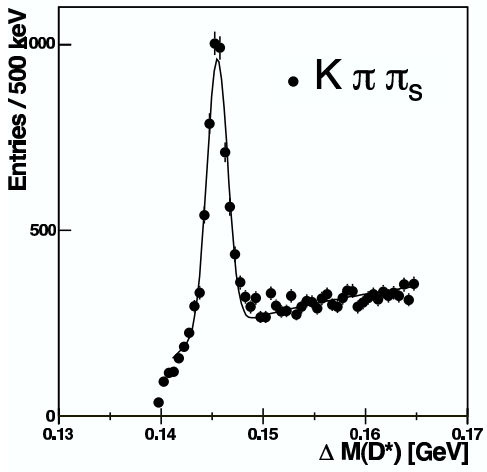

Figure 4.6: Mass difference spectrum for D^* candidates in the decay channel $D^* \to K\pi\pi_s$.

in the $K\pi\pi_s p$ channel are shown in figure 4.7. The selection cuts from [28] have been applied to obtain the mass spectrum in the top panel. As described earlier, two additional selection cuts are applied to obtain the middle and lower panels: A selection cut on the D^*p fragmentation variable $x_{obs}(D^*p) > \min(0.5, 0.5\,p(p)/\text{GeV})$ is applied for the candidates shown in

the middle panel. The proton momenta of the candidates in the lower panel have to fulfill $p(p) > 2$ GeV while dE/dx-requirements on the proton track have been omitted.

A narrow enhancement in the invariant mass spectrum of D^*p combinations at a mass of about 3.1 GeV is clearly visible for all selections. The $M(D^*p)$ spectrum in the upper panel differs slightly from the published mass difference spectrum (see figure 1.5). An event-by-event comparison to identify the reason still needs to be performed. Invariant mass spectra of D^*p combinations in the decay channel $D^*p \to K\pi\pi\pi\pi_s p$ are investigated in the next section.

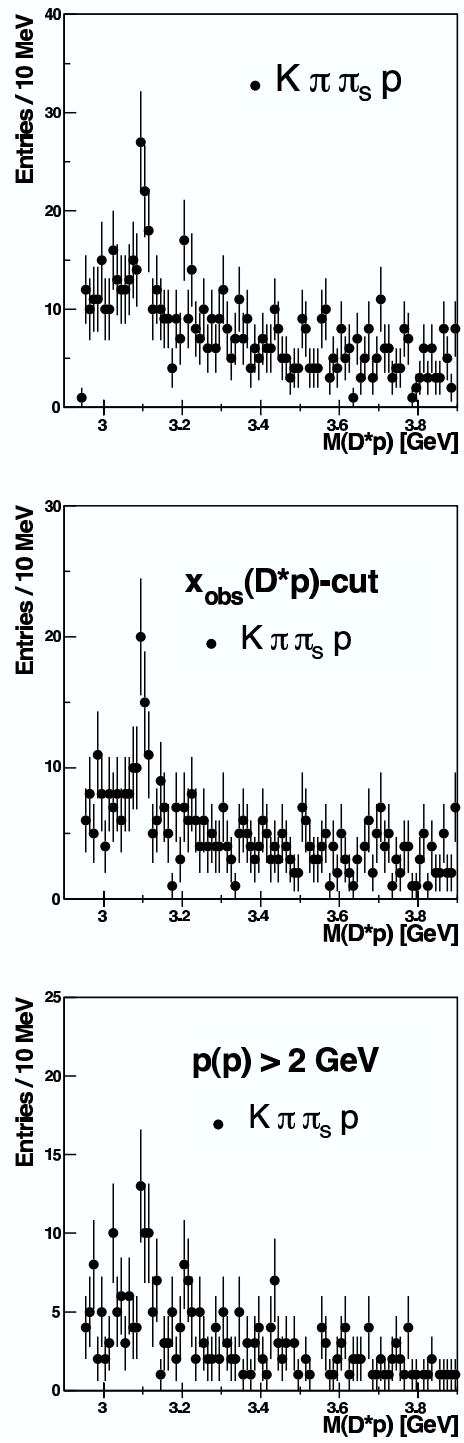

Figure 4.7: Invariant mass spectra of D^*p combinations in the decay channel $D^*p \to K\pi\pi_s p$. Additional selection cuts are imposed for the middle and lower panels.

Search for a charmed pentaquark in the channel $D^*p \to K\pi\pi\pi\pi_s p$

Combinations of D^* and proton candidates are investigated in the channels $D^*p \to K\pi\rho\pi_s p \to K\pi\pi\pi\pi_s p$ and $D^*p \to K\pi\pi\pi\pi_s p$. The selection cuts listed in table 4.2 have been applied. The corresponding D^* mass difference spectra are shown in figure 4.8. As only few pentaquark candidates are expected, it is desirable to improve the D^* signal-to-background ratio. However, measures like selecting D^* candidates with fragmentation variable $x_{obs}(D^*) > 0.5$ or requiring the maximal x_{obs} for a D^* candidate are not applied as $x_{obs}(D^*)$ is expected to be small for D^* mesons originating from a θ_c state (see figure 4.1).

In figures 4.9 and 4.10, mass spectra are shown for D^*p combinations in the channels $D^*p \to K\pi\rho\pi_s p \to K\pi\pi\pi\pi_s p$ and $D^*p \to K\pi\pi\pi\pi_s p$, respectively. Each row corresponds to a different set of selection cuts on the D^*p combinations: The selections listed in table 4.2 are imposed to the combinations used for the top panels. Additional selection cuts on D^*p fragmentation variable $x_{obs}(D^*p)$ and proton momentum $p(p)$ have been applied to the middle and lower panels, respectively. Background contributions are modeled by the sum of wrong-charge D combinations and simulated D^* mesons combined with proton candidates. The wrong-charge D combinations are scaled to the number of D^* candidates with $\Delta M(D^*) > 0.15$ GeV in the $\Delta M(D^*)$-histogram. The D^* Monte Carlo is scaled to the number of D^* mesons in the data obtained from a gaussian fit. Also shown is a background-only fit to the $M(D^*p)$ spectrum in the range $2970 < M(D^*p) < 3600$ MeV. The fit function is described in section 4.4.

The background description of $M(D^*p)$ in the $K\pi\rho\pi_s p$ decay (middle panel of figure 4.9) by the sum of wrong-charge D combinations and D^* simulation is systematically low for a $x_{obs}(D^*p)$-cut. A little enhancement can be seen for no additional cuts in the $M(D^*p)$ spectrum in the $K\pi\pi\pi\pi_s p$ decay (upper panel of figure 4.10). However, for a significant peak, more data will have to be collected and analyzed. Overall, no significant structure is observed at 3099 MeV. Upper limits on θ_c production are determined in section 4.4.

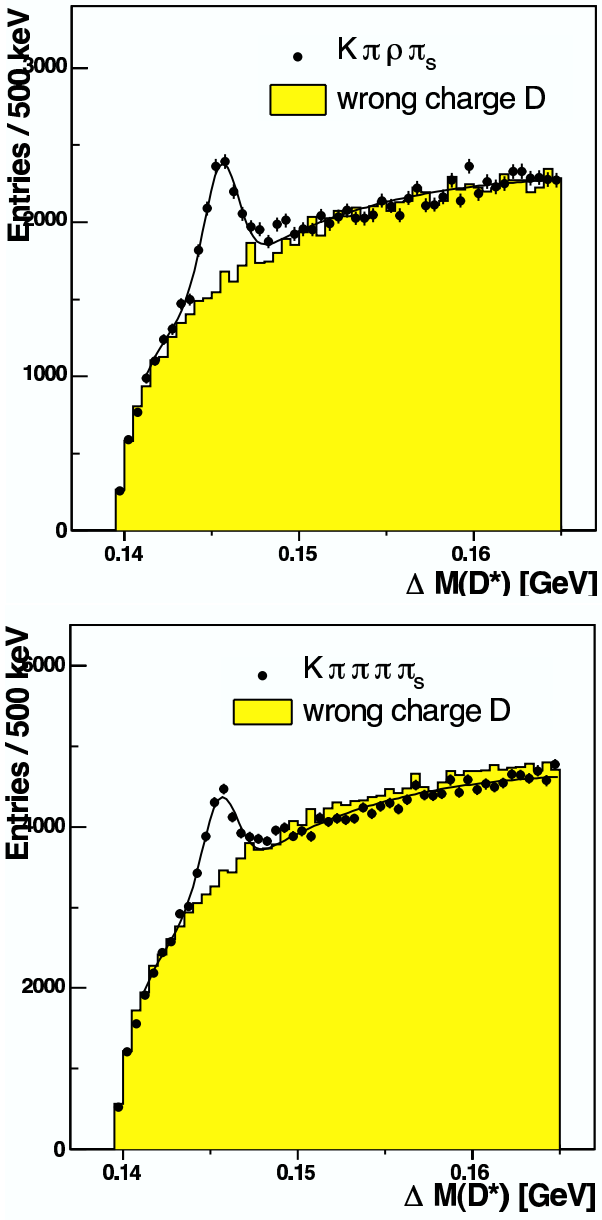

Figure 4.8: Mass difference spectrum for D^* candidates in the decay channels $D^* \rightarrow K\pi\rho\pi_s \rightarrow K\pi\pi\pi\pi_s$ and $D^* \rightarrow K\pi\pi\pi\pi_s$. The applied selection cuts are listed in table 4.2.

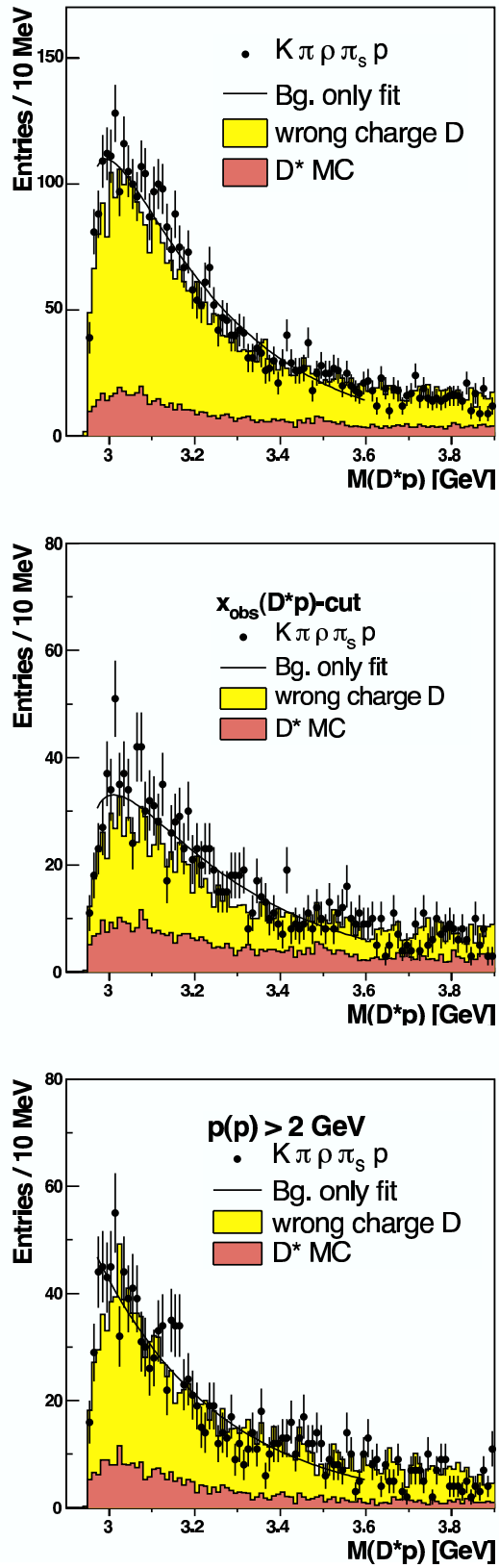

Figure 4.9: Invariant mass spectra for D^*p combinations in the decay channel $D^*p \to K\pi\rho\pi_s p$.

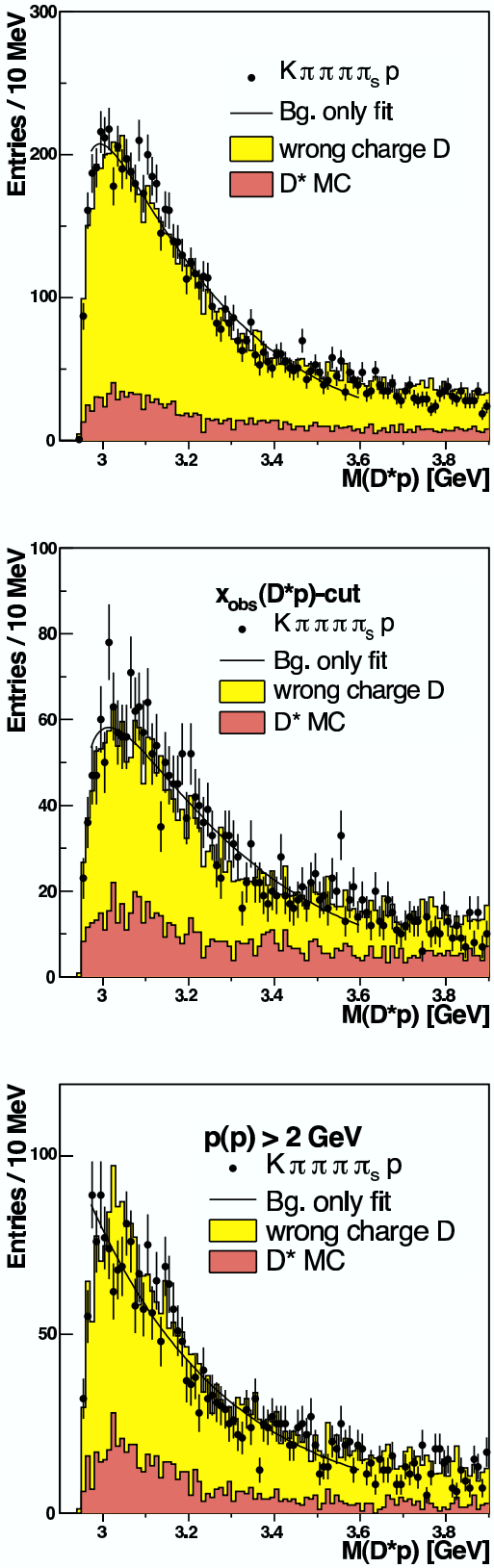

Figure 4.10: Invariant mass spectra for D^*p combinations in the decay channel $D^*p \to K\pi\pi\pi\pi_s p$.

D^* meson content of the signal region

The D^* content in the invariant D^*p mass around 3.1 GeV is tested by forming the $M(D^*p)$ distribution with the full selection on proton and D^*p combination, but with no requirement on $\Delta M(D^*)$. In figure 4.11, the D^* mass difference spectrum from simulated D^*p combinations is shown in signal region (3085 MeV $< M(D^*p) <$ 3115 MeV) and side band region (2990 MeV $< M(D^*p) <$ 3070 MeV or 3130 MeV $< M(D^*p) <$ 3210 MeV), corresponding to the signal position observed in the decay channel $D^*p \to K\pi\pi_s p$. A simulation of D^* mesons (upper panel) is compared to a simulation of D^* mesons from charmed pentaquarks (lower panel). A clean peak around the expected D^* mass is observed in both panels. However, while the D^* mass difference spectra for signal and side band region in the upper panel exhibit the same shapes, there is a significant difference in signal and side band region for the simulated pentaquarks. The D^* content of the signal region is richer.

D^* mass difference spectra from D^*p combinations in the data are shown in figures 4.12 ($D^*p \to K\pi\rho\pi_s p \to K\pi\pi\pi\pi_s p$) and 4.13 ($D^*p \to K\pi\pi\pi\pi_s p$). The number of D^* mesons is extracted with D^* peak position and width kept fixed to the values obtained from figure 3.16 ($\langle\Delta M\rangle = 145.5$ MeV and $\sigma_{\Delta M} = 0.95$ MeV). Values are given in table 4.4.

	$K\pi\rho\pi_s p$	$K\pi\pi\pi\pi_s p$
General selections	39 ± 6	80 ± 9
$x_{obs}(D^*p)$-cut	20 ± 4	40 ± 6
$p(p) > 2$ GeV	2 ± 1	23 ± 5

Table 4.4: Number of D^* candidates in the D^*p signal window for the discussed final states.

The side band region is observed to exhibit systematically less D^* candidates than the signal region for the selection cuts on $x_{obs}(D^*p)$ and $p(p)$. However, more data needs to be analyzed to allow for a definitive answer on whether the signal region is richer in D^* mesons than the side band region is observed.

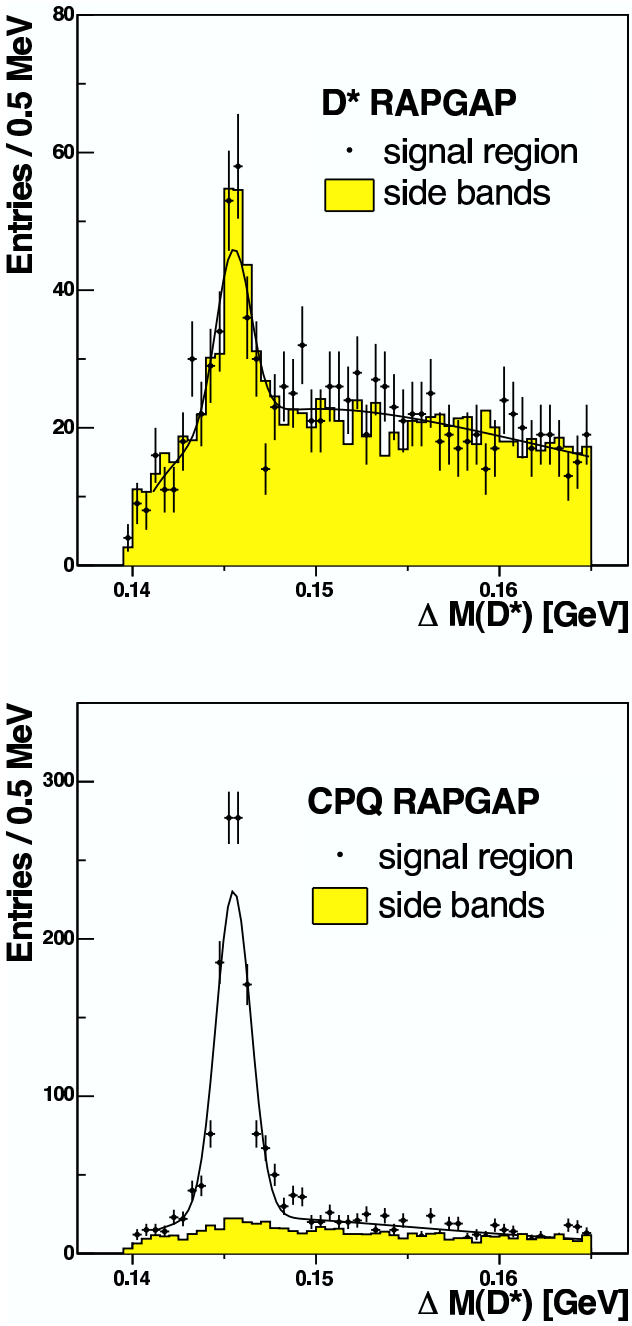

Figure 4.11: Simulated D^* mass difference spectra for D^*p combinations with invariant mass of the 3085 MeV $< M(D^*p) <$ 3115 MeV (signal region) and 2990 MeV $< M(D^*p) <$ 3070 MeV or 3130 MeV $< M(D^*p) <$ 3210 MeV (side bands). No requirement on the D^* mass difference is imposed. The side band distribution is normalized according to the widths of the chosen sample region. The expected spectrum for D^* candidates (upper panel) is compared to the spectrum of D^* mesons from charmed pentaquarks (lower panel).

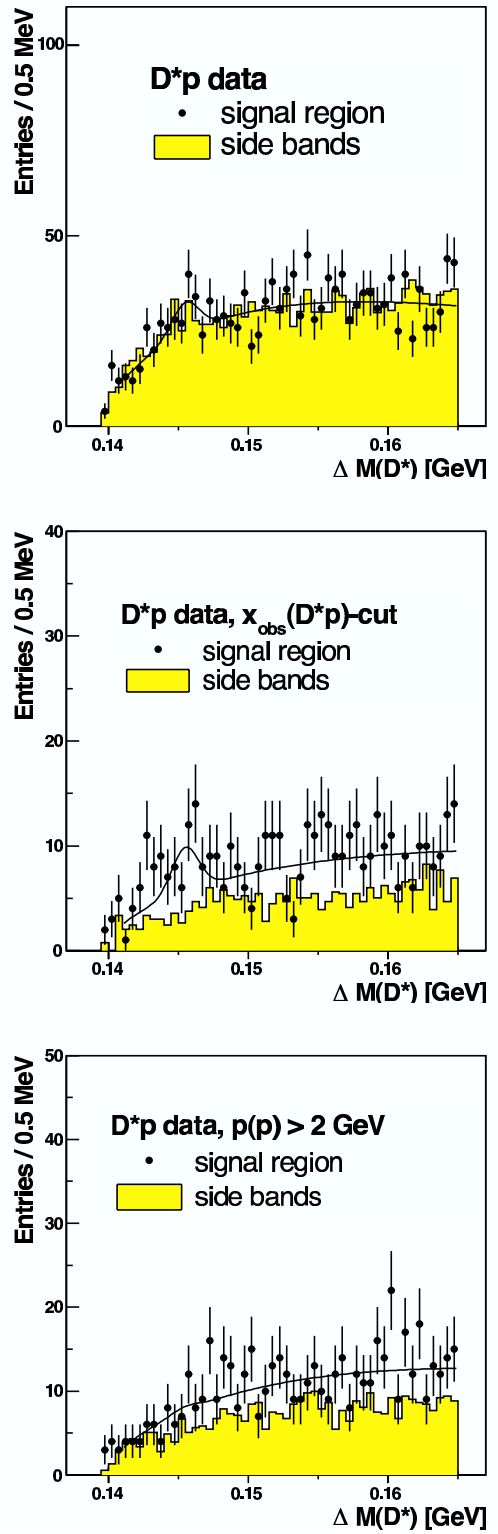

Figure 4.12: D^* mass difference spectra in the channel $D^*p \to K\pi\rho\pi_s p \to K\pi\pi\pi\pi_s p$ for D^*p combinations with invariant mass of the 3085 MeV $< M(D^*p) <$ 3115 MeV (signal region) and 2990 MeV $< M(D^*p) <$ 3070 MeV or 3130 MeV $< M(D^*p) <$ 3210 MeV (side bands). No requirement on the D^* mass difference is imposed. The side band distribution is normalized according to the widths of the chosen sample region.

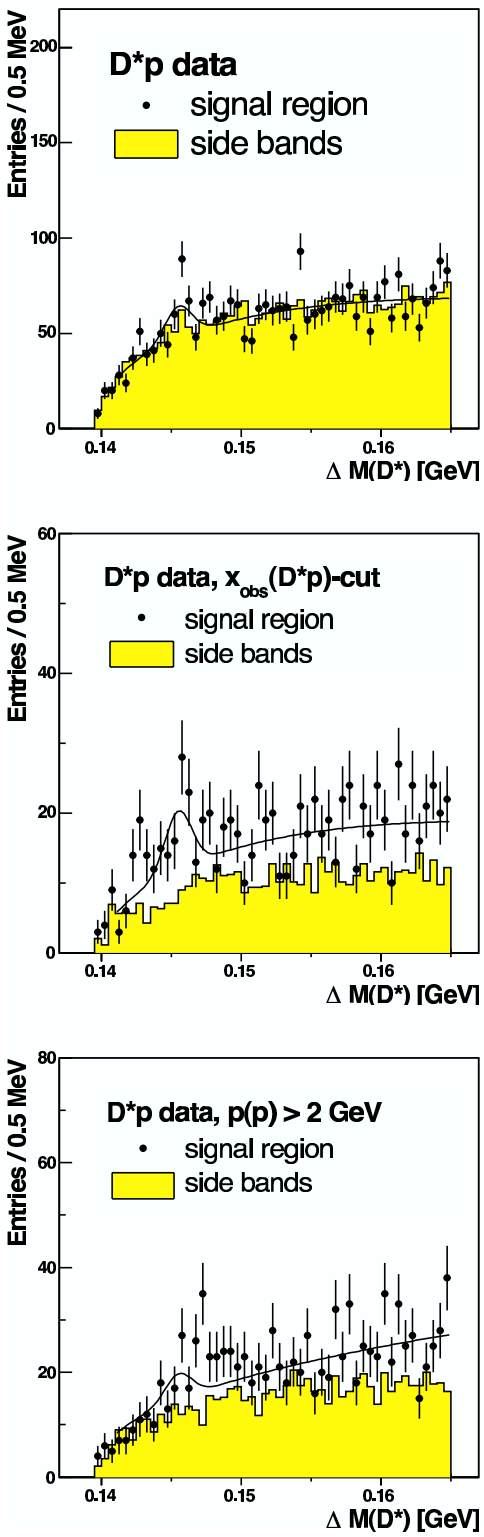

Figure 4.13: D^* mass difference spectra in the channel $D^*p \to K\pi\pi\pi\pi_s p$ for D^*p combinations with invariant mass of the 3085 MeV $< M(D^*p) <$ 3115 MeV (signal region) and 2990 MeV $< M(D^*p) <$ 3070 MeV or 3130 MeV $< M(D^*p) <$ 3210 MeV (side bands). No requirement on the D^* mass difference is imposed. The side band distribution is normalized according to the widths of the chosen sample region.

4.4 Limits on θ_c production

In this section, upper limits on the θ_c production cross section are determined for the data taken in the years 1996-2000, corresponding to an integrated luminosity of 75 pb^{-1}. The visible range is defined by the requirements given in table 4.5. The dependence of the overall acceptance on the θ_c mass has

$-1.5 < \eta(\theta_c) < 1$
$p_T(\theta_c) > 2.5$ GeV
$1\ \text{GeV}^2 < Q^2 < 100\ \text{GeV}^2$
$0.05 < y < 0.7$

Table 4.5: Visible range for the extraction of upper limits on θ_c production.

not been investigated. The acceptances stated in table 4.3 are hence used for the entire $M(D^*p)$ mass range.

A recent analysis [45] using data taken with the H1 detector reported a non-observation of a significant structure in the invariant mass of $K^0_s p$ combinations. The existence of such a state would be evidence for the strange pentaquark state θ^+. The extraction of upper limits on the $\theta_c \rightarrow D^*p \rightarrow K\pi\rho\pi_s p$ production cross section is performed in an analog manner as in [45]. The $M(D^*p)$ distribution is fitted in the range [2970 MeV, 3600 MeV] with a background function f_{bg} of the form

$$f_{bg}(M) = \alpha(M - m_{D^*} - m_p)^\beta \exp(\gamma(M - m_{D^*} - m_p)) \quad , \tag{4.8}$$

where α, β and γ are free parameters and m_{D^*} and m_p are the nominal masses of D^* meson and proton, respectively. The fit results are shown in figures 4.9 and 4.10, respectively.

The number of background events N_{bg} is determined from an integration of the thus obtained background function f_{bg} in a 48 MeV window (corresponding to $\pm 2\sigma$ [28]) around the assumed mass. The possible signal in this window corresponds to the difference of the total number N of events in the integration window and the number of background events N_{bg} in that window. This number of possible θ_c events is extrapolated to the entire range by a division by 0.95.

The upper limit N_{UL} on the θ_c yield at 95% confidence level, is[2]

$$N_{UL} = \frac{1}{0.95}\left(\max(N - N_{bg}, 0) + 1.64 \cdot \sqrt{N}\right) \quad . \tag{4.9}$$

The final step is to convert this upper limit N_{UL} on the D^*p yield to an upper limit on the total production cross section:

$$\sigma_{UL}(\theta_c \to D^*p) = \frac{N_{UL}(\theta_c \to D^*p)}{\mathcal{B}(D^* \to K\pi\pi\pi\pi_s) \cdot \epsilon \cdot \mathcal{L}} \tag{4.10}$$

A scan of the $M(D^*p)$ range in the region [2979 MeV, 3219 MeV] has been performed.

The total production cross section for θ_c production cross section in the decay channel $\theta_c \to D^*p \to (K\pi\pi_s)p$ for the visible range defined in table 4.5 is

$$\sigma(\theta_c \to D^*p \to (K\pi\pi_s)p) = 76.3 \pm 18.4 \text{ (stat.) pb [46].} \tag{4.11}$$

This value has been determined with a similar set of selections as given in table 4.2 and the previously described selection cut on the fragmentation variable $x_{obs}(D^*p)$. The corresponding $M(D^*p)$ spectrum for the decay $D^*p \to K\pi\rho\pi_s p$ (see middle panel of figure 4.9) is shown again with the fit parameters in figure 4.14. Also shown is a shaded band indicating a 48 MeV region around 3099 MeV, where the enhancement was found in the invariant mass of $K\pi\pi_s p$ combinations.

The upper limits on the θ_c production cross section for $\theta_c \to D^*p$, $D^* \to K\pi\rho\pi_s$ and $D^* \to K\pi\pi\pi\pi_s$ are shown in the lower panel of figure 4.15, while in the upper panel upper limits on the θ_c yield are shown. The upper limit from $D^*p \to K\pi\rho\pi_s p$ at $M(D^*p) = 3099$ MeV is consistent with the observed production cross section from $D^*p \to K\pi\pi_s p$ within the statistical error.

[2]The factor 1.64 comes from the asymmetric exclusion of an area under the Gaussian distribution: 95% of the area under a normalized Gaussian distribution f_{Gauss} are contained in an intervall $[-\infty, 1.64\sigma]$ (with the mean assumed to be zero): $\int_{-\infty}^{1.64\sigma} f_{Gauss}(x)dx = 0.95$

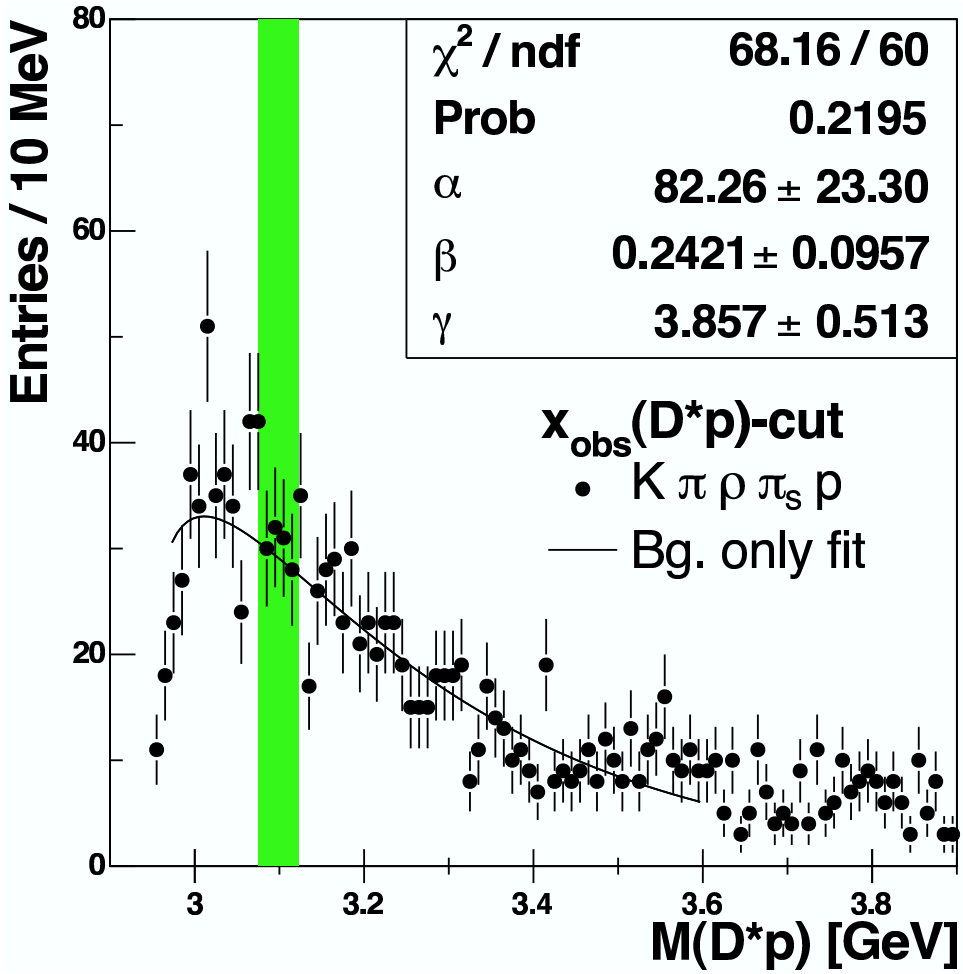

Figure 4.14: $M(D^*p)$ distribution for a selection cut on $x_{obs}(D^*p)$. Also shown is a background-only fit to the mass spectrum in the range $2970 < M(D^*p) < 3600$ MeV. The shaded band indicates a 48 MeV region around 3099 MeV, the position of the observed enhancement in the $K\pi\pi_s p$ final state.

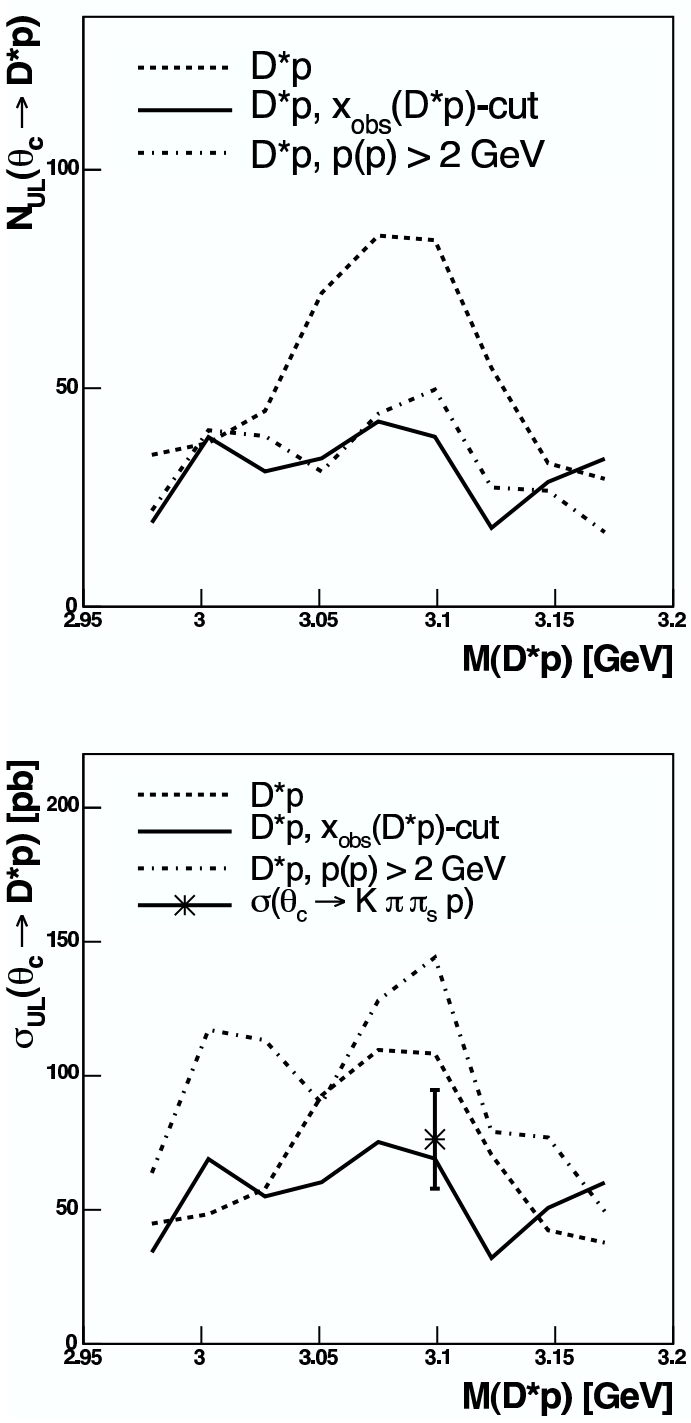

Figure 4.15: Upper limits on θ_c production yield (upper panel) and cross section (lower panel) for $D^*p \to K\pi\rho\pi_s p$. Also indicated is the θ_c production cross section measured in the decay $D^* \to K\pi\pi_s$ [43] obtained from a comparable set of selections and the described cut on the fragmentation variable $x_{obs}(D^*p)$. The corresponding upper limits are represented by the solid line.

4.5 Discussion

A search for an exotic baryon containing charm has been performed for D^*p combinations reconstructed in the decay channels

$$D^{*+}\bar{p} \rightarrow D^0\pi_s^+\bar{p}\ ,\ D^0 \rightarrow K^-\pi^+\rho^0\ ,\ \rho^0 \rightarrow \pi^+\pi^- \tag{4.12}$$

$$D^{*+}\bar{p} \rightarrow D^0\pi_s^+\bar{p}\ ,\ D^0 \rightarrow K^-\pi^+\pi^+\pi^- \tag{4.13}$$

and charge conjugates. D^* candidates have been combined with proton candidates of the opposite charge and the invariant mass of this combination has been investigated. While the observed narrow state [28] in D^*p combinations reconstructed in the decay chain $D^{*+}\bar{p} \rightarrow D^0\pi_s^+\bar{p}$, $D^0 \rightarrow K^-\pi^+$ is reproduced with the discussed selections, no enhancement is found in the invariant mass of D^*p combinations reconstructed in the above listed decay channels.

Since no resonance could be observed for the $K\pi\rho\pi_s$ and the $K\pi\pi\pi\pi_s$ final states, upper limits have been determined. The corresponding θ_c production cross section from the observed state reconstructed in the $K\pi\pi_s$ decay is consistent with the upper limits on the θ_c production cross section from D^*p combinations reconstructed in the decay channel (4.12), as can be seen in figure 4.15. The corresponding $M(D^*p)$ spectrum (figure 4.14) does not exhibit an enhancement at 3099 MeV, but large fluctuations around that value. This is expected to change when a larger data sample is analyzed.

It will be interesting to compare the determined upper limits for different selection cuts to the corresponding production cross sections. Furthermore, other selection cuts can be studied to get a better understanding of the $M(D^*p)$ spectrum: D^*p candidates could be selected by the largest fragmentation variable $x_{obs}(D^*p)$, as an analog selection is observed to greatly improve the signal-to-background ratio for D^* mesons.

The interesting fact that the observed acceptance corrected yields are compatible in both decay channels suggests that an analysis of the calibrated H1 data taken from 2000 on will lead to a better understanding of the observed narrow enhancement in the invariant mass of D^*p combinations.

Chapter 5

Summary

In this work, production and decay of D^* mesons in deep-inelastic electron-proton scattering is studied. The D^* mesons are detected via the decay chain

$$D^{*+} \to D^0 \pi_s^+ \ , \ D^0 \to K^- \pi^+ \rho^0 \ , \ \rho^0 \to \pi^+ \pi^- \qquad . \tag{5.1}$$

This decay channel has previously not been exploited for H1 analyses and can contribute to increase the total number of D^* mesons by a factor of two. However, one has to take into account that due to the high combinatorial background a cut $x_{obs}(D^*) > 0.5$ has to be done which limits the kinematic range. After the calibration of the data collected with the H1 detector from 2000 on, a gain of a factor of two in the total number of D^* mesons is to be expected for the data taken within the H1 experiment from 2000 on.

Systematic errors still need to be determined. In particular, the influence of D^* mesons decaying to a $K\pi\pi\pi\pi_s$ final state which are misidentified as D^* mesons decaying via (5.1) has to be studied. The branching ratio used for the determination of production cross sections needs to be corrected for such a situation. The correlation of imposed selection cuts also needs to be studied closely. In particular, the selection cut $x_{obs}(D^*) > 0.5$ suppresses candidates in the forward region.

In a second part of this work, a search for exotic baryons containing charm with a mass of 3099 MeV has been performed with protons and D^* mesons reconstructed in the decay channel (5.1). Although the narrow enhancement in the invariant mass of D^*p combinations reconstructed in the channel

$$D^{*+} \bar{p} \to D^0 \pi_s^+ \bar{p} \ , \ D^0 \to K^- \pi^+ \tag{5.2}$$

has been reproduced, no resonant structure has been found for D^*p combi-

nations reconstructed in the decay channels

$$D^{*+}\bar{p} \rightarrow D^0\pi_s^+\bar{p}\ ,\ D^0 \rightarrow K^-\pi^+\rho^0\ ,\ \rho^0 \rightarrow \pi^+\pi^- \text{ and} \tag{5.3}$$

$$D^{*+}\bar{p} \rightarrow D^0\pi_s^+\bar{p}\ ,\ D^0 \rightarrow K^-\pi^+\pi^+\pi^- \quad . \tag{5.4}$$

Upper limits on the production cross sections for charmed pentaquarks decaying to D^*p combinations have been determined. The upper limits are consistent with the measured cross section for the observed narrow state in D^*p combinations [28] within the statistical error. Including the data taken from 2000 on will lead to a more precise statement on this issue as suggested by the compatible acceptance corrected yields for the $K\pi\pi_s p$ final state and the $K\pi\pi\pi\pi_s p$ final state.

An object-oriented data storage and analysis environment, based on the ROOT framework and called H1OO, has been introduced within the H1 collaboration. A finder class for the decay channel (5.1) has been developed within this work and will be added to the standard H1OO analysis tools.

Bibliography

[1] R. K. Ellis, W. J. Stirling, and B. R. Webber, Camb. Monogr. Part. Phys. Nucl. Phys. Cosmol. **8**, 1 (1996).

[2] Particle Data Group, S. Eidelman *et al.*, Phys. Lett. **B592**, 1 (2004), http://pdg.lbl.gov/pdg.html.

[3] S. Schmidt, *Measurement of charm induced dijet events in deep-inelastic scattering with the H1 detector at HERA (in German)*, PhD thesis, Technische Universität München, 2004, DESY-THESIS-2004-043.

[4] ZEUS Collaboration, L. Gladilin, (2001), Talk at the International Europhysics Conference on High Energy Physics, EPS, Budapest.

[5] H1 Collaboration, C. Adloff *et al.*, Phys. Lett. **B528**, 199 (2002).

[6] K. Daum, S. Riemersma, B. W. Harris, E. Laenen, and J. Smith, (1996), hep-ph/9609478.

[7] A. Chuvakin, J. Smith, and W. L. van Neerven, Phys. Rev. **D62**, 036004 (2000), hep-ph/0002011.

[8] B. R. Webber, Nucl. Phys. **B238**, 492 (1984).

[9] G. Marchesini and B. R. Webber, Nucl. Phys. **B310**, 461 (1988).

[10] B. Andersson, G. Gustafson, and B. Soderberg, Z. Phys. **C20**, 317 (1983).

[11] M. G. Bowler, Zeit. Phys. **C11**, 169 (1981).

[12] D. A. Morris, Nucl. Phys. **B313**, 634 (1989).

[13] C. Peterson, D. Schlatter, I. Schmitt, and P. M. Zerwas, Phys. Rev. **D27**, 105 (1983).

[14] D. Besson, Eur. Phys. J. **C15**, 218 (2000).

[15] LEPS Collaboration, T. Nakano *et al.*, Phys. Rev. Lett. **91**, 012002 (2003), hep-ex/0301020.

[16] DIANA Collaboration, V. V. Barmin *et al.*, Phys. Atom. Nucl. **66**, 1715 (2003), hep-ex/0304040.

[17] CLAS Collaboration, S. Stepanyan *et al.*, Phys. Rev. Lett. **91**, 252001 (2003), hep-ex/0307018.

[18] SAPHIR Collaboration, J. Barth *et al.*, Phys. Lett. **B572**, 127 (2003), hep-ex/0307083.

[19] A. E. Asratyan, A. G. Dolgolenko, and M. A. Kubantsev, Phys. Atom. Nucl. **67**, 682 (2004), hep-ex/0309042.

[20] CLAS Collaboration, V. Kubarovsky *et al.*, Phys. Rev. Lett. **92**, 032001 (2004), hep-ex/0311046.

[21] HERMES Collaboration, A. Airapetian *et al.*, Phys. Lett. **B585**, 213 (2004), hep-ex/0312044.

[22] SVD Collaboration, A. Aleev *et al.*, (2004), hep-ex/0401024.

[23] COSY-TOF Collaboration, M. Abdel-Bary *et al.*, Phys. Lett. **B595**, 127 (2004), hep-ex/0403011.

[24] D. Diakonov, V. Petrov, and M. V. Polyakov, Z. Phys. **A359**, 305 (1997), hep-ph/9703373.

[25] NA49 Collaboration, C. Alt *et al.*, Phys. Rev. Lett. **92**, 042003 (2004), hep-ex/0310014.

[26] R. L. Jaffe and F. Wilczek, Phys. Rev. Lett. **91**, 232003 (2003), hep-ph/0307341.

[27] M. Karliner and H. J. Lipkin, (2003), hep-ph/0307343.

[28] H1 Collaboration, A. Aktas *et al.*, Phys. Lett. **B588**, 17 (2004), hep-ex/0403017.

[29] H. Jung, Comp. Phys. Commun. **86**, 147 (1995).

[30] K. Charchula, G. A. Schuler, and H. Spiesberger, Comput. Phys. Commun. **81**, 381 (1994).

[31] A. Kwiatkowski, H. Spiesberger, and H. J. Mohring, Comp. Phys. Commun. **69**, 155 (1992).

[32] G. Ingelman, A. Edin, and J. Rathsman, Comput. Phys. Commun. **101**, 108 (1997), hep-ph/9605286.

[33] H1 Collaboration, I. Abt *et al.*, Nucl. Instrum. Meth. **A386**, 310 (1997).

[34] H1 Collaboration, I. Abt *et al.*, Nucl. Instrum. Meth. **A386**, 348 (1997).

[35] A. A. Glazov, *Measurement of the Proton Structure Functions $F_2(x, Q^2)$ and $F_L(x, Q^2)$ with the H1 Detector at HERA*, PhD thesis, Humboldt-Universität zu Berlin, 1998, DESY-THESIS-1998-005.

[36] J. Steinhart, *Measurement of the total $c\bar{c}$ photoproduction cross section by the reconstruction of Λ_c baryons using the improved dE/dx particle identification at the H1 experiment at HERA. (in German)*, PhD thesis, Universität Hamburg, 1999, DESY-THESIS-1999-029.

[37] J. Wagner, *Charm and beauty production at HERA with D^* - muon events*, PhD thesis, Universität Hamburg, 2004, DESY-THESIS-2004-022.

[38] H1 Collaboration, L. Favart *et al.*, Integrated Luminosity Measurement using Bethe-Heitler Overlapping Events, H1 note H1-06/94-366.

[39] H1 Collaboration, S. Aid *et al.*, Luminosity Measurement in the H1 Experiment at HERA, submitted to the 28th International Conference of High Energy Physics, ICHEP'96, Warsaw, Poland, pa17-026.

[40] H1 Collaboration, C. Adloff *et al.*, Nucl. Phys. **B545**, 21 (1999), hep-ex/9812023.

[41] C. Grupen, *Teilchendetektoren* (BI-Wiss.-Verl., 1993).

[42] H1 Collaboration, Z. Rurikova, (2005), Talk at the Thirteenth International Workshop on Deep Inelastic Scattering, DIS2005, Madison, Wisconsin, USA.

[43] K. Lipka, private communication, 2005.

[44] H1 Collaboration, K. Daum, (2005), Talk at the Thirteenth International Workshop on Deep Inelastic Scattering, DIS2005, Madison, Wisconsin, USA.

[45] H1 Collaboration, C. Risler, (2005), Talk at the Thirteenth International Workshop on Deep Inelastic Scattering, DIS2005, Madison, Wisconsin, USA.

[46] K. Daum, private communication, 2005.

Acknowledgments

This thesis profits from many intensive discussions with lots of wonderful people within the H1 experiment, DESY Zeuthen and the Humboldt University. Some of them shall be mentioned in the following.

Katerina Lipka has been an outstanding teacher and supervisor who encouraged me on this exciting topic within the H1 collaboration. Her advice, support and criticism have been invaluable for my work. I sincerely appreciated our discussions on physics, life and everything else.

I wish to thank Hermann Kolanoski for giving me the opportunity to work as a diploma student within the H1 collaboration, for introducing me to Elementary Particle Physics and for getting me involved into his lecture on particle detectors. He taught me to continuously question my results and to always work with an open mind.

Heartfelt thanks to Karin Daum for many comments, suggestions and ideas on my analysis. I much appreciated our discussions on the search for charmed pentaquarks.

I am also grateful to Christiane Risler for our discussions on the extraction of upper limits on the pentaquark production cross section. Zuzana Rurikova had helpful comments and suggestions on charm fragmentation issues. Thank you also to the rest of the MPI Munich group under Günter Grindhammer who turned my time as a Summer Student into a wonderful introduction to charm physics at H1.

Furthermore, I would like to express my gratitude to Martin zur Nedden for proof-reading and discussions on the H1 trigger system.

I am indebted to Peter Kostka, Thomas Naumann and Jan Kretzschmar for continuous support, proof-reading and the overall warm and friendly atmosphere within the H1 group at DESY Zeuthen.

My parents have been a wonderful support throughout the past 26 years. Needless to say, that my entire studies would have hardly been possible without their help. Last but not least, I would like to thank Ute for sharing the ups and downs, laughs and tears that led to this thesis.

Erklärung

Hiermit bestätige ich, ich die vorliegende Arbeit ohne unerlaubte fremde Hilfe angefertigt und nur die angegebene Literatur und Hilfsmittel verwendet zu haben.
Mit der Auslage meiner Diplomarbeit in der Bibliothek der Humboldt-Universität zu Berlin bin ich einverstanden.

Florian Bechtel
Berlin, den 22.08.2005